

Response to Anonymous Referee #1

Included below are our responses to the comments from Anonymous Referee #1 on our ACPD paper. The specific referee comments are given in bold italics and our responses in plain text. We thank the referee for their insightful comments which have resulted in a much improved manuscript.

Major Comments:

-The paper lacks a comparison/validation of the CALIPSO-derived PSC occurrence statistics to long-term PSC statistic from ground-based measurements in the Antarctic and Arctic.

We agree that it is important to link the CALIPSO satellite-derived PSC statistics to the long-term ground-based measurements. To that end, a detailed comparison of observations of PSC occurrence and composition from CALIOP and the ground-based lidar at McMurdo is the focus of a separate paper that has just been submitted for review in ACPD (Snels et al., acp-2018-589). The paper is collaboration between the CALIOP team and colleagues at the Institute of Atmospheric Sciences and Climate (CNR-ISAC) in Italy. In general, point-to-point comparison between ground-based and satellite based lidar measurements is extremely difficult due to the intrinsic differences in the observation geometries and the imperfect overlap of the observed areas. Therefore this study employs a statistical approach to compare the satellite- and ground-based observations from a 5-year period (2006-2010). The ground-based McMurdo lidar data have been processed using a detection and classification algorithm which closely follows the CALIOP v2 algorithm in order to avoid a bias due to different classification schemes. The relative occurrences of the four PSC compositions, STS, NAT mixtures, enhanced NAT mixtures and ice, averaged over the five year overlap period are very similar for ground-based and CALIOP observations, and also the vertical distribution compares well.

We have also compared CALIOP PSC occurrence frequencies for 2006-2017 with published PSC climatologies for McMurdo and Ny-Ålesund ground-based lidars (Di Liberto et al., 2014; Massoli et al., 2006). A summary of these comparisons is now included in Section 6 of the revised manuscript. For these comparisons, we took the subset of CALIOP observations within $\pm 1.5^\circ$ latitude and $\pm 15^\circ$ longitude of McMurdo and Ny-Ålesund. The CALIOP occurrence frequency distribution for the McMurdo coincidences is very similar to the ground-based McMurdo distributions for both the 2006-2010 period (Figure 3 in Di Liberto et al., 2014) and 1995-2001 period (Figure 3 in Massoli et al., 2006), illustrating both the consistency between the satellite and ground-based lidar datasets and the regularity of the Antarctic PSC seasons. The CALIOP distribution for the Ny-Ålesund coincidences is qualitatively similar to the ground-based Ny-Ålesund distribution for the 1995/96-2002/03 period (Figure 3 in Massoli et al., 2006), but the lack of agreement in absolute sighting frequencies is not surprising given the large interannual variability in Arctic PSCs and the lack of temporal overlap between the satellite and ground-based datasets.

-The authors compare their v1 and v2 composition schemes only for theoretical calculations. The paper would benefit from an example case for both the v1 and v2 classification, i.e. plots such as Figures 3 and 4 with real data, for instance the PSC observation presented in Figure 2.

We are very appreciative of this suggestion by the referee and have added 2-D histogram figures (new Figures 5 and 6) showing the distribution of CALIOP PSC observations in the v1 and v2 classification optical spaces. The observations are from the period 10-18 July 2008, which includes the orbit shown in Fig. 2 and renumbered Fig. 11. The choice of this time period clearly illustrates that by accounting for denitrification and dehydration, the v2 PSC classification scheme captures the separation between ice and NAT mixture PSCs much better than the v1 scheme.

-Page 11: There is an abundance of balloon-borne in-situ measurements of particle size distributions in PSCs, e.g. Schreiner et al. (2003), Voigt et al. (2003), Deshler et al. (2003). A discussion of these measurements should be provided. Also, why have those data not been considered in the estimation of SAD and VD?

The in situ PSC particle data in Schreiner et al. (2003), Voigt et al. (2003), and Deshler et al. (2003) all appear to have been obtained under mountain wave conditions, so it is not clear that they are representative of PSCs as a whole. However, we did calculate $\beta_{\text{particulate}}$, SAD, and VD based on bimodal lognormal size distribution fits to in situ optical particle counter measurements within three PSC layers presented in Deshler et al. (2003). These calculated points are now included in renumbered Figs. 9 and 10 and show that our estimates of SAD and VD are reasonable. We also have been provided a draft of a manuscript presenting a comprehensive analysis of coincident in situ PSC particle size distributions and ground-based lidar measurements from McMurdo. Empirical relationships between $\beta_{\text{particulate}}$ and SAD and VD derived from those data are quite similar to the theoretical relationships we use and give us more confidence in our estimates of SAD and VD.

- Where does the information on the height of the tropopause used in the retrieval come from? How reliable are the values? It seems excessive to dismiss any data within 4 km of the tropopause height.

Tropopause height information is based on the MERRA-2 “blended” tropopause values that are included in the CALIOP Level 1b lidar data product files. The MERRA-2 “blended” tropopause is the lower (in altitude) of the temperature-based (“thermal”) tropopause and potential vorticity (PV) based (“dynamic”) tropopause (Bosilovich et al., 2016; Ott et al., 2016). In practice, the MERRA-2 “blended” tropopause is usually the “dynamic” tropopause in mid- and high-latitudes, but switches to the “thermal” tropopause in the tropics. The tropopause is often difficult to locate in the polar regions, especially during the polar nights (e.g., Highwood et al., 2000), so any tropopause height determination in these regions should be used with caution. It is our experience that the transition from upper tropospheric cirrus to PSCs is often ambiguous with no clear separation across the reported tropopause. Therefore, using the MERRA-2 tropopause as a hard boundary to separate tropospheric cirrus from PSCs will lead to misclassifications. Hence, we make no explicit attempt to distinguish tropospheric cloud from stratospheric cloud in the 8.5-30 km altitude range over which we produce the CALIOP PSC cloud mask. However, we do tag each

observation in the database with a feature flag that identifies its altitude location relative to the reported “blended” tropopause as one of three possibilities: (1) below the tropopause, (2) between the tropopause and tropopause + 4 km, or (3) above the tropopause + 4 km. This allows data users to perform some crude separation between troposphere and stratosphere as desired. Only in the PSC spatial volume analyses (renumbered Figs. 16 and 23) and composition pie charts (renumbered Figs. 12 and 26) do we exclude data within 4 km of the tropopause because inclusion of the omnipresent cirrus would distort the statistics on the temporal evolution of PSC occurrence and relative fraction of ice PSCs. We have improved the v2 composition classification algorithm in the lower stratosphere/upper troposphere by incorporating observed Aura MLS H₂O and HNO₃ abundances in the determination of the optical space composition boundaries at these lower altitudes. However, cirrus clouds will be identified simply as ‘ice’ clouds in our algorithm. We now include the location of the MERRA-2 tropopause in many of the figures as a guide to the reader for the approximate upper extent of cirrus. We have also added a discussion in the revised manuscript of the difficulty in using the tropopause to separate cirrus from PSCs.

- Figure 15c shows the highest occurrence rate of ice PSCs below 15 km height. I would expect to see those higher up, particularly as Figure 16 shows that the frost point temperature is only reached above 15 km height. Can cirrus still be misclassified as ice PSC?

As discussed above, we do not explicitly separate tropospheric ice clouds from stratospheric ice clouds due to the uncertainty in the location of the tropopause. To put better focus on PSCs, we limit the lower altitude in (renumbered) Fig. 17 to 12 km, near the climatological maximum MERRA-2 tropopause as shown in (renumbered) Fig. 15. The higher occurrence rates of ice clouds below 15 km are indeed likely due cirrus clouds. Using the MERRA-2 “blended” tropopause height as the discriminator does not completely filter out cirrus and enhanced ice occurrence rates are still present below 15 km. However, if we use the tropopause height + 4 km as the discriminator, the high ice frequencies associated with cirrus below 15 km completely disappear. We added some sentences in the description of (renumbered) Fig. 17c to mention that the ice cloud statistics do include some cirrus in the lower altitudes.

- Please add a figure on the occurrence rate of different PSC types with altitude for the Arctic.

Due to the high degree of interannual variability in PSC occurrence in the Arctic, the 11-year mean depictions of PSC occurrence and composition do not accurately represent the seasonal evolution in any given year and, in fact, may provide a misleading picture of PSC occurrence. Therefore we avoided including such representations in our original manuscript. However, based on referee suggestions, we now include these in the revised manuscript with appropriate caveats. In terms of the climatology of Arctic PSC composition, we feel that it is meaningful to show only the composite season-long vertical profile of relative spatial coverage (composition-specific area normalized by total PSC area). This is now included as new Figure 24. STS and NAT mixtures are the major Arctic PSC compositions as expected, with STS (NAT mixtures) predominant above (below) 24 km. Ice becomes the predominant composition at altitudes below 14 km, but this likely reflects an imprecise separation of ice PSCs from upper tropospheric cirrus due to uncertainty in the tropopause height.

Minor comments:

- Please be precise in the naming of your parameter to avoid misunderstandings as in my initial comment.

We have attempted to be more precise in our parameter notation by explicitly using perpendicular and parallel symbols. To avoid confusion, we use the subscript “||” to denote parallel, the subscript “⊥” to denote perpendicular, and the subscript “particulate” to denote particulate in the revised manuscript.

- What is the explanation for the change of the crosstalk value in the 2008 Antarctic and 2008-09 Arctic winters, and then again in 2015?

In response to a suggestion by Anonymous Referee #3, we have moved the discussion of crosstalk (CT) to Appendix A. We have added a figure to the Appendix showing the record of CT as derived from measurements of molecular depolarization ratio and have added text as to the likely cause of the increase in CT in the 2008 Antarctic and 2008-09 Arctic winters. There was no change in CT in 2015. There have been no regular measurements of molecular depolarization since March 2015, so we assumed a constant value of CT since that point, as stated in the Appendix.

- Please provide the equation used to calculate the particle linear depolarisation ratio.

Done. This is Equation 2 in the revised manuscript.

What is a typical total backscatter ratio for the stratospheric background aerosol layer from CALIPSO? Is it comparable to ground-based measurements?

During the lifetime of CALIPSO, the total backscatter ratio for the stratospheric aerosol layer in the polar regions has ranged from around 1.04 to 1.1, depending on the aerosol loading in a particular year. Vernier et al. (2009) found excellent agreement between CALIOP stratospheric aerosol scattering ratios and those from ground-based lidar, however these comparisons were primarily confined to lower latitudes. We have compared the CALIOP total backscatter ratio values used in the PSC algorithm to represent background stratospheric aerosol levels with profiles of total backscatter ratio from ground-based lidars at Dumont d’Urville and McMurdo in the Antarctic and Eureka in the Arctic. These comparisons indicate CALIOP and the ground-based lidars generally agree to within 5-10%.

- Page 8, line 7: Spheroids with aspect ratios smaller than 1 should be oblates. Why not use a mixture of prolates and oblates as done by Reichardt et al. (2002, 2014)?

We followed the terminology used by Engel et al. (2013) and Mishchenko and Travis (1998), where the aspect ratio was defined as the ratio of the horizontal to rotational axes lengths, i.e. prolate spheroids have aspect ratios < 1 . We did show calculations for oblate spheroids with an aspect ratio of 1.2 in Pitts et al. (2009), which are similar to the results shown in the

present paper, but with smaller theoretical maximum values of $\delta_{\text{particulate}}$. $\delta_{\text{particulate}}$ is not used for composition classification in our v2 algorithm, so we feel there is no need to repeat the theoretical calculations with a mixture of prolates and oblates.

- Page 8, line 8: What is the maximum value of the particle linear depolarisation ratio and how often have they been observed? I would like to know that these values are not outliers.

Engel et al. (2013) were referring to best agreement with maximum $\delta_{\text{particulate}}$ values of 0.3-0.4 for NAT mixtures and 0.4-0.6 for ice. The 2-D histogram in Figure 5 shows that there are many CALIOP observations in these regions of the optical space, i.e. that they are not outliers.

.- Page 10, line 21: Note that there is literature of lidar ratios in PSCs from ground-based observations, e.g. Reichardt et al. (2004).

Our theoretical lidar ratios are consistent with layer-averaged values for $S_{\text{particulate}}$ at 355 nm shown in Reichardt et al. (2004), e.g. values from 67-82 sr for PSCs with small scattering ratios and values of 20-35 sr for PSCs with large scattering ratios. We have added text accordingly to the revised manuscript.

- Page 13, line 24: Are you referring to millions of PSC profiles or indeed millions of PSC observations (i.e. individual clouds)? Please note that your profiles in the same don't provide independent measurements and that a single cloud might be present over several orbits. This means that your statistics are biased towards oversampled clouds. Please comment.

Here an 'observation' refers to a single CALIOP 5-km horizontal x 180-m vertical resolution measurement sample along a CALIOP orbit track. The spatial extent of PSCs as seen in the CALIOP orbit curtains can be hundreds to even thousands of kilometers horizontally by many kilometers thick. So an individual observation obviously doesn't represent a single independent cloud measurement. However, the distance over which PSCs have reasonably homogeneous physical properties as indicated by the variability in optical parameters is much smaller than the distance between opposite clear air boundaries. For instance, Kent et al. (1997) found a mean horizontal and vertical scale of homogeneity within cirrus clouds to be 20-25 km and 0.6-0.8 km, respectively. Although the scales of homogeneity may be different for PSCs, we are confident that they are much smaller than the distance between clear air boundaries. Although CALIOP may sample the same 'cloud' in adjacent profiles or orbits, each observation represents a different measurement sample volume with potentially different particle ensembles. So yes there likely is correlation between adjoining observations and if we were attempting to count clouds, overlap would be problematic. However, in the context of the discussion on page 13, we list the total number of 'observations' to highlight the vast quantity of data acquired over nearly the whole polar region over 11+ years that goes into these analyses. In deference to the referee, we have reworded the sentence to read: "These composite histograms, which incorporate over 11 years of CALIOP PSC measurements, demonstrate behavior consistent with theoretical expectations for each composition class, providing confidence that the v2 composition classification scheme is robust.

- Page 19, line 7: Again, are you referring to profiles or individual clouds? Please carefully revise your use of numbers of observations/profiles.

See discussion above. We have replaced “observations” with “measurement samples” to avoid implications that individual clouds are being observed with each measurement.

- Page 20: Why has the comparison to SAM II not been performed for Arctic PSCs?

The SAM II/CALIOP analyses are an attempt to assess the possibility of a long-term trend in PSC occurrence. The extremely high variability of Arctic PSC occurrence makes it very difficult to detect any long-term trend in the Arctic and thus we omitted this analysis from the original manuscript. We now include the Arctic results in Section 6 in the revised manuscript. Overall, the CALIOP occultation and SAM II records of Arctic column PSC occurrence frequency are very different, especially in December and January. However, we feel that this is not a long-term trend, but simply a result of comparing measurements from different time periods in a region with very high interannual variability.

- Figure 2: There is no gap between tropospheric and stratospheric clouds. Are they separated, e.g. through the feature classification or the height of the tropopause? If it's the height of the tropopause, please add the respective data to the figure. If it's through the feature mask, please add a subplot with the feature mask.

Figure 2 shows a standard browse image of the CALIOP Level 1b total attenuated backscatter along an orbit similar to what is provided on the CALIPSO web site (https://www-calipso.larc.nasa.gov/products/lidar/browse_images/production/). Only Level 1 processing has been performed at this point (geolocation and conversion to sensor units, e.g. total attenuated backscatter coefficient). Feature detection and classification is part of the Level 2 processing and the corresponding feature mask for this orbit is shown in (renumbered) Figure 11. Figure 2 is shown to simply illustrate the high resolution sampling capability of CALIOP in the polar troposphere and stratosphere. For context, we have added the MERRA-2 “blended” tropopause altitude to Figure 2.

Figure 9: please provide information on the height of the tropopause.

We have added the MERRA-2 ‘blended’ tropopause altitude to the figure.

- Figure 13: please remove all data points below the tropopause.

Given the uncertainty in the reported tropopause location (see discussion above), using the MERRA-2 tropopause to filter out tropospheric cloud produces less than pleasing results with significant amounts of cirrus remaining. To completely eliminate cirrus contamination, we must filter all clouds within several kilometers of the tropopause, which filters some PSCs as well. To avoid this conundrum, we feel it is best to not attempt to filter out upper tropospheric cirrus from the climatology, except in cases where cirrus contamination explicitly skews the statistics. In the context of the climatology, the temporal and spatial extent of the underlying cirrus provides additional information on cloud occurrence in the polar upper troposphere/lower

stratosphere that may be useful to potential users of the database. As mentioned previously, we do include a feature flag in the database that tags each PSC measurement sample with its location relative to the MERRA-2 tropopause. For added context, we have included the climatological daily maximum MERRA-2 polar tropopause height to the figure.

- Figure 19: This figure reveals the same effect as shown in Figure 12 and described on page 14, line 27, though not for all years. This should be discussed. Note that it has been reported previously by Fromm et al. (2003) and Achtert et al. (2012).

Thank you for pointing this out. Yes, although not as common as in the Antarctic, upper tropospheric forcing events also produce deep synoptic-scale cloud layers in the Arctic that can extend from the troposphere into the stratosphere, as previously noted by Fromm et al. (2003) and Achtert et al. (2012). There are several years in (renumbered) Figure 21 that indicate this phenomenon. We have added a brief discussion of this to the text.

- Figure 22: I would have expected a larger fraction of wave ice in the Arctic due to the stronger wave activity, e.g. triggered by Greenland and the Scandinavian mountains. With generally lower temperatures in the Arctic, does the threshold for wave ice require adjustment?

Pitts et al. (2011) found that intense mountain-wave induced PSCs can be distinguished as a subset of CALIOP ice PSCs through their distinct optical signature in R_{532} and lidar color ratio (the ratio of 1064-nm to 532-nm aerosol backscatter coefficients). In general, lidar color ratio is an indicator of particle size; cirrus and tropospheric clouds have color ratios around 1, indicating large particles, while smaller aerosol particles have lower color ratios (Liu et al. 2004). We do not use the color ratio in an absolute sense in our PSC algorithm because of calibration issues and the generally low signal-to-noise (SNR) of 1064-nm CALIOP data in the stratosphere (Hunt et al., 2009). However, an abrupt change in color ratio occurs for ice PSCs with very high values of R_{532} (where the 1064-nm data are more reliable), which we feel is a clear signature of mountain wave PSCs. However, it is important to note that the CALIOP wave-ice PSC class is not all-inclusive; some additional CALIOP ice PSC observations are likely associated with mountain waves, but do not meet our strict ($R_{532} > 50$) wave-ice identification criterion, e.g. observations immediately upwind or downwind of the location of peak backscatter. We have added this caveat to the revised manuscript.

At first glance, the fraction of wave ice in the Arctic seemed small to us as well. However, published studies support the CALIOP statistics. For instance, Alexander et al. (2013) quantified the role of orographic waves on PSC occurrence for four Arctic (2006-07 to 2009-10) and four Antarctic (2007-2010) winter season and found that 37% of Antarctic days and 12% of Arctic days were orographic-wave active. Also, Dörnbrack and Leutbecher (2001) compiled a 20-year climatology of meteorological conditions necessary to produce mountain wave PSCs over Scandinavia and concluded that mountain wave PSCs occurred only about 3 days/month on average (~10%) with a maximum in January. In comparison, CALIOP detected wave ice over Scandinavia on about 6 days/month during January 2006-2017, which is not inconsistent with the published

findings. In terms of relative occurrence, CALIOP wave ice comprises about 2.5% of all ice PSC measurement samples from the Arctic, but only about 0.4% of all ice PSC measurement samples from the Antarctic. So in this sense, wave ice is a larger fraction of total ice PSC occurrence in the Arctic than in the Antarctic.

The referee brings up an interesting point regarding the wave ice threshold in the Arctic compared with the Antarctic. The analysis in Pitts et al. (2011) was based on four years of combined data from both the Arctic and Antarctic with no attempt to separate hemispheres. So to adequately address the referee's point, more detailed analyses separated by hemisphere would be required. This is beyond the scope of the current paper, but will be considered in future work.

Bosilovich, M. G., R. Lucchesi, and M. Suarez, 2016: MERRA-2: File Specification. GMAO Office Note No. 9 (Version 1.1), 73 pp, available from http://gmao.gsfc.nasa.gov/pubs/office_notes.

Ott, L. E., Duncan, B. N., Thompson, A. M., Diskin, G., Fasnacht, Z., Langford, A. O., Lin, M., Molod, A. M., Nielsen, J. E., Pusede, S. E., Wargan, K., Weinheimer, A. J., Yoshida, Y., Frequency and impact of summertime stratospheric intrusions over Maryland during DISCOVER-AQ (2011): New evidence from NASA's GEOS-5 simulations, *J. Geophys. Res., Atmos.*, 121, 3687-3706, doi:10.1002/2015JD024052, 2016.

Highwood, E. J., Hoskins, B. J., Berrisford, P., Properties of the arctic tropopause, *Q. J. Roy. Met. Soc.*, 126, 1515-1532, <https://doi.org/10.1002/qj.49712656515>, 2000.

Alexander, S. P., Klekociuk, A. R., McDonald, A. J., Pitts, M. C., Quantifying the role of orographic gravity waves on polar stratospheric cloud occurrence in the Antarctic and Arctic, *J. Geophys. Res. Atmos.*, 118, 11493-11507, doi:10.1002/2013JD020122, 2013.

Dörnbrack, A., Leutbecher, M., Relevance of mountain waves for the formation of polar stratospheric clouds over Scandinavia: A 20 year climatology, *J. Geophys. Res.*, 106, D2, 1583-1593, 2001.

Response to Anonymous Referee #2

Included below are our responses to the comments from Anonymous Referee #2 on our ACPD paper. The specific referee comments are given in bold italics and our responses in plain text. We thank the referee for their insightful comments which have resulted in a much improved manuscript.

Specific Comments:

P2, L20 ‘sedimentation of large NAT particles (Molleker et al., 2014)’:

Please cite also the original paper(s) referring to the large NAT particles as reason for the denitrification.

This was an oversight. We have added citations to both the Fahey et al. (2001) and Northway et al. (2002) papers.

P5, L16 ‘interpolated to the CALIOP PSC orbit grid using a weighted average of the two nearest MLS profiles’: How has this weighting been performed?

The MLS gas species data are interpolated to the CALIOP orbit grid using an average of the two nearest profiles weighted by the inverse of their relative distance from the CALIOP grid point. We have added this additional information to the text.

P5, L28 ‘The data are then corrected for molecular and ozone attenuation using the MERRA-2 molecular and ozone number density profiles’: Are the ozone profiles from MERRA-2 or those from the MLS retrievals? If MERRA, how strong does it affect the preprocessing if the ‘real’ (MLS) profiles would be used?

The ozone attenuation correction uses MERRA-2 ozone number density profiles. Since 2004, MERRA-2 assimilates Aura MLS profile and OMI total column ozone which has resulted in a marked improvement in the MERRA-2 ozone product. During the period 2004-2014, the differences between MERRA-2 and ozonesonde values are around 5% (Gelaro et al., 2017; Wargan et al., 2017). Comparisons of Aura MLS profile ozone products with ground-based lidar and ozonesonde measurements from sites across the globe also indicate agreement within 5% or better (Hubert et al., 2016). So it appears that the MERRA-2 ozone product is of similar quality as Aura MLS. Therefore, changing the source of ozone from MERRA-2 to MLS would have negligible impact on the ozone attenuation correction. Also note that typical column ozone optical depths in the stratosphere are only on the order of 0.02, so the reduction in two-transmittance due ozone attenuation is about 4%. Therefore, even if one assumes an error in ozone abundance as large as 10% (which is double the uncertainty of MERRA-2), the error in the ozone attenuation correction would only be about 0.5%.

P6, L11: Is the second equation really correct, or should it read: $\beta'_{\perp} = \beta'_{\perp, meas} - \beta'_{\parallel} \times CT$?

This was a typographical error and the equation should read as the referee suggested. This has been corrected in Appendix A in the revised manuscript.

P6, L17 '[unc_par] . . . [unc_perp]':

1. 'par' should everywhere be exchanged by 'para' not to confuse it with 'particles'

To avoid confusion, we use the subscript “||” to denote parallel, the subscript “⊥” to denote perpendicular, and the subscript “particulate” to denote particulate in the revised manuscript.

2. 'unc' is a strange variable. Could it not be called delta_beta', so that the direct connection with beta' becomes clear?

In the revised manuscript, we adopted the ISO naming convention for measurement uncertainty in quantity x, i.e. u(x).

P7, L26 'is fixed at 10 cm⁻³': Could you provide a reason for this value (e.g. a citation) and how large its variation could be?

Based on in situ data on total particle concentrations in the polar stratospheres (Wilson et al., 1990; Campbell and Deshler, 2014; Weigel et al., 2014), we feel that 10 cm⁻³ is a good choice for “nominal” conditions and that 5 cm⁻³ and 15 cm⁻³ represent reasonable bounds on the variability. We have cited these papers in the revised manuscript.

P9, L21 'Points with CI_NS > 1 are presumed to be PSCs containing non-spherical particles.': This seems to be a 2-sigma limit – could you describe more clearly what it means in percentage of the whole data points: how many of the 'non-spherical' particles might be spherical and vice-versa?

CI_{NS} > 1 is roughly equivalent to β_{\perp} values more than 2 median deviations larger than the median β_{\perp} for the background aerosol. Histograms of β_{\perp} for v2 STS and NAT mixtures overlap somewhat and suggest that 10-15% of data points in either class could be misclassified. We have added text accordingly to the revised manuscript.

P9, L28 'detected through gas-phase uptake of HNO₃ as observed by MLS': Regarding your analysis of volume-density later in the manuscript: can you confirm, that the amount of HNO₃ uptake seen by MLS is in accordance with the detection limit of CALIOP?

Simulations in Lambert et al. (2016) indicate that the amount of HNO₃ uptake observed by MLS in sub-visible PSCs is consistent with the detection limits of CALIOP. Figure 12 of that paper shows that very low number density (5×10^{-5} cm⁻³) NAT particles remain undetectable by CALIOP throughout their growth history even though there may be uptake of several ppbv HNO₃ into the particles. Therefore, CALIOP may not detect NAT during the same time that MLS observes a substantial depletion of gas-phase HNO₃. On the other hand, higher number density (5×10^{-4} cm⁻³) NAT particles become detectable by CALIOP and via MLS HNO₃ gas phase depletion on similar time scales. We note in the manuscript that all derived quantities

(including VD) for non-features (including sub-visible PSCs) are retained in the v2 data product. So it is possible to compare our estimates of VD with the HNO_3 uptake observed by MLS in the sub-visible PSCs analyzed by Lambert et al., (2012; 2016), but we have not done this comparison.

P12, L18 ‘8.3%’: In Fig. 10 the number seems 5.8% (?)

This is a typographical error- 5.8% is the right number. We have corrected this in the revised manuscript.

P12, L17...: Apart from the referenced modelling work by Zhu et al., 2018, which additional arguments are there to support the strong increase in the detected ice-PSCs in v2 compared to v1?

As discussed by Pitts et al. (2013), a clear deficiency of v1 was the misclassification of ice as NAT mixtures under denitrified/dehydrated conditions because the NAT/ice boundary was based on a fixed abundance of 10 ppbv HNO_3 and 5 ppmv H_2O . Therefore, the strong increase in ice detections in v2 is expected since it uses a much more appropriate NAT/ice boundary based on MLS observed abundances of HNO_3 and H_2O . Additional supporting evidence for the v2 approach is provided by Spang et al. (2018), who show excellent agreement between CALIOP v2 and MIPAS areal coverage of ice PSCs over the 2009 Antarctic season.

P13, L17...: Is the explanation for the bimodal distribution of NAT-mixtures also confirmed by any modelling work which could be referenced here?

We are not aware of any specific modeling studies that have examined the bimodal distribution of NAT mixtures. However, in Pitts et al. (2013) we explored the source of this bimodality by examining the temperature histories along ten-day backward isentropic trajectories initiated at CALIOP NAT mixture observation points during 2009-10 Arctic winter. The trajectories were produced using the Chemical Lagrangian Model of the Stratosphere (CLaMS) (McKenna et al., 2002) with wind and temperature fields from the European Center for Medium-range Weather Forecasts (ECMWF) analyses. From these temperature histories, we were able to estimate the time the air parcel arriving at each CALIOP NAT mixture observation point was exposed to temperatures below T_{NAT} . The results clearly indicated that NAT mixture observations that occur at temperatures near NAT equilibrium had been exposed to temperatures below T_{NAT} for much longer time periods than the non-equilibrium NAT mixtures that were observed at colder temperatures closer to T_{STS} .

P14, L22 ‘persisting until early October’: From your Fig. 12, PSC are also often seen until mid and even end of October.

The referee is correct that PSCs often are observed by CALIOP until mid and even end of October. We have modified the text to reflect this.

P14, L30...: Is there any possibility to distinguish the PSCs from upper tropospheric cirrus (e.g. in terms of volume/surface density)? Do they ‘separate’ when plotting against potential temperature, if it is mainly caused by an upward displacement of isentropic surfaces, a separation might be possible.

This is an interesting topic that we want to explore further. In particular, we would like to examine particle characteristics in the polar upper troposphere/lower stratosphere when deep cloud decks are present. Given the likely sharp gradients in condensables in this region, we suspect the particle characteristics could vary significantly. In very limited analyses, we have not seen a separation of tropospheric cirrus and PSCs when plotted against potential temperature. Although beyond the scope of the present paper, we plan on pursuing this in future research.

P20, L10 ‘Then, we integrated the occurrence frequencies’: Does ‘integrated’ just mean ‘summed up’?

Yes the occurrence frequencies are compiled at 1-km vertical increments and just summed over altitudes between 14 and 30 km. So a more representative descriptor would be ‘total column occurrence frequency’- we have changed this in the manuscript.

P20, L16: ‘However, note that the SAM II occurrence frequencies are higher than those of CALIOP early in the PSC season.’ May this difference in the early PSC period also be caused by how the sightings in case of SAM II are counted? During this time, there is a clear maximum at around 18 km and a minimum below. As SAM II is a limb-sounder, the sightings below might be influenced by the higher PSCs through which the SAM II line-of-sight passes. Has this been taken into account in the comparison?

This is a good point. Although the occultation weighting functions are highly peaked near the tangent altitude, it is likely that at least to some extent an overlying cloud layer will impact the retrieved extinction values at lower tangent altitudes, with the cloud layer smeared out below the true level of occurrence. We don’t think that this is a large effect, but it could increase the cloud occurrence frequency below the true level of maximum occurrence. We don’t know of any quantitative approach to account for this in our statistics. Note that based on more comprehensive analyses presented in the revised Section 6, SAM II does appear more sensitive to tenuous clouds such as would be observed early in the season.

P20, L17: ‘This may be a reflection of the greater sensitivity of the limb-viewing occultation measurements to the onset of PSCs when liquid droplets first began to deliquesce and/or when low number density NAT particles form that are below the CALIOP detection thresholds’. How far south are the soundings by SAM II in mid-May? Aren’t the ‘sub-visible’ PSCs identified by MLS more in the centre of the vortex where SAM II has not been observing?

PSCs observed by SAM II early in the season were at lower latitudes than the sub-visible PSCs seen by MLS early in the season near the center of the vortex, so they are not the same PSCs. However, the principle is the same, i.e., both SAM II and MLS had/have greater sensitivity to tenuous PSCs than CALIOP. When the sensitivity of SAM II is adjusted to mimic that of CALIOP as we describe in Section 6 in the revised manuscript, there is no statistically significant difference between the two instruments in early season PSC sighting frequencies, so we have deleted the text referring to this difference in the revised manuscript.

P22, L24: ‘The estimates assume liquid particles (binary H₂SO₄-H₂O or STS) only and thus have large uncertainties when NAT mixtures or ice are present’ It would be helpful for the reader to repeat at this point that in case of NAT or ice the values are very probably lower limits of surface and volume density.

We have added a sentence in both Sections 5 and 7 reiterating that our estimated SAD is likely an upper (lower) limit for the actual SAD in NAT mixture (ice) PSCs, and that our estimated VD is likely a lower limit for the actual VD in ice PSCs and in most NAT mixtures.

P33, Fig. 3: To better understand the differences between the new and the old composition classification, either the separation lines of v2 should be included in Fig. 3 or those of v1 in Fig. 4.

Fig. 3 (v1 optical space) now includes a new curve indicating the separation between enhanced NAT mixtures and NAT mixtures in v2. The new curve is noted in the figure caption and is also mentioned in the revised manuscript.

P33, Fig. 3, caption: ‘and symbol sizes are proportional to NAT’ Does ‘size’ mean the symbol area or the diameter?

Since particle size is not an important topic for either Fig. 3 or Fig. 4 (as noted by Anonymous Referee #3), we have made all symbols in these figures the same size to eliminate any confusion.

P44, Fig. 14: The colours are partly difficult to distinguish, could different symbols be used, at least for the case of similar colours?

Figs. 16 and 23 in the revised manuscript now use different symbols and colors so that individual years can be distinguished more easily.

P54, Fig. 24: Please plot the results from both instruments in one graph. As it is now, the comparison in relation to the text is difficult.

Results from CALIOP and SAM II are now plotted in the same graphs, one for the Antarctic (Fig. 32) and one for the Arctic (Fig. 33).

Technical:

P2, L5: ‘of season’ -> ‘of the season’

Changed.

P6, L9,11: numbering of equations missing

Changed.

P14, L20: ‘Hence, it not’ -> ‘Hence, it is not’

Changed.

P16, L17: ‘from the near’ -> ‘from near’

Changed.

P17, L24: ‘about the pole’ -> ‘around the pole’

Changed.

P20, L6: delete blank between ‘degree’ and ‘N’ or ‘S’

Done.

P21, L26: ‘that more are more’ -> ‘that are more’

Changed.

P32, Fig. 2 caption: ‘in yellow’: in Fig. 1 this appears more light green than yellow

We remade the figure and highlighted the orbit of interest in green.

P41, Fig. 11 caption: ‘1 Antarctic’ -> ‘12 Antarctic’ (?)

Changed.

P43 and P49: color bar legend: ‘(x 10⁶ km²)’ should read either ‘(10⁶ km²)’ or ‘/(10⁶ km²)’

Changed to ‘(10⁶ km²)’

References

- Gelaro, R., McCarty, W., Suárez, M. J., Todling, R., Molod, A., Takacs, L., Zhao, B., The Modern-Era Retrospective Analysis for Research and Applications, version 2 (MERRA-2), J. Clim., 30, 5419–5454, <https://doi.org/10.1175/JCLI-D-16-0758.1>, 2017.
- Wargan, K., Labow, G., Frith, S., Pawson, S., Livesey, N., and Partyka, G., Evaluation of the ozone fields in NASA's MERRA-2 reanalysis, J. Climate, 30(8), 2961–2988. <https://doi.org/10.1175/JCLI-D-16-0699.1>, 2017.
- Hubert, D., Lambert, J.-C., Verhoelst, T., Granville, J., Keppens, A., Baray, J.-L., Bourassa, A. E., Cortesi, U., Degenstein, D. A., Froidevaux, L., Godin-Beekmann, S., Hoppel, K. W., Johnson, B. J., Kyrölä, E., Leblanc, T., Lichtenberg, G., Marchand, M., McElroy, C. T., Murtagh, D., Nakane, H., Portafaix, T., Querel, R., Russell III, J. M., Salvador, J., Smit, H. G. J., Stebel, K., Steinbrecht, W., Strawbridge, K. B., Stübi, R., Swart, D. P. J., Taha, G., Tarasick, D. W., Thompson,

- A. M., Urban, J., van Gijssel, J. A. E., Van Malderen, R., von der Gathen, P., Walker, K. A., Wolfram, E., and Zawodny, J. M.: Ground-based assessment of the bias and long-term stability of 14 limb and occultation ozone profile data records, *Atmos. Meas. Tech.*, 9, 2497–2534, <https://doi.org/10.5194/amt-9-2497-2016>, 2016.
- McKenna, D. S., Konopka, P., Grooß, J.-U., Günther, G., Müller, R., Spang, R., Offermann, D., and Orsolini, Y.: A new chemical Lagrangian model of the stratosphere (CLaMS) 1. Formulation of advection and mixing, *J. Geophys. Res. Atmos.*, 107, ACH4.1–ACH4.14, doi:10.1029/2000JD000113, 2002b. 763

Response to Anonymous Referee #3

Included below are our responses to the comments from Anonymous Referee #3 on our ACPD paper. The specific referee comments are given in bold italics and our responses in plain text. We thank the referee for their insightful comments which have resulted in a much improved manuscript.

Minor comments:

To my mind the manuscript is missing a short section/paragraph on comparisons with PSC measurements of other sensors. Some references on comparisons are given at various places of the paper, but I recommend to summarise the comparisons results at one specific place of the manuscript. This would better highlight the quality and reliability of the PSC detection and classification methods of the CALIOP instrument.

Section 6 now includes a summary of comparisons of CALIOP with MIPAS PSC results and ground-based lidar PSC observations at McMurdo and Ny-Ålesund, as well as a more comprehensive quantitative comparison with the historical SAM II PSC record.

I would recommend to move 3.1.1. and 3.1.2 into an appendix. A reduction on technical details in section 3 would be desirable for none-expert readers.

We agree with the referee's recommendation, we have moved the material in these sections to Appendix A. We also added a figure to the appendix in response to questions from Anonymous Referee #1 about changes in crosstalk.

Page 9, line 5: I am wondering that the MIPAS observations show a NAT belt on 2008- 05-29 and 2008/06-01/02 but no indication on May 30. Usually the NAT belt is devolving slowly over a couple of days starting with a small area of NAT/ice activity followed by a downstream formation of a belt-like structure in the next days (e.g. Höpfner et al., 2006). Please clarify, if May 30 is really NAT-free (maybe a typo?) in the MIPAS observations. Is it possible that MIPAS just misses the small NAT area from the day before due to a sampling issue? This potential mismatch may bias your definition of the empirical sub-class of 'enhanced NAT mixtures'.

MIPAS data from 2008-05-30 showed the presence of NAT in just one observation at one altitude, so we originally grouped those data with data from 2008-05-27/28 (which showed zero NAT observations) to characterize observations without the NAT belt. We repeated our analysis excluding CALIOP data from 2008-05-30 altogether and obtained results nearly identical to our original analysis. So, we conclude that our results as presented in the paper are robust. We did discover that our description of CALIOP NAT mixture statistics for 2008-05-27/28/30 was not correct in the original manuscript. It now reads

as follows: “... only about 2% of CALIOP NAT mixture data from those days had $R_{532} > 2$ and $\beta_1 > 2 \times 10^{-5} \text{ km}^{-1} \text{sr}^{-1}$ ” instead of the original version “...about 98% of CALIOP NAT mixture data from those days had $R_{532} \leq 2$ and $\beta_1 \leq 2 \times 10^{-5} \text{ km}^{-1} \text{sr}^{-1}$.”

Section 3.6: The percentages of Figure 10 suggests that mainly enhanced NAT mixtures of Version 1 are classified in Version 2 as ice. Is this correct, or is the effect caused by misclassification of the former Mix-2 and Mix-2enhanced classes. Can you quantify the partitioning between the two V1 classes into the V2 ice class?

Further analysis indicates that about 75% of the additional ice PSCs in Version 2 come from a reclassification of Version 1 Mix2-enhanced PSCs, and the remaining 25% come from a reclassification of Version 1 Mix1 and Mix2 PSCs. The text has been modified accordingly.

Section 3.7: The temperature difference between STS and ice in the $T - T_{ice}$ histogram for the maximum position ($\Delta T 1 - 1.5\text{K}$) looks unexpectedly small to me. I would expect from the equilibrium curves, for example presented in Fig. 5 of Pitts et al. (2013), higher temperatures for STS. Can you please clarify and/or explain in more detail how you defined TST S based on Carslaw et al. (1995).

The roughly 1.5 K difference between the peaks of the STS and ice histograms in $T - T_{ice}$ space is a reflection of the denitrification that occurs during both Antarctic and Arctic winters. For example, Fig. 5(a) of Pitts et al. (2013) shows that the STS equilibrium curve lies about 3.5 K above T_{ice} at 15 ppbv HNO_3 , but actually approaches T_{ice} at very low HNO_3 mixing ratios. T_{STS} is defined using Carslaw et al. (1995) with equilibrium HNO_3 and H_2O mixing ratios equal to those observed by MLS.

Page 13, line 8: Is the 'strong' statement regarding the positive tail in the PSC distribution (that this is due to warm biased temperatures associated with wave ice events not fully resolved in MERRA-2 fields) based on a detailed analysis or 'only' one plausible explanation. Uncertainties of the threshold lines between Ice and NAT may cause a similar tail in the distribution. Please commend and clarify.

Pitts et al. (2011) found that anomalously warm temperatures in ice PSC distributions from the 2009-10 Arctic winter were associated with wave ice events. Given that the MERRA-2 meteorological analyses are computed on a grid with horizontal resolution of approximately $0.5^\circ \times 0.625^\circ$ (55.55 km x 23.75 km at 70° latitude), it is likely that small scale temperature perturbations will not be fully resolved. Hoffman et al. (2017) found that MERRA-2 reanalyses were only able to reproduce about 30% of the standard deviations of the temperature fluctuations observed on long-duration superpressure balloon flights over Antarctica. So it is possible that at least part of the warm tail is associated with poorly resolved temperature perturbations associated with wave ice events. But as the referee correctly points out, it is also plausible that misclassification of NAT mixtures as ice due to measurement noise could produce a similar tail. Overall there are not a lot of anomalously warm ice observations, so it is not a significant issue. We have reworded the text to offer both possibilities as plausible explanations for the positive tail.

The authors may think about to skip Figure 16, which is partly redundant to Fig. 17. For example, Fig. 17 includes by far more quantitative information than Fig. 16 due to the choice of the vertical and horizontal coordinates.

We agree with the referee that there is some redundancy between original Figs. 16 and 17. However, we have decided to not skip the former for the benefit of readers who are more comfortable with geographic coordinates and because including both figures clearly illustrates that more quantitative information comes directly from the coordinate transformation.

Section 6: To my mind the SAM II - CALIPSO comparison would profit by some more detailed descriptions and analyses. The information on SAM II measurements are very limited. For a profound comparison of the PSC occurrence frequencies it would be necessary to discuss the detection limits of both instruments (I guess based on extinction or density thresholds). The authors should discuss similarities and differences between the two sensors as well.

Section 6 now includes a more detailed description of the SAM II measurements and how the CALIOP PSC record was sub-sampled to mimic the SAM II measurement geometry. There is also a comprehensive discussion of the steps we took to put the two data sets on equal footing to establish their relative sensitivities before comparing their multi-year PSC sighting statistics.

Technical corrections:

page 14, line 20: 'Hence, it is not ...'

Changed.

p21, L7: please explain 'DMPs'

The Version 2 (v2) derived meteorological products (DMPs) (Manney et al., 2007; Manney et al., 2011a) consist of gridded meteorological data and derived products, such as equivalent latitude and vortex edge location, that are calculated from the GEOS5-based MERRA-2 reanalyses and interpolated to the locations and times of the MLS measurements. The Aura MLS Derived Meteorological Products (DMPs) acronym is defined in Section 2, first paragraph. A brief description of the DMP data is provided in Section 2.2.

P23, L26: For completeness the authors may like/need to add a reference to the SAM II dataset as well.

Good point, we've added the appropriate references to the SAM II dataset.

page 31/32; Fig. 1/2 caption: CALIOP curtain of Fig. 2 looks on my printout and screen greenish and not yellow. Please check.

We remade the figure and highlighted the orbit of interest in green.

Figure 3: *'The symbols size are proportional to volume-equivalent radii of NAT and ice'. This fact is hard to see in Figure 3 and may cause the effect, that the Mix1 calculations are hiding all STS results. Is the particle size an important topic for this figure? If not, keeping the figure more simple the interpretation of the figure might be easier for the reader. Is the the particle radius also an issue in Figure 4? If yes, this is not obvious from the caption and the text passages in the corresponding section.*

Particle size is not an important topic for either Fig. 3 or Fig. 4, so we have made all symbols in these figures the same size. STS results are now clearly visible in Fig. 3, but are off scale in Fig. 4 because theoretical $\delta_{\text{particulate}}=0$ for spherical particles.

Figure 4: *The authors may explain the grey box in the figure caption (S/N issue) or reference to the details in the corresponding section.*

We have added an explanation for the grey box in the Figure 4 caption.

Figure 18: *Starting at 5% occ. freq. with the colour bar looks a bit extreme. Especially, if this is leading to the strong statement of section 4.1.2 'with essentially no STS' occurrence in the the deep vortex during September. Please clarify, if this statement is an 'artefact'.*

We remade the original Figure 18 (renumbered Figure 20) using 1% occ. freq. as the minimum contour. The original minimum contour of 5% may have been misleading in terms of STS occurrence, although the large difference between STS and NAT mixtures is a robust feature. We have modified the text describing (renumbered) Figure 20 accordingly to state that STS observations are widespread during June at this level, but more limited afterwards with occurrence frequencies generally less than 10% in the interior of the vortex during July-August and less than 5% during September. NAT mixtures, on the other hand, are relatively widespread over much of the vortex at this level, especially during July and August when occurrence frequencies exceed 35%.

References:

Please abbreviate the First Name of the authors (copernicus style) for the references of Wegner et al., Young et al. and Prata et al. .

Done.

References

Hoffmann, L., Hertzog, A., Rößler, T., Stein, O., Wu, X., Intercomparison of meteorological analyses and trajectories in the Antarctic lower stratosphere with Concordiasi superpressure balloon observations, Atmos. Chem. Phys., 17, 8045–8061, <https://doi.org/10.5194/acp-17-8045-2017>, 2017.

Response to Anonymous Referee #4

Included below are our responses to the comments from Anonymous Referee #4 on our ACPD paper. The specific referee comments are given in bold italics and our responses in plain text. We thank the referee for their insightful comments which have resulted in a much improved manuscript.

Minor comments:

1) In the text in Section 3.6 regarding Figure 9, some comment on the fact that v2 only detects ice in the lowest altitude region in the cloud at 26E is also warranted – i.e. ice in the upper troposphere merges seamlessly into ice in the lower stratosphere, rather than having low-level mixed NAT PSCs in (assumedly) the upper troposphere as in v1.

The v2 composition classification extends downward in altitude to the 215 hPa pressure level (~10 km), the lowest reliable level for Aura MLS HNO₃ data that is required to define the location of the NAT mixture/ice boundary in our classification scheme. All clouds at altitudes below this pressure level are assumed to be ice. For altitudes above the 215 hPa pressure level, the v2 composition classification scheme is producing more ice due to an improved characterization of the condensables in the lower stratosphere. We now explicitly state the above in the text.

2) p13, line 9. It would be worth providing a citation for this comment regarding the tail of ice PSC distributions being due to wave ice events.

Anonymous Referee #3 had a similar comment and we repeat our response here. Pitts et al. (2011) found that anomalously warm temperatures in ice PSC distributions from the 2009-10 Arctic winter were associated with wave ice events. Given that the MERRA-2 meteorological analyses are computed on a grid with horizontal resolution of approximately 0.5° x 0.625° (55.55 km x 23.75 km at 70° latitude), it is likely that some small scale temperature perturbations will not be fully resolved. Hoffman et al. (2017a) found that MERRA-2 reanalyses were only able to reproduce about 30% of the standard deviations of the temperature fluctuations observed on long-duration superpressure balloon flights over Antarctica. So it is possible that at least part of the warm tail is associated with poorly resolved temperature perturbations associated with wave ice. But as the referee correctly points out, it is also plausible that misclassification of NAT mixtures as ice due to measurement noise could produce a similar tail. Overall there are not a lot of anomalously warm ice observations, so it is not a significant issue. We have reworded the text to offer both possibilities as plausible explanations for the positive tail.

3) Section 5 p 19 line 24. There is large variability in climatological SAD in Figure 23 over ~fortnightly intervals in July or August. Does this follow directly from the variability of the climatology of PSC ice at this time (Fig 15c, i.e. a large fraction of total PSC area is ice at the start of August)? Please clarify.

We examined the variability in the climatological SAD in more detail by compiling additional SAD time series excluding ice PSCs and for ice PSCs only. Examination of these clearly show that the large variability in total SAD is indeed driven by the ice variability. There is a strong correspondence between the 1-2 week enhancements seen in renumbered Figure 27 and the enhancements in ice only SAD. The SAD time series with ice PSCs excluded exhibits much less variability. The ice variability is driven by episodic ice events that extend over approximately 1-2 week periods, primarily in July and August. These likely correspond to the tropospheric forcing events mentioned in the text that occur on synoptic scales (e.g. Teitelbaum and Sadourny, 1998; Teitelbaum et al., 2001). In the revised manuscript, we now state that the quasi-periodic nature of the variability in the maximum SAD is due to ice cloud occurrence.

4) Do other Antarctic years show similar changes between v1 and v2, as shown in Figure 10 for 2009?

Yes, other years and groups of years in the Antarctic show similar changes between v1 and v2 to those shown in Fig. 10 (renumbered Fig. 12 in the revised manuscript).

5) Figure 15c. There is a white contour enclosed in the ice PSC in May – June but your colorbar indicates purple as 0.0. Please reconcile or explain in the figure caption.

There is a solid black contour line on each of the color panels in original Figure 15 (renumbered Figure 17) that corresponds to the range of days and altitudes where PSCs (of any composition) were observed in at least six of the twelve Antarctic seasons. This provides an indication of the climatological temporal and altitude extent of the PSC season. For STS and NAT mixtures (Figs 17a-b), PSC onset in at least six years occurred by approximately 20 May. The onset of ice PSCs (Fig. 17c) is delayed until temperatures drop below the frost point which is typically mid-June. The contour is primarily included to illustrate when the onset of ice occurs relative to the other compositions. We have revised the caption to Figure 17 to better explain this contour.

Polar stratospheric cloud climatology based on CALIPSO spaceborne lidar measurements from 2006-2017

Michael C. Pitts¹, Lamont R. Poole², and Ryan Gonzalez^{3, 4}

¹NASA Langley Research Center, Hampton, Virginia, 23681, USA

5 ²Science Systems and Applications, Inc., Hampton, Virginia, 23666, USA

³Universities Space Research Association, NASA Langley Research Center, Hampton, VA, 23681 USA

⁴Now at Department of Atmospheric Science, Colorado State University, Fort Collins, CO, 80523 USA

Correspondence to: Michael C. Pitts (michael.c.pitts@nasa.gov)

10 **Abstract.** The Cloud-Aerosol Lidar with Orthogonal Polarization (CALIOP) on the CALIPSO (Cloud-Aerosol Lidar and
Infrared Pathfinder Satellite Observations) satellite has been observing polar stratospheric clouds (PSCs) from mid-June
2006 until the present. The spaceborne lidar profiles PSCs with unprecedented spatial (5-km horizontal x 180-m vertical)
resolution and its dual-polarization capability enables classification of PSCs according to composition. Nearly coincident
Aura Microwave Limb Sounder (MLS) measurements of the primary PSC condensables (HNO₃ and H₂O) provide additional
15 constraints on particle composition. A new CALIOP Version 2 (v2) PSC detection and composition classification algorithm
has been implemented that corrects known deficiencies in previous algorithms and includes additional refinements to
improve composition discrimination. Major v2 enhancements include dynamic adjustment of composition boundaries to
account for effects of denitrification and dehydration, explicit use of measurement uncertainties, addition of composition
confidence indices, and retrieval of particulate backscatter, which enables simplified estimates of particulate surface area
20 density (SAD) and volume density (VD). The 11+ years of CALIOP PSC observations in each v2 composition class
conform to their expected thermodynamic existence regimes, which is consistent with previous analyses of data from 2006-
2011 and underscores the robustness of the v2 composition discrimination approach.

The v2 algorithm has been applied to the CALIOP dataset to produce a PSC reference data record spanning the 2006-2017
time period, which is the foundation for a new comprehensive, high resolution climatology of PSC occurrence and
25 composition for both the Antarctic and Arctic. Time series of daily-averaged, vortex-wide PSC areal coverage versus
altitude illustrate that Antarctic PSC seasons are similar from year to year, with about 25% relative standard deviation in
Antarctic PSC spatial volume at the peak of the season in July and August. Multi-year average, monthly zonal mean cross
sections depict the climatological patterns of Antarctic PSC occurrence in latitude/altitude and also equivalent
latitude/potential temperature coordinate systems, with the latter system better capturing the microphysical processes
30 controlling PSC existence. Polar maps of the multi-year mean geographical patterns in PSC occurrence frequency show a
climatological maximum between longitudes 90° W and 0°, which is the preferential region for forcing by orography and

upper tropospheric anticyclones. The climatological mean distributions of particulate SAD and VD also show maxima in this region due to the large enhancements from the frequent ice clouds.

Stronger wave activity in the Northern Hemisphere leads to a more disturbed Arctic polar vortex, whose evolution and lifetime vary significantly from year to year. Accordingly, Arctic PSC areal coverage is distinct from year to year with no “typical” year, and the relative standard deviation in Arctic PSC spatial volume is > 100% throughout most of the season. When PSCs are present in the Arctic, they most likely occur between longitudes 60°W and 90°E, which is consistent with the preferential location of the Arctic vortex.

Comparisons of CALIOP v2 and Michelson Interferometer for Passive Atmospheric Sounding (MIPAS) Antarctic PSC observations show excellent correspondence in the overall spatial and temporal evolution, as well as for different PSC composition classes. Climatological patterns of CALIOP v2 PSC occurrence frequency in the vicinity of McMurdo Station, Antarctica, and Ny-Ålesund, Spitsbergen, are similar in nature to those derived from local ground-based lidar measurements. To investigate the possibility of longer term trends, appropriately subsampled and averaged CALIOP v2 PSC observations from 2006-2017 were compared with PSC data during the 1978-1989 period obtained by the spaceborne solar occultation instrument SAM II (Stratospheric Aerosol Measurement II). There was good consistency between the two instruments in column Antarctic PSC occurrence frequency, suggesting that there has been no long-term trend. There was less overall consistency between the Arctic records, but it is very likely due to the high degree of interannual variability in PSCs rather than a long-term trend.

Deleted: , appropriately degraded in resolution and subsampled time-varying latitude,

Deleted: integrated

Deleted:

1 Introduction

The overall role of polar stratospheric clouds (PSCs) in the depletion of stratospheric ozone is well established (Solomon, 1999). Heterogeneous reactions on PSC particles convert the stable chlorine reservoirs HCl and ClONO₂ to chlorine radicals that destroy ozone catalytically (Solomon et al., 1986; Crutzen et al., 1992; Solomon et al., 1999). Rates of these reactions depend on particle surface area density (SAD) and composition, which can include binary (H₂SO₄/H₂O) or ternary (HNO₃/H₂SO₄/H₂O, or STS) liquid droplets; solid nitric acid trihydrate (NAT) particles; and H₂O ice particles (Lowe and MacKenzie, 2008). PSCs also impact polar ozone chemistry by temporarily removing gas-phase HNO₃ from the polar stratosphere through uptake by the particles during formation and growth (denoxification). In addition, sedimentation of large NAT particles (Fahey et al., 2001; Northway et al., 2002; Molleker et al., 2014) can permanently remove HNO₃ (denitrification), which prolongs ozone depletion by delaying reformation of the stable chlorine reservoirs. A substantial recovery of the ozone layer is expected by the middle of this century with reduced global production of ozone depleting substances in accordance with the Montreal Protocol and subsequent amendments and adjustments (WMO, 2015). But as climate changes, leading to a colder and perhaps wetter stratosphere and upper troposphere (e.g., Shindell, 2001), reliable model predictions of recovery of the Antarctic ozone hole and of potentially more severe ozone depletion in the Arctic are

challenging because many global models use simple parameterizations that do not accurately represent PSC processes (e.g. Peter and Grooß, 2012; Morgenstern et al., 2017).

Fortunately, our knowledge of the temporal and geographic distribution of PSCs and their particle composition has expanded greatly in the 21st century with the advent of three satellite instruments with extensive polar measurement coverage: the
5 Michelson Interferometer for Passive Atmospheric Sounding (MIPAS) on Envisat (2002-2012), the Microwave Limb
Sounder (MLS) on Aura (2004-present), and the Cloud-Aerosol Lidar with Orthogonal Polarization (CALIOP) on CALIPSO
(Cloud-Aerosol Lidar and Infrared Pathfinder Satellite Observations, 2006-present). CALIPSO flies in a 98° inclination
orbit at an altitude of 705 km as part of the NASA A-train satellite constellation (Stephens et al., 2002), along with the Aqua,
Aura, CloudSat, and Orbiting Carbon Observatory-2 (OCO-2) satellites. Although PSC studies are not a primary mission
10 objective, CALIPSO is an ideal platform for studying polar processes, collecting data along 14-15 orbits per day with
coverage from 82° S to 82° N latitude on each orbit. CALIOP data collection began in mid-June 2006 and continues at the
time of this writing.

The foundation for PSC detection and composition classification using CALIOP data was laid out in papers by Pitts et al.
(2007) and Pitts et al. (2009), with additional refinements appearing in Pitts et al. (2011) and Pitts et al. (2013). We will
15 refer to these papers herein as P07, P09, P11, and P13, respectively, and refer to the P07/P09/P11/P13 algorithm sequence as
Version 1.0 (v1). Data products from v1 have compared favorably with PSC observations from MIPAS (Höpfner et al.,
2009), ground-based lidar (Achtert and Tesche, 2012), and Aura MLS (P13; Lambert et al, 2016). However, several known
deficiencies in the v1 algorithm were highlighted in P13, one being that the effects of measurement noise on the inferred
PSC composition were not explicitly considered. In addition, the boundary separating NAT and ice PSCs in the CALIOP
20 optical measurement space needed to be adjusted in the event of denitrification and dehydration, a shortcoming that was also
noted in comparisons of v1 products with model simulations by Zhu et al. (2017).

In the present paper, we introduce the CALIOP Version 2.0 (v2) PSC algorithm, which addresses these known deficiencies
and includes additional refinements to increase the robustness of the inferred PSC composition. These refinements include:
(1) correction for crosstalk between the CALIOP parallel and perpendicular polarization channels; (2) estimation of random
(3) adoption of less conservative PSC detection thresholds to better match features detected by the naked eye in CALIOP
orbital curtain images; (4) redefined PSC composition classes with indices denoting statistical confidence in the inferred
composition; and (5) retrieval of 532-nm particulate backscatter, which corrects the CALIOP measurements for attenuation
by overlying particle layers and enables simplified estimates of the bulk particle microphysical quantities SAD and volume
25 density (VD) to facilitate comparisons with PSC measurements by other instruments as well as with theoretical model
representations of heterogeneous chemical processes. We show several examples that illustrate the top-level differences
between v1 and v2 data products. We then present a state-of-the-art PSC reference data record and climatology constructed
30

by applying the v2 algorithm to the 11+ year CALIOP spaceborne lidar dataset spanning 2006-2017. This work is part of a larger effort to compile new reference PSC climatologies based on the contemporary CALIOP, MIPAS, and MLS datasets that is being performed under the auspices of the Stratospheric-tropospheric Processes and their Role in Climate (SPARC) Polar Stratospheric Cloud initiative (PSCi: <http://www.sparc-climate.org/activities/polar-stratospheric-clouds/>). A separate

5 MIPAS PSC climatology has been compiled by Spang et al. (2018). These new climatologies represent the first observational-based records of PSC occurrence, composition, and particle characteristics on vortex-wide spatial scales covering decadal time scales and are a valuable resource for testing and validating current and future global models.

In Section 2 we describe the datasets utilized in the CALIOP v2 PSC algorithm and in constructing the CALIOP PSC climatology. In Section 3 we describe in detail the modifications implemented in the v2 algorithm, illustrate the top-level

10 differences between v1 and v2, and show that the v2 PSC composition classes conform well to their expected temperature existence regimes. In Section 4 we present the CALIOP v2 PSC reference data record and climatology in terms of overall and composition-specific areal coverage and occurrence frequency. Multi-year average, monthly zonal mean cross sections in both latitude/altitude and equivalent latitude/potential temperature coordinate systems are shown along with polar maps that illustrate the detailed temporal and spatial patterns in PSC occurrence and composition. In Section 5 we show examples

15 of the SAD climatology. In Section 6 we [discuss comparisons of CALIOP with MIPAS and ground-based lidar PSC observations and](#) investigate the possibility of long-term trends in PSC occurrence by comparing the CALIOP data record to the historical (1978-1989) SAM II (Stratospheric Aerosol Measurement II) solar occultation PSC occurrence record. Finally, in Section 7 we summarize the key findings and discuss the results.

2 Datasets

20 The A-Train satellite constellation offers a unique opportunity for PSC analyses through the combination of CALIOP data and nearly coincident Aura MLS measurements of the primary PSC condensable vapors, HNO_3 and H_2O . Additional context is provided by ancillary meteorological information from the Modern Era Retrospective-Analysis for Research (MERRA-2) reanalysis products (Gelaro et al., 2017) and the Aura MLS Derived Meteorological Products (DMPs) (Manney et al., 2007; Manney et al., 2011a). A brief description of these datasets is provided below.

2.1 CALIOP

25 CALIOP, the primary instrument on the CALIPSO satellite, is a dual wavelength polarization-sensitive lidar that provides high vertical resolution profiles of backscatter coefficients at 532 and 1064 nm (Winker et al., 2009). Figure 1 illustrates the typical CALIPSO orbital coverage for a single day (17 July 2008) over the Antarctic polar region. A curtain of CALIOP 532-nm total attenuated backscatter coefficient measurements along a single orbit from this day is shown in Fig. 2 and

30 illustrates the unique capability of the CALIOP spaceborne lidar to probe clouds and aerosols at very high spatial resolution.

Although not specifically designed for stratospheric applications, PSCs generally produce detectable enhancements in CALIOP backscatter profiles as can be seen at altitudes above ~12 km along the orbit curtain in Fig. 2. The CALIOP measurements of 532-nm perpendicular backscatter coefficient provide additional information on particle shape, from which PSC composition can be inferred. The v2 CALIOP PSC data products are derived from night-time-only CALIOP v4.10 Level 1B 532-nm parallel and perpendicular backscatter coefficient measurements; daytime measurements contain elevated background noise due to scattered sunlight, which greatly inhibits the detection of PSCs. Ancillary meteorological data from MERRA-2, including temperature, pressure, ozone number density, and tropopause height at the CALIOP measurement locations are included in the CALIOP v4.10 Level 1B data products and utilized in the PSC algorithm as described in Section 3. Further details on the CALIPSO v4.10 Level 1 data processing and calibration approach can be found in Kar et al. (2018).

2.2 Aura MLS

The Aura satellite flies in formation with CALIPSO in the A-train satellite constellation providing a nearly coincident dataset of gas-phase HNO_3 and H_2O from the MLS instrument with spatial and temporal differences between the CALIOP and MLS measurements less than 10 km and 30 s after a repositioning of the Aura satellite in April 2008 and about 200 km and 7-8 min. prior to 2008 (see Lambert et al., 2012). The Aura MLS detects thermal microwave emission from the Earth's limb along the line-of-sight in the forward direction of the Aura spacecraft flight track (Waters et al., 2006). Vertical scans are made from the Earth's surface up to a 90 km tangent height every 24.7 s, providing a total of 3500 vertical profiles per day with a horizontal along track spacing of 1.5 degrees (~165 km) and nearly global latitude coverage from 82° S–82° N. The limb radiance measurements are inverted using a 2-D optimal estimation retrieval (Livesey et al., 2006) to yield atmospheric profiles of temperature and gas-phase constituents in the vertical range 8–90 km. Herein we use the MLS version 4.2 products (Livesey et al., 2017). For the vertical range relevant for PSCs, the MLS version 4.2 measurements have typical single-profile precisions (accuracies) of 4-15% (4-7%) for H_2O (Read et al. 2007; Lambert et al., 2007) and 0.6 ppbv (1-2 ppbv) for HNO_3 (Santee et al., 2007). Vertical and horizontal along-track resolutions are 3.1-3.5 km and 180-290 km for H_2O , and 3.5-5.5 km and 400-550 km for HNO_3 .

The Aura MLS Version 2 (v2) derived meteorological products (DMPs) (Manney et al., 2007; Manney et al., 2011a) have been calculated from the MERRA-2 reanalyses and consist of meteorological variables (winds, temperature, potential temperature, potential vorticity) and derived fields (e.g., equivalent latitude and vortex edge location) interpolated to the locations and times of the Aura MLS observations.

To better facilitate the utilization of the MLS data in the PSC analyses, the MLS gas-phase HNO_3 and H_2O measurements are interpolated to the CALIOP PSC orbit grid using an average of the two nearest MLS profiles weighted by the inverse of the relative distance of each to the CALIPSO location. In addition, meteorological parameters from the Aura MLS v2.0

DMPs are also mapped onto the CALIOP PSC orbit grid. The MLS HNO_3 and H_2O , and meteorological parameters from the DMPs are included in the archived v2 CALIOP PSC data product files.

3 CALIOP Version 2.0 PSC Algorithm

3.1 Data Pre-processing

Data pre-processing generally follows the procedure discussed in detail in P07 and P09, but with additional steps (see Appendix A) to correct for the small amount of crosstalk between the two CALIOP polarization channels and to estimate uncertainties $[u(x)]$ in the basic CALIOP measurements and derived quantities. The initial step is to ingest nighttime-only profiles of CALIOP V4.10 Lidar Level 1B 532-nm attenuated parallel (β'_{\parallel}) and perpendicular (β'_{\perp}) backscatter coefficients over the altitude range 8.4-30 km. The data are smoothed to a uniform 5-km horizontal (along the orbit track) by 180-m vertical resolution grid to remove the altitude dependence of the resolution of the downlinked CALIOP data (Winker et al., 2007). The data are then corrected for molecular and ozone attenuation using the MERRA-2 molecular and ozone number density profiles reported in the CALIOP V4.10 Level 1B data product files. The MERRA-2 molecular number density is also used in the theoretical relationship from Hostetler et al. (2006) to calculate molecular backscatter β_{mol} , which is then used to calculate the 532-nm attenuated scattering ratio

$$R'_{532} = (\beta'_{\parallel} + \beta'_{\perp}) / \beta_{\text{mol}} \quad (1)$$

3.2 PSC Detection

Detection of PSCs in the v2 algorithm generally follows the approach of v1 in that PSCs are detected as statistical outliers in either β'_{\perp} or R'_{532} relative to the background stratospheric aerosol population. We also use successive horizontal averaging (5, 15, 45, and 135 km) to ensure that strongly scattering PSCs (e.g., fully developed STS and ice) are found at the finest possible spatial resolution while also enabling the detection of more tenuous PSCs (e.g., low number density liquid-NAT mixtures) through additional averaging. PSC features found at finer spatial resolution are masked out of the profiles of β'_{\perp} and R'_{532} that undergo additional averaging. Successive averaging minimizes optical aliasing that can result from grouping fine-resolution pixels having vastly different optical properties into a single coarser-resolution average.

Visual comparison of many CALIOP v1 orbital composition images (e.g., Fig. 13 of P11) with corresponding images of β'_{\perp} and R'_{532} indicated that the PSC statistical thresholds used in the v1 algorithm were too conservative, so we have made appropriate adjustments in v2. The thresholds for the background aerosol - assumed to be those data at MERRA-2 temperatures above 200 K - are now defined as the daily median plus one median absolute deviation of β'_{\perp} and R'_{532} . These are computed in overlapping 100 K-thick potential temperature (θ) layers over the range from $\theta = 250$ -750 K. The region of the South Atlantic Anomaly, defined here as a wedge between longitudes 60° W and 45° E, is excluded from the background

Deleted: , such as dynamic tropopause height, equivalent latitude and vortex edge location

Deleted: 3.1.1 Crosstalk Correction¶

The CALIOP backscatter signal is separated into parallel and perpendicular components by a polarization beam splitter in the receiver subsystem (Hunt et al., 2009). With an ideal beam splitter the measured molecular depolarization ratio ($\delta_{\text{mol,meas}}$) would equal the theoretical value of 0.00366 at the ~40-pm bandwidth of the CALIOP optical filter (Cairo et al. 1999; Hostetler et al., 2006). The difference between the measured and theoretical molecular depolarization ratios indicates the level of crosstalk (CT) between the two polarization channels. We assume for simplicity that a fraction CT of the received parallel signal is reflected into the perpendicular channel and that the remainder (1-CT) of the received parallel signal is transmitted into the parallel detector. With this assumption and some algebraic manipulation, it can be shown that

$$\text{CT} = (\delta_{\text{mol,meas}} - 0.00366) / (1 + \delta_{\text{mol,meas}}) \quad (2)$$

The crosstalk-corrected attenuated backscatter signals can then be derived from the measured signals as follows:¶

$$\beta'_{\parallel} = \beta'_{\parallel,\text{meas}} / (1 - \text{CT}) \quad (3)¶$$

$$\beta'_{\perp} = \beta'_{\perp,\text{meas}} - \beta'_{\parallel}(\text{CT}) \quad (4)¶$$

Based on daily values of $\delta_{\text{mol,meas}}$ from mid-June 2006 until March 2015, we found that CT has been less than 0.005 over almost the entire CALIPSO mission. The only exceptions were the 2008 Antarctic and 2008-09 Arctic winters, when CT ranged from 0.003 to 0.007. Since the CT correction is so small, we use PSC seasonal average CT values for simplicity in our algorithm. The value of CT since March 2015 is assumed to be equal to the 2014-15 Arctic winter average value of 0.0025.¶

3.1.2 Random Measurement Uncertainties¶

Random uncertainties in β'_{\parallel} [$u(\beta'_{\parallel})$] and β'_{\perp} [$u(\beta'_{\perp})$] due to shot noise are computed using the noise scale factor (NSF) approach introduced by Liu et al. (2006) and described in detail for the CALIOP system by Hostetler et al. (2006). The uncertainties are scaled by the inverse square root of the product of: the number of 15-m vertical bins being averaged, which is 12 in the case of our fixed 180-m vertical resolution, and the number of 1/3-km horizontal resolution laser shots being averaged, which ranges from 15 to 40 in our successive horizontal averaging scheme. Relative random uncertainty in R'_{532} [$u(R'_{532})/R'_{532}$] is calculated as the square root of the sum of squares of the relative random uncertainties in β'_{\parallel} [$u(\beta'_{\parallel})/\beta'_{\parallel}$] and β'_{\perp} [$u(\beta'_{\perp})/\beta'_{\perp}$] plus an assumed 3% relative uncertainty in β_{mol} (Hostetler et al., 2006). The basic random uncertainties are propagated through the calculation of other optical quantities, e.g. particulate depolarization ratio ($\delta_{\text{particulate}}$), to estimate their uncertainties as well. ¶

aerosol threshold calculations due to excessive noise in the CALIOP 532-nm data in this region (Hunt et al., 2009). Then for a candidate CALIOP data point to be identified as a PSC, its value of β'_{\perp} (or R'_{532}) must exceed the background aerosol threshold by at least $u(\beta'_{\perp})$ (or $u(R'_{532})$). We also impose a spatial coherence test that requires that more than 11 of the points in a 5-point horizontal by 3-point vertical box centered on the candidate feature exceed the current PSC detection threshold or to have been identified as a PSC at a previous (finer) averaging scale. This revised approach does a better job overall of capturing PSC clusters identified by the naked eye in CALIOP orbital images while continuing to eliminate false PSC identifications stemming from positive noise spikes in the data. Spot checks of the v2 Antarctic PSC database from early May - when no PSCs observations are expected - indicate that the v2 false positive rate is much less than 0.01%.

Tropopause height information included in the CALIOP Level 1b lidar data product files is based on the MERRA-2 “blended” tropopause altitudes. The MERRA-2 “blended” tropopause is the lower (in altitude) of the temperature-based (“thermal”) tropopause and potential vorticity (PV) based (“dynamic”) tropopause (Bosilovich et al., 2016; Ott et al., 2016). In practice, the MERRA-2 “blended” tropopause is usually the “dynamic” tropopause in mid- and high-latitudes, but switches to the “thermal” tropopause in the tropics. The tropopause is often difficult to locate in the polar regions, especially during the polar nights (e.g., Highwood et al., 2000), so any tropopause height determination in these regions should be used with caution. In fact, it is our experience that the transition from upper tropospheric cirrus to PSCs is often ambiguous with no clear separation across the reported tropopause. Consequently, using the MERRA-2 tropopause as a hard boundary to separate tropospheric cirrus from PSCs will certainly lead to misclassifications. Hence, we make no explicit attempt to distinguish tropospheric cloud from stratospheric cloud in the 8.5-30 km altitude range over which we produce the CALIOP PSC cloud mask. However, we do tag each observation in the database with a feature flag that identifies its altitude location relative to the reported “blended” tropopause as one of three possibilities: (1) below the tropopause, (2) between the tropopause and tropopause + 4 km, or (3) above the tropopause + 4 km. This allows data users to perform some crude separation between tropospheric and stratospheric cloud as desired.

3.3 PSC Composition Classification

PSC composition classification is based on comparing CALIOP data with temperature-dependent theoretical optical calculations for non-equilibrium mixtures of liquid (binary $\text{H}_2\text{SO}_4\text{-H}_2\text{O}$ or STS) droplets and NAT or ice particles. To illustrate the differences between the v2 and v1 algorithms, we show a more extensive set of theoretical results for 50 hPa atmospheric pressure, 10 ppbv HNO_3 , and 5 ppmv H_2O . For these conditions, the NAT equilibrium temperature $T_{\text{NAT}} \equiv 195.7$ K (Hanson and Mauersberger, 1988); T_{STS} , the temperature at which liquid particle volume starts to increase markedly $\equiv 192$ K (Carslaw et al., 1995); and the frost point temperature $T_{\text{ice}} \equiv 188.5$ K (Murphy and Koop, 2005). The total particle number density (N_{total}) is fixed at 10 cm^{-3} (Weigel et al., 2014), partitioned between liquid droplets (N_{liq}) and either NAT (N_{NAT}) or ice (N_{ice}) for the various mixtures being considered. The liquid particle size distribution is assumed to be a single-mode lognormal with geometric standard deviation $\sigma=1.6$, whose mode radius is calculated as a function of N_{liq} and the

equilibrium condensed liquid particle VD (Carslaw et al., 1995) for temperatures $T_{\text{ice}} - 3 \text{ K} < T < 196 \text{ K}$. We assume that non-equilibrium liquid-NAT mixtures exist at $T < T_{\text{NAT}}$ and that non-equilibrium liquid-ice mixtures exist at $T < T_{\text{ice}}$ and that both NAT and ice particle size distributions are single-mode lognormals with $\sigma=1.38$. We consider a range of $N_{\text{NAT}} (N_{\text{ice}})$ from $0.0001\text{-}1.0 \text{ cm}^{-3}$ ($0.001\text{-}10 \text{ cm}^{-3}$) and a range of volume-equivalent radii (r_{NAT} and r_{ice}) from $0.25\text{-}15 \text{ }\mu\text{m}$. However, only those combinations of $[N, r]$ with NAT (ice) particle volumes less than or equal to the temperature-dependent equilibrium NAT (ice) volume are physically possible. For the liquid-NAT mixtures, $N_{\text{liq}} = N_{\text{total}} - N_{\text{NAT}}$, and the equilibrium liquid particle VD is reduced to account for the condensed HNO_3 and H_2O in the co-existing NAT particles. For the liquid-ice mixtures, $N_{\text{liq}} = N_{\text{total}} - N_{\text{ice}}$, and the equilibrium liquid particle VD is reduced to account for the condensed H_2O in the co-existing ice particles. All particle optical properties were calculated using the database of T-matrix results compiled by Scarchilli et al. (2005) and based on the original work of Mishchenko and Travis (1998), with fixed refractive indices of $1.44 + i0.0$ for binary $\text{H}_2\text{SO}_4\text{-H}_2\text{O}$ and STS, $1.48 + i0.0$ for NAT, and $1.31 + i0.0$ for ice. We assumed spherical liquid droplets (aspect ratio = 1.0) and assumed both NAT and ice particles to be prolate spheroids with an aspect (diameter-to-length) ratio of 0.9, which Engel et al. (2013) showed to produce best agreement with maximum values observed by CALIOP of particulate depolarization ratio $\delta_{\text{particulate}}$:

$$\delta_{\text{particulate}} = \beta_{\perp, \text{particulate}} / \beta_{\parallel, \text{particulate}} = [\beta_{\perp} - \delta_{\text{mol}} \beta_{\text{mol}}] / [\beta_{\parallel} - (1 - \delta_{\text{mol}}) \beta_{\text{mol}}] \quad (2)$$

where δ_{mol} is the theoretical molecular depolarization ratio = 0.00366 (see Appendix A).

Figure 3 shows the theoretical results plotted in the coordinate system of $\delta_{\text{particulate}}$ vs. inverse scattering ratio ($1/R_{532}$) used in the v1 algorithm. In v1, it was assumed implicitly that attenuation of the CALIOP laser beam due to PSC particles themselves was negligible, i.e. that R'_{532} and β'_{\perp} could be considered equivalent to R_{532} and β_{\perp} for the purpose of composition classification. The individual “streaks” of points in Fig. 3 represent physically possible $[N_{\text{NAT}}, r_{\text{NAT}}]$ or $[N_{\text{ice}}, r_{\text{ice}}]$ combinations, with temperature decreasing from upper left to lower right along each streak. P09 defined fixed $\delta_{\text{particulate}}$ vs. $1/R_{532}$ boundaries separating the composition classes STS, ice (our abbreviated name for liquid-ice mixtures), and Mix1 and Mix2, the latter denoting liquid-NAT mixtures with lower and higher NAT number densities/volumes, respectively. P11 added two additional subclasses: Mix2-enhanced, those liquid-NAT mixtures with optical properties ($2 < R_{532} < 5$ and $\delta_{\text{particulate}} > 0.1$) similar to the so-called Type 1a enhanced clouds observed during earlier airborne field missions (e.g., Tsias et al., 1999); and wave ice, PSCs presumably induced by mountain waves. P11 defined wave ice conservatively as those PSCs with $R_{532} > 50$, but noted that the subclass is not all-inclusive, i.e. some additional ice PSCs are likely associated with mountain waves, but do not meet the stringent ($R_{532} > 50$) wave-ice classification criterion. P13 changed the boundary separating STS from liquid-NAT mixtures and ice to a β_{\perp} threshold instead of a fixed value of $\delta_{\text{particulate}}$; hence that boundary is shown as a dashed magenta line in Fig. 3. For comparison purposes, Fig. 3 also shows a dashed purple curve representing the lower boundary of the v2 “enhanced NAT mixtures” class, as discussed below.

Deleted: ; and Mix2-enhanced, liquid-NAT mixtures with optical properties ($2 < R_{532} < 5$ and $\delta_{\text{particulate}} > 0.1$) similar to the so-called Type 1a enhanced clouds observed downstream of wave ice PSC during earlier airborne field missions (e.g., Tsias et al., 1999). the subclass is not all-inclusive, i.e. some additional ice PSCs are likely associated with mountain waves, but do not meet the stringent ($R_{532} > 50$) wave-ice classification criterion.

Two known deficiencies in the v1 composition classification scheme were pointed out in P13. Due to uncertainty in the CALIOP measurements, the optical space boundaries between PSC composition classes are actually “fuzzy” rather than sharp. Thus, toggling between inferred composition classes over small spatial scales may be due to measurement noise rather than a true change in composition. This is especially true in the case of separating liquid-NAT mixtures into the Mix1, Mix2, and Mix2-enhanced categories. P13 also pointed out that the boundary separating ice and liquid-NAT mixtures must be shifted to larger values of $1/R_{532}$ (smaller values of R_{532}) in the event of denitrification and dehydration to avoid ice PSCs being misclassified as liquid-NAT mixtures (also noted by Zhu et al., 2017). To address these deficiencies, we have significantly improved the composition classification scheme in v2. The improvements are discussed below in the context of Fig. 4, where the theoretical optical results are re-plotted in the coordinate system β_{\perp} vs. R_{532} , surrogates for the measured attenuated CALIOP quantities β'_{\perp} and R'_{532} used for PSC detection. As discussed below in Section 3.4, the v2 algorithm also incorporates a retrieval of 532-nm particulate backscatter, $\beta_{\text{particulate}}$, through which β'_{\perp} and R'_{532} are later corrected for attenuation due to overlying particulate layers (i.e. the “primes” are removed), allowing for a more robust comparison with the theoretical results. The families of points representing physically possible $[N_{\text{NAT}}, r_{\text{NAT}}]$ or $[N_{\text{ice}}, r_{\text{ice}}]$ pairs lie at constant β_{\perp} in Fig. 4, with temperature again decreasing from left to right along each family of points. The following points are to be noted in our revised algorithm:

- The former Mix1 and Mix2 classes of liquid-NAT mixtures have been combined into a single class named “NAT mixtures” for brevity. (Note that the line and curve separating Mix1 and Mix2 in Fig. 3 disappears with the v2 definition of NAT mixtures.)
- The former Mix2-enhanced class has been renamed “enhanced NAT mixtures” and it is now defined as the sub-class of NAT mixtures with $R_{532} > 2$ and $\beta_{\perp} > 2 \times 10^{-5} \text{ km}^{-1} \text{sr}^{-1}$. This conservative boundary was determined empirically by comparing CALIOP Antarctic PSC data to contemporaneous MIPAS observations with and without a belt of NAT clouds formed by heterogeneous nucleation on wave ice PSCs over the Antarctic Peninsula (Höpfner et al., 2006). MIPAS data from 2008 May 27/28/30 (M. Höpfner, Karlsruhe Institute of Technology, private communication) showed no evidence of these NAT clouds, and only about 2% of CALIOP NAT mixture data from those days had $R_{532} > 2$ and $\beta_{\perp} > 2 \times 10^{-5} \text{ km}^{-1} \text{sr}^{-1}$. In contrast, NAT belt clouds were clearly evident in MIPAS data on 2008 May 29 and 2008 June 01/02, and their locations were matched extremely well by CALIOP NAT mixtures with $R_{532} > 2$ and $\beta_{\perp} > 2 \times 10^{-5} \text{ km}^{-1} \text{sr}^{-1}$. In theoretical terms, CALIOP enhanced NAT mixture points correspond roughly to those NAT mixtures with $r_{\text{NAT}} < 3 \text{ }\mu\text{m}$ and NAT VD $> 1.0 \text{ }\mu\text{m}^3 \text{cm}^{-3}$, which match the MIPAS NAT detection limits ($r_{\text{NAT}} < 3 \text{ }\mu\text{m}$ and NAT VD $> 0.3 \text{ }\mu\text{m}^3 \text{cm}^{-3}$) reasonably well. Since our criteria defining enhanced NAT mixtures are conservative, the enhanced NAT mixtures sub-class is not all-inclusive, i.e., it does not capture all NAT mixture PSCs heterogeneously nucleated in wave ice PSCs.

Deleted: 98

Deleted: \leq

Deleted: \leq

- The wave ice class remains the same as in P11, i.e. ice PSCs with $R_{532} > 50$. We reemphasize that this definition of wave ice is not all-inclusive, i.e. some additional ice PSCs are likely associated with mountain waves, but do not meet our stringent wave-ice classification criterion.
- The dashed horizontal line labeled $\beta_{\perp, \text{thresh}}$ represents qualitatively the CALIOP statistical threshold for detection of PSCs containing non-spherical particles. In practice, this threshold changes with horizontal averaging scale and differs from point to point due to its dependency on $u(\beta_{\perp})$. Each data point is assigned a non-spherical particle confidence index $CI_{\text{NS}} = [\beta_{\perp} - u(\beta_{\perp})]/u(\beta_{\perp})$. Points with $CI_{\text{NS}} > 1$ are presumed to be PSCs containing non-spherical particles.
- The dashed magenta vertical line labeled R_{thresh} represents qualitatively the CALIOP statistical threshold for detection of liquid PSCs. In practice, R_{thresh} also changes with horizontal averaging scale and differs from point to point due to its dependency on $u(R_{532})$. Data points classified as STS are those with $CI_{\text{NS}} \leq 1$, but with $R_{532} > R_{\text{thresh}}$. Each is assigned an STS confidence index $CI_{\text{STS}} = [R_{532} - u(R_{532})]/u(R_{532})$; $CI_{\text{STS}} > 1$.
- Note that in practice, there is not a distinct separation between histograms of β_{\perp} for v2 STS and NAT mixtures. We estimate that 10-15% of data points in either class may fall in the overlap region and thus could be misclassified.
- Points in the grey box at the lower left fall below both CALIOP PSC detection thresholds and are classified as non-features. It should be noted that all measured and derived quantities for non-features are also retained in the v2 data product. A comprehensive discussion of so-called “sub-visible” PSCs can be found in the paper by Lambert et al. (2016), who show that they often can be detected through gas-phase uptake of HNO_3 as observed by MLS even though they are not detectable as PSCs by CALIOP.
- The position of the boundary separating NAT mixtures and enhanced NAT mixtures from ice (labeled $R_{\text{NAT|ice}}$) now is calculated dynamically according to the total abundances of HNO_3 and H_2O vapors. $R_{\text{NAT|ice}}$ is based on a parameterization of theoretical calculations of R_{532} for fully developed STS (assumed to be points between T_{ice} and $T_{\text{ice}} - 1$ K) over a wide range of atmospheric pressures and HNO_3 and H_2O mixing ratios. Total HNO_3 and H_2O abundances are determined on a daily basis as a function of altitude and DMP equivalent latitude based on nearly coincident “cloud-free” Aura MLS data, where the CALIOP PSC data themselves are used to filter out MLS data affected by uptake in the cloud particles. Then each point with $CI_{\text{NS}} > 1$ is assigned a NAT|ice confidence index $CI_{\text{NAT|ice}} = (R_{532} - R_{\text{NAT|ice}})/u(R_{532})$. For points classified as ice or wave ice, $CI_{\text{NAT|ice}} > 0$. For NAT mixtures or enhanced NAT mixtures, $CI_{\text{NAT|ice}} < 0$.
- The v2 composition classification extends downward in altitude to the 215 hPa pressure level (~10 km), the lowest reliable level for Aura MLS HNO_3 data that is required to define the location of the NAT mixture/ice boundary ($R_{\text{NAT|ice}}$) in our classification scheme. All clouds at altitudes below this pressure level are assumed to be ice.
- To illustrate that these theoretical calculations resemble actual measurements, composite 2-D histograms of CALIOP PSC data from 10-18 July 2008 (which includes the orbital curtain of Fig. 2) are shown in Figs. 5 and 6 for the v1 and v2 coordinate systems, respectively. In the interest of examining a quasi-homogeneous ensemble, the data have been restricted to latitudes from 65° S to 75° S and θ from 475 K to 525 K. The most noteworthy feature in Fig. 5 is that the separation

Deleted:

between NAT mixtures and ice is not at the fixed value of $1/R_{532} = 0.2$ used in the v1 algorithm, but instead occurs at $1/R_{532} \approx 0.25$ -0.35. The separation appears to be better captured in Fig. 6, where the average dynamically calculated $R_{\text{NATice}} \approx 2.75$ as a result of denitrification and dehydration.

3.4 Retrieval of 532-nm Particulate Backscatter

- 5 By retrieving the 532-nm particulate backscatter, $\beta_{\text{particulate}}$, the observed quantities β'_{\perp} and R'_{532} can be corrected for attenuation due to overlying particulate layers (i.e. the “primes” are removed). This allows for a more robust comparison with the theoretical results and final adjustments in $u(\beta'_{\perp})$, $u(R'_{532})$, and the assigned PSC composition class. It also enables the development of approximate relationships (Section 3.5) relating $\beta_{\text{particulate}}$ to the bulk particle microphysical quantities SAD and VD. The retrieval procedure we have implemented in v2 follows the general CALIOP particulate extinction retrieval approach outlined by Young and Vaughan (2009). The CALIOP total attenuated 532-nm backscatter profile, with the correction for molecular and ozone attenuation previously applied, can be expressed as follows:

$$\beta'(z) = [\beta_{\text{particulate}}(z) + \beta_{\text{mol}}(z)] \exp[-2\eta(z)\pi(0,z)_{\text{particulate}}] \quad (3)$$

where $\pi(0,z)_{\text{particulate}}$ is the particulate optical depth between the lidar (altitude 0) and altitude z , and $\eta(z)$ is a factor accounting for multiple scattering. By definition,

$$\pi(0,z)_p = \int_0^z \alpha_{\text{particulate}}(z) dz' \quad (4)$$

where $\alpha_{\text{particulate}}(z)$ is the particulate extinction coefficient.

- Making the usual assumption that $\alpha_{\text{particulate}} = S_{\text{particulate}} \times \beta_{\text{particulate}}$, where $S_{\text{particulate}}$ is the particulate extinction-to-backscatter (lidar) ratio, leads to an equation of the form $\beta_{\text{particulate}}(z) = f\{\beta_{\text{particulate}}(z)\}$, which is solved bin by bin in PSCs layers using an unconstrained top-down Newtonian iterative numerical approach as discussed by Young and Vaughan (2009). The multiple scattering factor $\eta(z)$ is calculated as a function of temperature from a spline fit to results from Garnier et al. (2015) for semi-transparent cirrus clouds; for temperatures <190 K (>240 K) $\eta(z)$ is fixed at 0.9 (0.5). Based on ground-based 355-nm lidar measurements in a mountain-wave PSC event at Esrange, Sweden, Reichardt et al. (2004) derived layer-average values of $S_{\text{particulate}}$ ranging from 67-82 sr (20-35 sr) for PSC layers with small (large) scattering ratios. These are consistent with 532-nm $S_{\text{particulate}}$ values of 50-80 sr derived by Prata et al. (2017) for binary H_2SO_4 - H_2O aerosols and with values of 14-26 sr derived by Platt et al. (2011) for cold (-80 °C) high-altitude cirrus. For implementation in the v2 algorithm, we derived a parameterization based on the theoretical results described in Section 3.3 for binary H_2SO_4 - H_2O and STS droplets by which $S_{\text{particulate}}$ varies smoothly between the observed bounds:

$$S_{\text{particulate}} = 16 + 66/R_{532} - 12/(R_{532})^2 \quad (5)$$

Deleted: any necessary

Deleted: σ

Deleted: σ

Deleted: σ

Deleted: =

Deleted: In the absence of data on $S_{\text{particulate}}$ for

Deleted: PSCs, we assume it is bounded by values

Deleted: observed

Deleted: (50-80 sr; Prata et al. (2017)) as R_{532} approaches 1,

Deleted: and by values observed

Deleted: (14-26 sr; Platt et al. (2011)) at very large R_{532}

Deleted:

Deleted: Based on the theoretical results described in Section 3 for binary H_2SO_4 - H_2O and STS droplets,

Deleted: these

Deleted: limits

Deleted: :

Deleted: 7

The minimum value of $S_{\text{particulate}}$ was set at 16 to ensure that retrievals did not terminate at altitudes above where PSCs were detected in the CALIOP Level 1 attenuated backscatter data.

3.5 Estimation of Particle SAD and VD

To estimate SAD and VD using CALIOP data, we followed the methodology applied to stratospheric aerosols by Gobbi (1995), in which functional relationships linking $\beta_{\text{particulate}}$, SAD, and VD were determined by averaging the scattering properties of a large set of stratospheric aerosol size distributions. Actual PSC particle size measurements are somewhat limited and have often been obtained under mountain wave conditions (e.g., Deshler et al., 2003; Schreiner et al., 2003; Voigt et al., 2003), and there is little or no information on the actual shapes of NAT or ice PSC particles. Therefore, we made the simplifying assumption that useful functional relationships could be based on the averaged scattering properties of

a range of size distributions for liquid spherical H_2SO_4 - H_2O and STS particles, the characteristics of which are much better constrained. As described in Section 3.3, the equilibrium VD for H_2SO_4 - H_2O or STS particles can be calculated as a function of temperature for given atmospheric pressure and HNO_3 and H_2O mixing ratios from Carslaw et al (1995). Assuming a single-mode lognormal size distribution with number density N_{liq} and geometric standard deviation σ , the mode radius and SAD can then be calculated from VD using standard relationships between lognormal moments (e.g., Heintzenberg, 1994).

With the particle size distribution fully specified, $\beta_{\text{particulate}}$ can be calculated using the database of optical properties for spherical particles compiled by Sarchilli et al. (2005). To explore the sensitivity of the results to size distribution parameters, we performed calculations for other values of N_{liq} (5 and 15 cm^{-3} ; Wilson et al., 1990; Campbell and Deshler, 2014) and σ (1.3 and 1.8) in addition to our standard conditions of $N_{\text{liq}}=10 \text{ cm}^{-3}$, $\sigma=1.6$, 50 hPa atmospheric pressure, 10 ppbv HNO_3 , and 5 ppmv H_2O . The results are shown in Figs. 7 and 8, along with the 3rd order polynomial least-squares fits

to the two sets of curves. Note that increases (decreases) in atmospheric pressure, HNO_3 , or H_2O do not produce different curves, but shift the results for a given curve to the right (left). The RSS uncertainty in liquid particle SAD due to measurement error and lack of knowledge of the size distribution parameters N_{liq} and σ is on the order of ± 1 (± 2.5 , ± 5) $\mu\text{m}^2\text{cm}^{-3}$ for $\beta_{\text{particulate}} = 10^{-5}$ (10^{-4} , 5×10^{-4}) $\text{km}^{-1}\text{sr}^{-1}$. The corresponding RSS uncertainty in liquid particle VD is on the order of ± 0.05 (± 0.15 , ± 1.0) $\mu\text{m}^3\text{cm}^{-3}$ for $\beta_{\text{particulate}} = 10^{-5}$ (10^{-4} , 5×10^{-4}) $\text{km}^{-1}\text{sr}^{-1}$.

These liquid particle approximate expressions can be applied to the full suite of CALIOP data, including “sub-visible” PSCs as well as background aerosols. However, there are large uncertainties in the case of NAT mixtures and ice PSCs due to the dearth of information on NAT or ice particle size and shape. Figures 9 and 10 show the complex behavior of SAD and VD versus $\beta_{\text{particulate}}$ from the full set of theoretical results for NAT mixtures and ice discussed in Section 3.3 and compare those to the liquid particle approximations shown in Figs. 7 and 8. For a given value of $\beta_{\text{particulate}}$, the liquid particle approximation for SAD is an upper limit for the actual SAD in NAT mixtures and a lower limit for the actual SAD in ice PSCs. The level of over/underestimation of SAD may be as much as a factor of 3. For a given value of $\beta_{\text{particulate}}$, the liquid particle approximation for VD is a lower limit for the actual VD in ice PSCs and in most NAT mixtures, the exception being those with small r_{NAT} ($< \sim 1.5 \mu\text{m}$). The level of underestimation of VD can be as much as a factor of 10 for NAT mixtures and up

Deleted: There is very little information on the size distribution or actual shapes of non-spherical NAT or ice PSC particles. Therefore, we made the simplifying assumption that useful relationships could be based on the averaged scattering properties of a range of size distributions for liquid spherical H_2SO_4 - H_2O and STS particles, the characteristics of which are much better constrained.

Deleted: ure

Deleted: 5

Deleted: 6

Deleted: -

Deleted: 7

Deleted: 8

Deleted: s

Deleted: 5

Deleted: 6

to a factor of 30 for ice PSCs. To test the validity of our approach, we used bimodal lognormal size distribution fits to in situ optical particle counter measurements within STS, NAT, and ice PSC layers (Deshler et al., 2003) to compute SAD, VD, and $\beta_{\text{particulate}}$. These are the blue symbols (labeled according to PSC composition) in Figs. 9 and 10 and show that our estimates of SAD and VD are reasonable.

3.6 Illustration of Difference Between v1 and v2 Algorithms

In this section, we illustrate top-level changes in CALIOP PSC data products between the v1 and v2 algorithms. Figures 11(a) and 11(b) present curtains of the retrieved v2 values of the two optical signals used in PSC detection and composition discrimination, R_{532} and β_{\perp} , for the orbit shown in Fig. 2, and Fig. 11(c) is the resultant v2 PSC composition curtain. Spatially-coherent regions of NAT mixtures/enhanced NAT mixtures (yellow/red) and ice (blue) identified along the orbit track correspond directly to regions of enhancements in both R_{532} and β_{\perp} , while regions of liquid STS (green) show no enhancements in β_{\perp} since they are spherical droplets and are identified solely through enhancements in R_{532} (i.e. near left edge of orbit curtain). Also notice the mountain wave ice (dark blue) with its distinctive tilted layer structure over the Antarctic Peninsula (75°S, 300°W). For comparison, the v1 PSC composition curtain is shown in Fig. 11(d). In general, there is much more ice and much less enhanced NAT mixtures in v2 compared with v1, where much of the ice was misclassified as NAT mixtures due to the fixed boundary separating the two composition classes in v1. In the lower stratosphere/upper troposphere, the v2 composition classification is producing more ice than with v1 due to the improved characterization of the HNO_3 and H_2O condensables in this region. In addition, v2 substantially fills in holes that are present in the v1 image and reduces the pixel-to-pixel variation in inferred PSC composition. As noted in Section 3.3, all clouds at altitudes below the 215 hPa pressure level are assumed to be ice in v2.

Figure 12 compares v1 and v2 in terms of the total number of CALIOP measurement samples within PSCs (180-m vertical by 5-km horizontal pixels) for the Antarctic in 2009 at altitudes 4 km or more above the tropopause (to avoid contamination from cirrus), as well as the breakdown of those observations by PSC composition. There are about 19% more total PSC measurements with v2 due to the less conservative PSC detection thresholds. In terms of PSC composition, the STS, NAT mixture, and wave ice fractions are similar in v1 and v2, but there is a significant decrease in v2 relative to v1 in enhanced NAT mixtures (5.8% versus 18.8%) and an accompanying increase in ice PSCs (21.4% versus 10.6%). We estimate that about 75% of the additional v2 ice PSCs come from a reclassification of v1 Mix2-enhanced PSCs, and the remaining 25% from a reclassification of v1 Mix1 and Mix2 PSCs. Differences between v1 and v2 Antarctic PSC composition for other years and groups of years are comparable to those shown in Fig. 12.

3.7 Consistency of v2 PSC Observations with Expected Thermodynamic Regimes

Similar to the approach used by Lambert et al. (2012), P13, and Lambert and Santee (2018), we have examined the consistency of the v2 PSC composition classes with respect to their expected thermodynamic existence regimes through

Deleted: 9

Deleted: 9

Deleted: 9

Deleted: 10

Deleted: observations

Deleted: observations

Deleted: fractions of

Deleted: observations

Deleted: increase

Deleted: and a concomitant decrease in enhanced NAT mixtures (8.3% versus 18.8%). This is a result of v2 having a dynamic RNAT/ice boundary, as well as a more restrictive definition of enhanced NAT mixtures, i.e. only those NAT mixtures with $\beta_{\perp} > 2 \times 10^{-5} \text{ km}^{-1} \text{sr}^{-1}$ and $R_{532} > 2$.

Deleted: ¶

combined analyses of the CALIOP and Aura MLS data. Here, we extend these previous studies to now include the entire 2006-2017 v2 CALIOP data record. To avoid potentially biased MLS HNO_3 measurements where the relatively large geometric field-of-view (FOV) is only partially filled with PSCs (e.g. see P13 and Lambert and Santee, 2018), the analyses are limited to cases where CALIOP PSCs cover at least 75% of the Aura MLS FOV (assumed to be 165 km x 2.16 km) and a single CALIOP composition is dominant. Composite histograms of PSC occurrence vs. $T - T_{\text{ice}}$ over the 20-22 km altitude range are shown in Fig. 13(a) and Fig. 13(c) for the Arctic (2006-07 to 2016-17) and Antarctic (2006-2017), respectively. Here, T is the ambient temperature at the CALIOP observation point determined from the MERRA-2 gridded analyses, and T_{ice} is calculated using the Murphy and Koop (2005) relationship with the coincident Aura MLS gas-phase H_2O abundance. Histograms are shown for the CALIOP STS, NAT mixture (including enhanced NAT mixtures), and ice (including wave ice) composition classes, and each histogram is normalized to a maximum value of 1.0. Figures 13(b) and 13(d) show the same composite histograms transformed to $T - T_{\text{eq}}$ space, where T_{eq} is defined as T_{NAT} , T_{STS} , or T_{ice} , depending on the CALIOP composition classification, and is calculated using the Hanson and Mauersberger (1988) (T_{NAT}), Carslaw et al. (1995) (T_{STS}), and Murphy and Koop (2005) (T_{ice}) relationships with the coincident HNO_3 and H_2O abundances observed by MLS. T_{eq} for ice PSCs remains the same as in Figs. 13(a) and 13(c) and the ice PSC distributions are identical to those in Figs. 13(a) and 13(c). The STS and NAT mixture histograms are restricted to observations with MLS HNO_3 values greater than 1 ppbv to avoid the region where the NAT and STS equilibrium HNO_3 uptake curves converge (e.g. see Fig. 3 in P13).

The mode of the ice PSC distribution for both hemispheres is located at a temperature slightly below the frost point with a full-width-half-maximum of about 1 K. The longer positive tail in the ice PSC distributions may be associated with wave ice events induced by small-scale temperature perturbations that aren't fully resolved in the MERRA-2 temperature fields (e.g., Hoffman et al., 2017a) or NAT mixtures at warmer temperatures misclassified as ice due to measurement noise. STS PSCs in both hemispheres occur over a relative narrow temperature range centered slightly below the STS equilibrium temperature. The relatively narrow widths of the ice and STS histograms with modes near T_{eq} are an indication that these particles are near equilibrium, as would be expected. The ice and STS histogram mode peaks occurring below T_{eq} are consistent with a small cold bias in the MERRA-2 temperature analyses as noted by Lambert et al. (2012) and Lambert and Santee (2018). The NAT mixture distributions are broader and roughly bimodal with one mode slightly below the NAT equilibrium temperature and a second more populous mode at 3-4 K below NAT equilibrium, which corresponds approximately to the STS equilibrium temperature. As discussed in P13, this bimodality is likely a consequence of different exposure times of air parcels to temperatures below T_{NAT} . The mode near the STS equilibrium temperature represents air parcels with relatively brief exposure to temperatures below T_{NAT} . These parcels contain non-equilibrium liquid-NAT mixtures with a detectable enhancement in β_1 , but the uptake of HNO_3 is dominated by the much more numerous liquid droplets at the lower temperatures. The NAT mixture mode near the NAT equilibrium temperature corresponds to parcels that have been exposed to temperatures below T_{NAT} for extended periods of time, allowing a larger fraction of the gas-phase HNO_3 to condense onto the thermodynamically-favored NAT particles and bringing the mixture closer to NAT equilibrium.

Deleted: 11

Deleted: 11(

Deleted: 11

Deleted: 11

Deleted: MLS

Deleted: 11

Deleted: 11

Deleted: 11

Deleted: 11

Deleted: is due to warm biased

Deleted: associated with wave ice events

These composite histograms, which incorporate over 11 years of CALIOP PSC measurements, demonstrate behavior consistent with theoretical expectations for each composition class, providing confidence that the v2 composition classification scheme is robust.

Deleted: representing millions of PSC observations

4 PSC Climatologies

Applying the v2 detection and composition classification algorithm to the CALIOP V4.10 Lidar Level 1B data from June 2006 through October 2017, we have created a new PSC reference data record which covers 12 Antarctic PSC seasons (May-October) and 11 Arctic PSC seasons (December-March). It is archived as the CALIPSO Lidar Level 2 Polar Stratospheric Cloud Mask Version 2.0 (v2) data product and publicly available through the NASA Langley Atmospheric Science Data Center (ASDC) (https://eosweb.larc.nasa.gov/project/calipso/lidar_l2_polar_stratospheric_cloud_table). In this section, we present representative figures drawn from this data record that depict the seasonal and interannual variability of PSC spatial coverage in the Antarctic and Arctic, climatological mean geographic patterns of PSC occurrence, and overall differences between the hemispheres. We also show how Antarctic PSC composition varies climatologically over the season and relate climatological zonal mean cross-sections of PSC occurrence to analogous cross-sections of temperature and the PSC condensables HNO_3 and H_2O . We reiterate that in general we make no explicit attempt to separate upper tropospheric cirrus from PSCs in the climatologies, but do include the location of the MERRA-2 tropopause in many of the figures as a guide to the reader for the approximate upper extent of cirrus. Only in the PSC spatial volume analyses (Figs. 16 and 23) and composition pie charts (Figs. 12 and 26) do we exclude data within 4 km of the tropopause because inclusion of the omnipresent cirrus would skew the statistics on the temporal evolution of PSC occurrence and relative fraction of ice PSCs.

4.1 Antarctic

4.1.1 PSC Areal and Spatial Volume Coverage

A depiction of the vortex-wide, seasonal evolution of PSC occurrence is given by a measure of the total areal coverage of PSCs over the polar region as a function of altitude and time. To mitigate the effects of irregular sampling density due to the CALIPSO orbit geometry, the daily total PSC areal coverage is estimated as the sum of the occurrence frequency (number of PSC detections divided by the total number of observations) in ten equal-area latitude bands spanning the 50° - 90° S latitude range, multiplied by the area of each band. This estimate implicitly assumes that the CALIOP observations from the approximately 15 orbits per day are representative of the PSC coverage within each latitude band. Note that the highest equal-area latitude band covers 77.8° - 90° S, so CALIOP measurements between 77.8° - 82° S are assumed to be representative of the entire 77.8° - 90° S latitude band. A similar approach has been used to estimate PSC area statistics by P09 for CALIOP observations from 2006-2008 and also by Spang et al. (2018), who found that MIPAS and CALIOP PSC areas from the 2009 Antarctic PSC season were in excellent agreement in spite of the fundamentally different measurement approaches.

The seasonal evolution of PSC areal coverage during each of the 12 seasons in the CALIOP Antarctic data record is shown in Fig. 14. The full altitude range of the PSC data product (8.4 – 30.0 km) is presented with no attempt here to distinguish PSCs from upper tropospheric cirrus clouds that are commonly observed below ~12 km throughout the entire season. Temperatures low enough for PSC existence typically occur inside the stratospheric polar vortex, which in the case of the Antarctic is large, relatively axisymmetric, and generally similar from year-to-year (e.g. Waugh and Randel, 1999). Hence, it is not surprising that the seasonal evolution of PSC coverage in the Antarctic follows a similar pattern from year-to-year, with PSCs first occurring in mid to late May and persisting into October. The total areal extent of PSCs typically peaks in July and August when the vortex is largest and coldest and then diminishes markedly in September and approaches zero in October. PSCs extend in altitude from near the tropopause up to > 25 km, but there is a downward trend in the altitude of maximum areal coverage over time from above 20 km early in the season to near 15 km by September. This corresponds to a downward shift in the axis of coldest temperatures as the vortex warms at higher altitudes, as was also noted by Poole and Pitts (1994). An interesting feature seen in most years is the apparent merging of the upper tropospheric and lower stratospheric cloud layers in July and August associated with CALIOP observations of deep synoptic-scale clouds extending from the troposphere into the stratosphere to altitudes well above 20 km. These episodic events are likely produced by large-scale adiabatic cooling along upwardly displaced isentropic surfaces above upper tropospheric anticyclones (e.g. Teitelbaum and Sadourny, 1998; Teitelbaum et al., 2001; Kohma and Sato, 2013). Distinctive tilted cloud layers formed in the cold phases of strong orographic gravity waves (e.g. Cariolle et al., 1989; Höpfner et al., 2006; Orr et al., 2015) are also occasionally observed to extend from the troposphere well into the stratosphere, primarily over the Antarctic Peninsula. Both of these phenomena can be seen in the CALIOP orbit curtain shown in Fig. 2.

Although the general seasonal evolution is similar from year to year, there is a moderate amount of year-to-year variability in PSC coverage during the season that is primarily driven by the dynamical processes that control the size, thermal structure, and stability of the vortex, as well as the strength and frequency of orographic and upper tropospheric forcing events. For instance, 2006 was characterized by an especially large and cold vortex (e.g. WMO, 2007) and showed the largest PSC areas observed by CALIOP to date, while in 2010 and 2012 the vortex was relatively warm with concomitantly much smaller PSC areas. The climatological mean seasonal evolution of Antarctic PSC areal coverage compiled for the 2006-2017 period is shown in Fig. 15. The climatological daily maximum tropopause height is indicated on Fig. 15 by the dashed white line and provides an approximate upper limit to the extent of cirrus during the season. While it is a reasonable approximation to the seasonal evolution of PSC coverage in any given year, the dynamic variability of the vortex and orographic/upper tropospheric forcing can produce significant deviations from this mean picture. To better quantify the interannual variability in PSC coverage, we calculated the 12-year mean, standard deviation, and range of daily values of PSC spatial volume (daily area coverage integrated over altitude, e.g. see P09). These PSC spatial volumes are shown in Fig. 16, with maximum and minimum values color-coded according to the year in which they occurred. To avoid contamination from the underlying cirrus, the volume calculations include only those CALIOP observations at altitudes more than 4 km above the reported

Deleted: 12

Deleted: until early

Deleted: 13

Deleted: 14

tropopause. Most of the maximum values in PSC spatial volume are from the very cold 2006 season, and many of the minimum values are from the warmer 2010/2012 seasons. At the peak of the season in July, the relative standard deviation in PSC spatial volume is about $\pm 25\%$.

The v2 CALIOP PSC data record can also be exploited to differentiate the seasonal evolution of PSC areal coverage by composition class. Figure 17 shows the 12-year mean relative spatial coverage (composition-specific area normalized by total PSC area) for (a) STS; (b) NAT mixtures, including enhanced NAT mixtures; and (c) ice, including wave ice. To provide additional perspective, Fig. 17(d) shows the 12-year mean contour plot of $T - T_{\text{NAT}}$, where again T is the ambient temperature from MERRA-2 gridded analyses and T_{NAT} is calculated using the Hanson and Mauersberger (1988) relationship with cloud-free Aura MLS gas-phase HNO_3 and H_2O abundances. To put better focus on PSCs, we limit the lower altitude in Fig. 17 to 12 km, near the climatological maximum tropopause as shown in Fig. 15. The onset of the PSC season in the Antarctic depends on the details of the evolving Antarctic polar vortex such as its shape, location, and coldness, which vary significantly from year-to-year. Lambert et al. (2016) showed that from 2006-2015, synoptic-scale HNO_3 uptake by PSCs was first observed by Aura MLS as early as May 13 and as late as May 28. Furthermore, these initial PSCs are often “sub-visible” and only become detectable by CALIOP some 1-6 days later. Thus we chose to avoid the highly variable onset period in terms of presenting a representative climatology and restricted our analyses to days and altitudes where PSCs were observed in at least 6 of the 12 Antarctic seasons covered by CALIOP demarcated by the thick black contour line on each of the color panels in Fig. 17. This provides an indication of the climatological temporal and altitude extent of the PSC season. For STS and NAT mixtures (Figs 17a-b), PSC onset in at least six years occurred by approximately 20 May. The onset of ice PSCs (Fig. 17c) is delayed until temperatures drop below the frost point which is typically mid-June. STS (panel a) is the most prevalent composition above 20 km until mid-June and then again at lower altitudes in September and October. The early-season predominance of STS above 20 km corresponds to the region of largest temperature departures below T_{NAT} in panel (d), which is consistent with an enhanced liquid particle growth regime. The predominance of STS late in the season may be an indication that efficient NAT nuclei have been removed through sedimentation of PSC particles during the winter. NAT mixtures (panel b) are by far the dominant composition observed below 20 km in May and early June, comprising >80 % of the total observed PSC area below 17 km, and are also the prevailing composition above 20 km during July through mid-September. The early season maximum of NAT mixtures below 17 km corresponds to a region of temperatures near or just below T_{NAT} where liquid particle growth would not be expected. The onset of ice PSCs (panel c) is delayed 3-4 weeks relative to STS and NAT mixtures, typically occurring around mid-June as temperatures fall below the frost point. The areal extent of ice PSCs is largest in July and August primarily at altitudes below 20 km, but ice is rarely the predominant composition. Note that cirrus contamination is still apparent in the ice distributions (panel c) above 12 km. The 12-year mean relative PSC composition breakdown shown in Fig. 17 is remarkably similar to the 2006-2008 compilation shown by P09, highlighting the robustness of these results.

Deleted: 15

Deleted: 15

Deleted: May 21 and beyond,

Deleted: when

Deleted: .

Deleted: 15

4.1.2 Zonal Mean and Geographical Distributions of PSC Occurrence

The PSC areal coverage and spatial volume plots capture quite well the seasonal evolution and interannual variability of PSCs from a vortex-wide point of view, but offer no information on the actual geographical patterns of occurrence. To gain this insight, we now examine monthly zonal mean cross sections and polar maps of PSC occurrence frequency.

Latitude/altitude cross sections of monthly zonal mean PSC occurrence frequency compiled from the 12-year CALIOP Antarctic data record are shown in Fig. 18 (top row) for the four primary Antarctic PSC months of June–September. To indicate potential PSC existence regimes, we show corresponding cross sections of zonal mean cloud-free MLS HNO_3 (second row) and H_2O (third row), MERRA-2 T (fourth row), and $T-T_{\text{NAT}}$ (bottom row). For reference, the mean location of the edge of the vortex from the Aura MLS DMPs and the tropopause altitude from MERRA-2 are indicated on the panels by the black dashed and dotted lines, respectively. In June, PSCs are observed at latitudes poleward of about 65°S from near the tropopause up to about 26 km in altitude, with maximum mean occurrence frequency $> 60\%$ near 18 km at the highest latitudes. PSC occurrence peaks during July and August, with the region of highest occurrence frequency expanding in both altitude and latitude in response to the continued cooling of the polar vortex. There is also a hint of a double peak in occurrence frequency with altitude during these months with the dominant peak near 15 km and a secondary peak above 20 km. PSC occurrence declines significantly in both magnitude and spatial extent in September with only a small region of occurrence frequency $> 40\%$ at 14 km near 82°S and overall occurrence restricted to altitudes below 23 km as the vortex warms at higher altitudes. As was observed in the vortex-wide PSC areal coverage plots, there is a systematic shift downward in the altitude of maximum zonal mean PSC occurrence from near 18–20 km in June to below 15 km in September. Upper tropospheric cirrus cloud occurrence frequency is $> 10\text{--}15\%$ throughout the season at all latitudes.

Although these conventional latitude/altitude zonal means are correct in a statistical sense, the Eulerian view has the disadvantage of possibly averaging together air masses from different, physically distinct regions of the vortex or even from inside and outside of the vortex. Consequently, the latitude/altitude zonal means are difficult to interpret in the context of meteorological and microphysical processes within the vortex that control PSC occurrence. This is especially true when the vortex is elongated and/or not centered over the South Pole. An alternative approach is to average data in the more physically based quasi-Lagrangian coordinate system of equivalent latitude (EqLat) versus potential temperature (θ). This coordinate system roughly captures the motion of air parcel ensembles and is widely used by the stratospheric chemistry and dynamics community in studies of polar processes (e.g., Butchart and Remsberg, 1986; Manney et al., 1999).

Figure 19 shows the EqLat/ θ cross-sectional representations of the 12-year average, monthly zonal mean Antarctic PSC occurrence frequency, cloud-free MLS HNO_3 and H_2O , MERRA-2 T , and $T-T_{\text{NAT}}$. During most months, the center of the polar vortex is shifted off the pole so that the conventional latitude/altitude cross-sectional monthly means (Fig. 18) blur the sharp gradients in HNO_3 and H_2O between the interior and “collar” regions (e.g. Wespes et al., 2009) of the vortex that are much more clearly captured in the EqLat/ θ cross-sections (Fig. 19). Gas-phase HNO_3 and H_2O are severely depleted by July

Deleted: 16

Deleted: 17

Deleted: 16

Deleted: 17

in the interior of the vortex at EqLat $< -75^\circ$ and $\theta = 400$ -500 K. Although there is relatively cold air present in this region, the lack of condensables sufficiently lowers the particle thermodynamic existence temperatures (e.g. T_{NAT}) to near or below ambient temperatures, limiting PSC existence. Consequently, the highest PSC frequency more typically occurs at equivalent latitudes closer to the vortex edge where there is an optimal combination of sufficient condensables and cold temperatures, which corresponds reasonably well with the minima in the T - T_{NAT} distributions (bottom row of Fig. 19). The reason that a double-peak vertical structure in PSC occurrence appears at high latitudes in July and August in the latitude/altitude cross sections (Fig. 18) is much clearer in the EqLat/ θ coordinate system, which show a relative minimum in PSC occurrence at $\theta = 450$ K (~18 km) corresponding to the layer of depleted condensables.

PSC occurrence is not typically zonally symmetric in either geographic or equivalent latitude coordinate systems, but instead exhibits distinct longitudinal patterns. To illustrate these preferred patterns of PSC occurrence, 12-year average, monthly mean polar maps of Antarctic PSC frequency at $\theta = 500$ K (~20 km altitude) are shown in Fig. 20. The top row shows the occurrence frequency for all PSCs, while the subsequent rows display the occurrence frequencies of STS, NAT mixtures, and ice, respectively. Overlaid in the figure are the mean location of the edge of the vortex (black line) and the boundaries of the regions where the mean temperature is below T_{NAT} (solid red line) and below T_{ice} (dashed black line). In general, PSC occurrence is roughly bounded by the region where mean temperature is below T_{NAT} and increases poleward with the highest occurrence frequencies (>60%) generally located within the region of $T < T_{\text{ice}}$ at the highest latitudes. The contours of PSC occurrence frequency and cold pool are not symmetric around the pole, but instead pushed slightly off the pole towards the Greenwich Meridian (GM) longitude quadrant. This zonal asymmetry in PSC occurrence is especially pronounced in July-September with the maximum occurrence frequency at 0° - 90° W longitude near the base of the Antarctic Peninsula. The enhancement in PSC occurrence at longitudes near the Antarctic Peninsula is due to frequent mountain wave activity in this region (Alexander et al., 2011; Alexander et al., 2013; Hoffman et al., 2017b) and the large-scale upper tropospheric forcing events which are more frequent at these longitudes (Kohma and Sato, 2013).

The mean geographical distributions of STS, NAT mixtures, and ice PSCs at $\theta = 500$ K (Fig. 20, rows 2-4) also exhibit preferred occurrence patterns. STS-only observations are widespread during June at this level, but more limited afterwards with occurrence frequencies generally less than 10% in the interior of the vortex during July-August and less than 5% during September. NAT mixtures, on the other hand, are relatively widespread over much of the vortex at this level, especially during July and August when occurrence frequencies exceed 35%. The ubiquitous NAT mixtures and concomitant limited STS-only observations may be an indication that air parcels well inside the vortex have been exposed to temperatures below T_{NAT} for sufficiently long periods of time to allow the condensed HNO_3 to migrate from the STS droplets to the more thermodynamically-favored NAT particles. The ring of increased occurrence of NAT mixtures in July over East Antarctica between 70° - 75° S latitude is consistent with the so-called NAT belt that evolves downstream of ice PSCs that frequently occur over the Antarctic Peninsula (e.g. Höpfner et al., 2006). Ice PSC occurrence aligns reasonably well with the region of mean temperatures below T_{ice} that occurs over the interior of the vortex at latitudes generally poleward of 70° S with a

Deleted: 16

Deleted: 16

Deleted: 18

Deleted: about

Deleted: 18

Deleted: essentially no

Deleted: STS

Deleted: deep

Deleted: completely missing

Deleted: absence of

distinct maximum in July and August near the base of the Antarctic Peninsula arising from the frequent mountain wave and upper-tropospheric forcing events in this region.

4.2 Arctic

4.2.1 PSC Areal and Spatial Volume Coverage

5 The more irregular underlying surface topography in the Northern Hemisphere leads to stronger upward-propagating wave activity than in the Southern Hemisphere, causing a weaker and more distorted Arctic vortex compared to the Antarctic (e.g. Waugh et al., 2017). As a result, the Arctic polar vortex is warmer and exhibits greater temporal variability than its Antarctic counterpart, including sudden stratospheric warmings, which can severely disrupt or even completely break down the vortex in mid-winter (Charlton and Polvani, 2007). Not surprisingly then, Arctic PSC occurrence varies significantly

10 from year to year as is illustrated in Fig. 21, which shows the daily mean PSC areal coverage during each of the 11 Arctic seasons in the CALIOP data record. As in Fig. 14, the full altitude range of the PSC data product (8.4 – 30.0 km) is presented with no attempt here to distinguish PSCs from upper tropospheric cirrus clouds. The 2010-11 season was marked by persistent periods of PSCs from December-March that set the stage for record ozone depletion over the Arctic (Manney et al., 2011b). During the 2015-16 season, CALIOP observed the largest areal coverage of PSCs over the Arctic to date, including areas of synoptic ice PSCs, which have only been observed by CALIOP in the Arctic in only one other season (2009-10). In contrast to these remarkable Arctic PSC seasons, the warm 2014-15 winter was almost devoid of PSCs. Also note the merging of the upper tropospheric and lower stratospheric cloud layers during some winters (e.g. 2015-16). As in the Antarctic, this is indicative of upper tropospheric forcing events in the Arctic (Fromm et al., 2003; Achtert et al., 2012) that produce deep synoptic-scale cloud layers extending from the troposphere into the stratosphere.

20 For comparison with the Antarctic multi-year mean (Fig. 15), the mean seasonal evolution of Arctic PSC areal coverage compiled for the 2006-2017 period is shown in Fig. 22 with the climatological maximum daily tropopause height indicated by the dashed white line. Clearly the multi-year Arctic mean is unlike any year in the CALIOP record and, hence, would not be very meaningful in itself as guidance for representing Arctic PSCs in a model. The large year-to-year variability in Arctic PSC coverage is further quantified in Fig. 23, which depicts the time series of 11-year mean daily PSC spatial volumes over the Arctic along with the standard deviations, maxima, and minima. All the maxima in January correspond to the anomalous 2015-16 season while the majority of the maxima in February and March correspond to the 2010-11 season. The year-to-year variability in the PSC spatial volume in the Arctic is much larger than in the Antarctic, with the relative standard deviations exceeding 100% for most days. In terms of the climatology of Arctic PSC composition, we feel that it meaningful to show only the composite season-long vertical profile of relative spatial coverage (composition-specific area normalized by total PSC area) in Fig. 24. STS and NAT mixtures are the major Arctic PSC compositions as expected, with STS (NAT mixtures) predominant above (below) 24 km. Note that upper tropospheric cirrus produces the ice maximum near 12 km.

30

Deleted: 19

Deleted: For instance, t

Deleted: This

Deleted: dramatic

Deleted: 20

4.2.2 Geographical Distributions of PSC Occurrence

In spite of the high interannual variability in PSC areal coverage, the geographical pattern of PSC occurrence in the Arctic is quite regular from year to year, with PSCs primarily confined to longitudes from about 60° W to 120° E as illustrated in the 11-year average, monthly mean Arctic PSC occurrence frequency maps for December and January shown in Figure 25. This region corresponds to the climatologically favored location of the Arctic vortex in recent decades (e.g. Zhang et al., 2016) which has been influenced by enhanced zonal wavenumber 1 activity, pushing the vortex off the North Pole towards Eurasia.

4.3 Differences between Antarctic and Arctic

As discussed in Sections 4.1 and 4.2, the Antarctic polar vortex is a much more conducive environment for PSC existence than its Arctic counterpart. The Antarctic PSC season is longer and more regular with PSCs present every year from mid-May to early October, while in the Arctic, PSC occurrence is possible from December-March but not guaranteed in any of these months. The contrast between CALIOP PSC observations in the two hemispheres can be seen in Figure 26, which shows the total number of measurement samples within PSCs over the entire 2006-2017 data record (12 Antarctic seasons and 11 Arctic seasons), as well as the average, minimum, and maximum percentage of measurements by composition class. On average, about 14 times more PSCs were sampled during a season in the Antarctic than in the Arctic. The largest differences in composition are in ice, which comprised nearly 25% of Antarctic PSCs compared to less than 5% in the Arctic (a result of the much colder Southern vortex) and in NAT mixtures, which comprised nearly 60% of Arctic PSCs, but only about 40% of Antarctic PSCs. The percentages of STS, enhanced NAT mixtures, and wave ice are not vastly different between the two hemispheres.

5 Particle Surface Area Density and Volume Density

As described in Section 3.5, estimates of the bulk particle microphysical quantities SAD and VD are included in the new CALIOP v2 PSC data record. The estimates assume liquid particles (binary H₂SO₄-H₂O or STS) only and thus have large uncertainties when NAT mixtures or ice are present. Our estimated SAD is likely an upper (lower) limit for the actual SAD in NAT mixture (ice) PSCs, while our estimated VD is likely a lower limit for the actual VD in ice PSCs and in most NAT mixtures. Nonetheless, they represent the first long-term, vortex-wide observational-based record of SAD and VD and can be used to compare CALIOP stratospheric data with in situ particle measurements and to test parameterizations of the chemical and radiative effects of particles in current and future theoretical models. Since the SAD and VD estimates cover the full range of CALIOP data, including “sub-visible” PSCs as well as background aerosols, they may prove especially valuable in studies of the role of PSCs relative to that of cold background aerosols in early-season chlorine activation (e.g., Wegner et al., 2016; Drdla and Müller, 2012).

The climatological, 12-year mean depiction of the temporal evolution of vortex-averaged SAD over the Antarctic is shown

Deleted: 21

Deleted: 22

Deleted: observations

Deleted: observations

Deleted: observed

in the top panel in Figure 27. The vortex-mean SAD begins to rise in mid-May, which may be an indication of binary aerosol deliquescence as the vortex cools and/or the initial onset of PSCs. SAD increases more significantly in June as PSCs become widespread below 25 km. The maximum SAD and its quasi-periodic nature are associated with ice PSCs that are most prevalent in July and August below 20 km. Twelve-year average, monthly mean polar maps of SAD at 18 km altitude are shown in the bottom row of Figure 27. Since ice PSCs produce the largest enhancements in SAD, the mean geographical distribution of SAD closely mirrors the highly zonally asymmetric pattern of ice PSC occurrence, with largest values in the 90° W to 0° longitude sector where ice PSC occurrence is most prevalent, especially in July-September. The spatial and temporal patterns in estimated VD (not shown) are very similar to those in estimated SAD, as expected.

Deleted: 23

Deleted: 23

6 Comparison with Other PSC Data Sets

In this section we discuss comparisons of CALIOP v2 PSC data with MIPAS PSC observations over the period 2002-2012 and with contemporaneous and historical ground-based lidar PSC observations from McMurdo Station, Antarctica (77.85° S, 166.67° E) and Ny-Ålesund, Spitsbergen (79° N, 12° E). Also, to investigate the possibility of longer-term trends, we compare CALIOP PSC data from 2006-2017 with the SAM II (Stratospheric Aerosol Measurement II) solar occultation PSC record from the period 1978-1989 (Poole and Pitts, 1994; Fromm et al., 2003).

PSCs are detected and classified in MIPAS data based on differences in IR limb emission spectral measurements from different atmospheric window regions (Spang et al., 2005; 2016). Since this approach is completely different from that of CALIOP, comparisons with MIPAS PSC observations provide an independent test of the validity of the CALIOP PSC results. The first such assessment was presented by Höpfner et al. (2009), who showed a high degree of correlation between MIPAS NAT and CALIOP v1 NAT mixtures for the 2006–2007 Antarctic and 2006/07–2007/08 Arctic winters. Spang et al. (2018; hereafter S18) recently published a climatology of PSC occurrence and composition classification based on MIPAS data from 2002-2012. S18 compared MIPAS and CALIOP v2 observations of daily, altitude-resolved PSC areal coverage for the 2009 Antarctic season and found excellent correspondence in the overall spatial and temporal evolution as well as for different PSC composition classes. The 10-year mean MIPAS daily PSC areal coverage shown by S18 is very similar to the 11-year mean CALIOP v2 areal coverage (Fig. 15). Additionally, S18 showed the predominant PSC composition to be STS in May and early June and NAT over most altitudes from early July through the end of the season, which is consistent with the CALIOP v2 relative composition areal coverages shown in Fig. 17. In another recent paper, Höpfner et al. (2018) compared retrieved/estimated vertical profiles of PSC particle VD from coincident (within 200 km distance and 2 h time) MIPAS and CALIOP measurements during the 2009 Antarctic winter. For STS PSCs, the comparisons showed very good agreement between the instruments in terms of the vertical profile shape as well as the absolute values of particle VD.

To facilitate comparisons with the ground-based lidar data, we calculated the frequency of CALIOP v2 PSC observations within $\pm 1.5^\circ$ latitude and $\pm 15^\circ$ longitude of McMurdo and Ny-Ålesund, respectively. Figure 28 shows CALIOP PSC occurrence frequencies near McMurdo for June-September, 2006-2010 compiled in $15\text{-d} \times 1.5\text{-km}$ bins, which is similar in nature to the ground-based McMurdo 2D PSC occurrence frequency histogram for the same time period given in Fig. 3 in Di Liberto et al. (2014). Figure 29 extends this to show CALIOP PSC occurrence frequencies near McMurdo for May-September, 2006-2017 compiled in $15\text{-d} \times 2\text{-km}$ bins. This figure is quite similar to the 2D histogram of ground-based lidar PSC occurrence frequencies at McMurdo for the earlier period 1995-2001 shown in Fig. 3b in Massoli et al. (2006). Finally, Figure 30 shows CALIOP PSC occurrence frequencies near Ny-Ålesund for December-February, 2006-2017 compiled in $7\text{-d} \times 2\text{-km}$ bins. This figure is qualitatively similar to the 2D histogram of Ny-Ålesund ground-based lidar PSC occurrence frequencies for five earlier Arctic seasons from 1995/96 and 2002/03 shown in Fig. 3a in Massoli et al. (2006). It is not surprising that the absolute sighting frequencies at Ny-Ålesund by CALIOP and the ground-based lidar do not agree well given the different time periods and the high degree of interannual variability in PSC occurrence in the Arctic (as illustrated earlier in Fig. 23).

The first spaceborne sightings of PSCs were by SAM II (McCormick et al., 1982), which was a single-channel ($1\text{-}\mu\text{m}$) sun photometer (McCormick et al., 1979) that operated on the Nimbus 7 satellite from October 1978 – December 1993 (orbit degradation led to significant data gaps after 1989). SAM II measured the solar radiance in a small (0.01°) field of view along a tangential ray path through the Earth's atmosphere during each sunrise and sunset encountered by the satellite. The radiance data were reduced to give transmittance profiles, which were then inverted by the methods of Chu and McCormick (1979) to produce 1-km vertical resolution profiles of particulate extinction ($\alpha_{\text{particulate}}$) at the $1\text{-}\mu\text{m}$ wavelength. Due to the orbital characteristics of Nimbus 7, all sunrise events occurred in the Southern Hemisphere at latitudes from 64°S to 81°S , and all sunset events occurred in the Northern Hemisphere between 65° to 84°N . The measurement locations progressed slowly in latitude ($1^\circ\text{-}2^\circ$ per week) from one extreme to the other over a period of three months with the minimum and maximum latitudes measured at the solstices and equinoxes, respectively. There were approximately 14 measurements in each hemisphere per day, each separated by about 26° longitude. The SAM II extinction values represent an average over a measurement volume near the tangent point of the optical path, which is approximately $230\text{ km long} \times 1\text{-km thick}$. Because of this long horizontal path through the atmosphere, SAM II was very sensitive to the presence of thin cloud that would be transparent to many nadir-viewing instruments. While the inversion treats the atmosphere as a series of concentric shells where the particulate matter in each shell is assumed to be homogeneously distributed throughout the shell, in reality clouds can occur at any point along the ray path at an altitude equal to or higher than the tangent point. With a 12-bit digitizer (Chu and McCormick, 1979), SAM II could not measure through clouds with optical depths greater than about 6 (maximum $\alpha_{\text{particulate}} \cong 0.02\text{ km}^{-1}$).

Deleted: For

Deleted: 8

The first step in comparing CALIOP with SAM II is to produce a subset of CALIOP data (which we shall call CALIOP-SO) matched to the nominal SAM II solar occultation sampling geometry. For each day from May-November in the Antarctic and from November-March in the Arctic, we determined the longitudes at which the CALIPSO orbits crossed the nominal SAM II measurement latitude(s). We then defined a 230 km along track \times 1 km vertical subset of CALIOP data centered at the SAM II measurement latitude to represent the large occultation sampling volume. If CALIOP detected PSCs in at least five measurement pixels (5 km horizontal \times 180-m vertical) within this volume, then the CALIOP-SO measurement was counted as a PSC. The mean CALIOP 532-nm particulate backscatter ($\beta_{\text{particulate}}$) in the occultation sampling volume was then calculated. For a given day, we produced 14-15 simulated CALIOP-SO profiles at 1-km vertical resolution from 14 – 30 km in altitude. We repeated this for each day in the CALIOP PSC data record, producing a CALIOP-SO database covering the 2006-2017 period.

For a quantitative comparison of the two data sets, we first converted the CALIOP-SO mean 532-nm $\beta_{\text{particulate}}$ values to 1- μm $\alpha_{\text{particulate}}$ values using the relationship from Gobbi et al. (1995). We then multiplied the archived SAM II 1- μm $\alpha_{\text{particulate}}$ values by a factor of 1.3 based on the assessment of Thomason et al. (2018) who noted that the SAM II data may be biased low by as much as 30%. Note that such a bias would have little effect on published SAM II PSC statistics that were based on relative increases in $\alpha_{\text{particulate}}$. We then produced PDFs as a function of altitude of calculated 1- μm $\alpha_{\text{particulate}}$ for CALIOP-SO Antarctic PSCs for 2006-2017, and of adjusted ($\times 1.3$) SAM II 1- μm $\alpha_{\text{particulate}}$ for Antarctic PSCs detected during the years 1978-1989. We restricted our analysis of the optical signals to the Antarctic because of the large degree of similarity in PSCs there from year to year, and omitted the years 1983-1986 from the SAM II composite to avoid the possible masking influence of the 1982 El Chichón eruption. From the PDFs, we determined the season-long minimum (1st percentile) detectable values of 1- μm $\alpha_{\text{particulate}}$ for SAM II ($\times 1.3$, solid curve) and CALIOP-SO (dotted curve) PSCs, which are plotted as a function of altitude in Fig. 31. These show a clear difference in sensitivity between the instruments, with SAM II able to detect more tenuous PSCs.

To put both datasets on equal footing for comparing PSC occurrence frequency, we then reprocessed the SAM II data for PSC detections, excluding all data points with adjusted 1- μm $\alpha_{\text{particulate}}$ that fell below the CALIOP-SO minimum detection threshold. For the CALIOP-SO profiles, we excluded data that would have been beyond the optical depth limit of SAM II, i.e. points with 1- μm $\alpha_{\text{particulate}} > 0.02 \text{ km}^{-1}$ as well as all points at lower altitudes in those profiles. Figure 32 shows the time series of multi-year mean Antarctic PSC column occurrence frequency for CALIOP-SO (a) and SAM II (b), along with standard errors in the means. Note that the nominal SAM II solar occultation sampling latitude tracks near the terminator, and after September there are no night-time CALIOP measurements at the SAM II sampling latitude. Overall, the magnitude and variability of the CALIOP and SAM II Antarctic PSC column occurrence frequencies are similar, suggesting there have not been any significant changes in since the SAM II era. CALIOP-SO and SAM II column PSC occurrence frequencies for the Arctic are shown in Fig. 33. The two records are similar for February, but the CALIOP-SO occurrence frequencies are

Deleted: However, note that the SAM II occurrence frequencies are higher than those of CALIOP early in the PSC season.

significantly higher than SAM II for December and February. This is likely a consequence of the high degree of interannual variability in Arctic PSCs rather than an indicator of a long-term trend.

7 Summary and Discussion

Measurements from CALIOP on the CALIPSO satellite have greatly expanded the PSC observational data record with now over 11 years of observations to date. The spaceborne lidar profiles the polar stratosphere with unprecedented spatial (5-km horizontal \times 180-m vertical) and temporal (\sim 15 orbits/day) resolution and its dual-polarization capability allows classification of PSCs according to composition. A new v2 CALIOP PSC algorithm has been developed that corrects a number of known deficiencies in previous versions, leading to significantly improved PSC composition data products. Major v2 enhancements include dynamic adjustment of composition boundaries to account for effects of denitrification and dehydration, direct use of measurement uncertainties, addition of composition confidence indices, and retrieval of particulate backscatter, which enables simplified estimates of particulate SAD and VD. Top-level comparisons between v1 and v2 data products indicate that the improved discrimination between ice and NAT mixtures leads to roughly twice as much ice identified in v2 relative to v1, coming primarily at the expense of enhanced NAT mixtures. Composite multi-season histograms of v2 PSC observations in each composition class versus $T-T_{eq}$ were shown to conform to their expected existence regimes, with narrow distributions near T_{eq} for STS and ice, which are thought to be near thermodynamic equilibrium, and a broader bimodal distribution of NAT mixtures due to the frequent non-equilibrium growth of NAT particles. These results are consistent with findings of P13 for the 2006-2009 period, underscoring the robustness of the v2 composition discrimination approach.

Utilizing the v2 algorithm, we have produced a state-of-the-art CALIOP PSC reference data record that spans the June 2006-October 2017 time period with PSC information compiled along each of the \sim 15 CALIPSO orbits per day. Nearly coincident Aura MLS measurements of HNO_3 and H_2O , the primary PSC condensables, along with vortex information from the Aura MLS DMPs have been mapped to the CALIOP PSC along-orbit grid and included in the PSC data products to facilitate their use in the analyses. In combination, this data record represents the most comprehensive, high resolution PSC database in existence and establishes the foundation for the compilation of a robust climatology of PSC occurrence and particle characteristics. The CALIPSO Lidar Level 2 Polar Stratospheric Cloud Mask Version 2.0 (v2) data product is archived at the NASA Langley Science Data Center and available publicly (https://eosweb.larc.nasa.gov/project/calipso/lidar_l2_polar_stratospheric_cloud_table).

From the 11+ year CALIOP PSC reference data record, we have compiled a comprehensive climatology of PSC occurrence and composition for both the Antarctic and Arctic. The seasonal evolution of Antarctic PSC areal coverage corresponds closely to the evolution of the stratospheric polar vortex which is generally similar from year to year in the Antarctic and hence is captured reasonably well by the multi-season mean depiction. However, year-to-year variability in vortex shape,

Deleted: 6 Comparison to SAM II Solar Occultation PSC Record¶

To investigate the possibility of longer-term trends, we have compared the CALIOP Antarctic data record with the SAM II (Stratospheric Aerosol Measurement II) solar occultation Antarctic polar stratospheric aerosol and cloud data record from the years 1979-1989 (Poole and Pitts, 1994). To account for differences caused by dissimilarities in sampling, we have produced a subset of CALIOP measurements matched to the nominal SAM II solar occultation sampling pattern where measurement latitude varied slowly over the season from 64° S at the solstices to 80° S at the equinoxes. In addition, we degraded the resolution of the CALIOP PSC products to roughly match the large sampling volume of SAM II, which was approximately 1 km in the vertical by several hundred km in the horizontal. For comparison, we calculated 11-year mean PSC occurrence frequencies (SAM II: 1979-1989, CALIOP: 2006-2016) over 10-day periods from May through October in 1-km bins over the altitude range from the tropopause + 2 km to 30 km. Then we integrated the occurrence frequencies over altitude to produce column-integrated occurrence frequencies. Figure 24 shows the multi-year mean time series for CALIOP (a) and SAM II (b), along with standard deviations and the maximum and minimum values observed in any season over the 11-year periods. Note that the solar occultation sampling latitude tracks near the terminator, and after September there are no night-time CALIOP measurements at the SAM II sampling latitude. Overall, the magnitude and variability of the CALIOP and SAM II integrated occurrence frequencies are similar, indicating that there have not been any significant changes in PSC occurrence since the SAM II era. However, note that the SAM II occurrence frequencies are higher than those of CALIOP early in the PSC season. This may be a reflection of the greater sensitivity of the limb-viewing occultation measurements to the onset of PSCs when liquid droplets first began to deliquesce and/or when low number density NAT particles form that are below the CALIOP detection thresholds. This is consistent with the findings of Lambert et al. (2016) that in a number of years there were signatures of uptake of gas-phase HNO_3 by PSC particles up to a week before PSCs were first detected by CALIOP. ¶

size and thermal structure leads to moderate variability in PSC coverage, with about 25% relative standard deviation in PSC spatial volume at the peak of the season in July and August. The relative breakdown of areal coverage by composition shows that STS is the predominant particle composition early in the season above 20 km where temperatures are optimal for liquid particle growth and again late in the season when efficient NAT nuclei may have been depleted. NAT mixtures are predominant in the slightly warmer ($T \cong T_{\text{NAT}}$) environment below 16 km in late May and June, and also above 17 km from July through mid-September when air parcels have long exposures to $T < T_{\text{NAT}}$, especially in the interior of the vortex, leading to the thermodynamically-favored NAT at the expense of STS. Monthly zonal mean cross sections show the multi-season average patterns of PSC occurrence in geographic latitude/altitude and also equivalent latitude/potential temperature coordinates. The vortex-centered EqLat/ θ coordinates better capture processes controlling PSC existence such as gradients in condensable abundances that are more closely aligned with the structure of the vortex. PSC occurrence is limited deep within the interior of the vortex at high equivalent latitudes due to severe denitrification and dehydration. The maximum in PSC occurrence frequency is typically at EqLats between 65°-75° S, closer to the collar region of higher HNO_3 near the edge of the vortex.

Geographical patterns of Antarctic PSC occurrence were investigated through examination of polar (latitude-longitude) maps of multi-season, monthly mean PSC occurrence on constant potential temperature surfaces. Overall, there is a maximum in Antarctic PSC occurrence between 90° W and 0° longitude, consistent with the preferential region for forcing by mountain waves and upper-tropospheric anticyclones. CALIOP observations of deep cloud systems that extend from the troposphere well into the stratosphere up to 20-25 km are indicative of the important role of large-scale upper tropospheric forcing in PSC formation. The particle characteristics within these deep cloud systems, particularly in the transition region near the tropopause are not well understood and warrant further investigation.

Specific compositions also exhibit preferred geographical patterns of occurrence. STS occurrence is typically limited in the interior of the vortex, while NAT mixtures are abundant throughout the vortex. The ubiquitous NAT mixtures and concomitant absence of STS-only observations is likely an indication that air parcels well inside the vortex have been exposed to temperatures below T_{NAT} for sufficiently long periods of time to allow the condensed HNO_3 to migrate from STS droplets to the more thermodynamically-favored NAT particles. A NAT mixture belt is also seen in the multi-year means over East Antarctica, consistent with MIPAS observations (Höpfner et al., 2006). The mean pattern of ice PSC occurrence is dominated by mountain wave forcing, with a maximum in the 90° W to 0° longitude quadrant near the Antarctic Peninsula.

In contrast to the Antarctic, Arctic PSC occurrence is highly variable from year-to-year due to the more disturbed Arctic vortex that is prone to sudden stratospheric warmings. As such, the evolution of an Arctic PSC season doesn't follow a climatological mean pattern and instead each PSC season is distinctly different. For instance, PSC areas during the 2010-11 and 2015-16 Arctic seasons were the highest observed during the CALIOP lifetime to date, while the 2014-15 season was almost devoid of PSCs. As a result, the relative standard deviation in Arctic PSC spatial volume is greater than 100%

throughout most of the season. In spite of the high variability in Arctic PSC occurrence, when PSCs occur they are typically found between 60° W and 90° E longitude, consistent with the preferential location of the Arctic vortex during the last decade. The larger, colder, and more stable Antarctic vortex is much more conducive for PSC formation than the Arctic vortex, leading to about a factor of 14 more PSC observations on average in the Antarctic than Arctic during the CALIOP era. The most compelling difference between the hemispheres in observed composition is in ice, which comprises 24% of PSC observations in the Antarctic on average, but only 4% in the Arctic due to the inherently warmer conditions.

Estimates of the bulk particle microphysical quantities SAD and VD are included in the new CALIOP v2 PSC data record. The estimates assume liquid particles (binary H₂SO₄-H₂O or STS) only and thus have large uncertainties when NAT mixtures or ice are present. Our estimated SAD is likely an upper (lower) limit for the actual SAD in NAT mixture (ice) PSCs, while our estimated VD is likely a lower limit for the actual VD in ice PSCs and in most NAT mixtures. Nonetheless, they represent the first long-term, vortex-wide observational-based record of SAD and VD and can be used to compare CALIOP stratospheric data with in situ particle measurements and to test parameterizations of the chemical and radiative effects of particles in current and future theoretical models. A climatology of the seasonal evolution of vortex-averaged SAD was presented, showing an initial increase in May associated with particle growth as the vortex cools, possibly from deliquescence of binary aerosol, and then a more substantial increase as PSCs become widespread in June. Maximum SAD occurs in July and August below 20 km when ice PSCs are most prevalent. Multi-season average, monthly mean polar maps of SAD exhibit a zonally asymmetric pattern that mimics ice PSC occurrence, with maxima occurring near the mountainous Antarctic Peninsula where orography leads to enhanced ice cloud formation.

Comparisons of CALIOP v2 and MIPAS data showed excellent agreement in the overall spatial and temporal evolution of Antarctic PSCs as well as that for different PSC composition classes. CALIOP v2 PSC occurrence frequency patterns in the vicinity of ground-based lidars at McMurdo Station, Antarctica, and Ny-Ålesund, Spitsbergen, are similar in nature to the climatological patterns derived from the ground-based measurements. Finally, to investigate potential longer term trends in PSC occurrence, appropriately subsampled and averaged CALIOP v2 PSC observations from 2006-2017 were compared with PSC data from the 1979-1989 period collected by the spaceborne solar occultation instrument SAM II (Stratospheric Aerosol Measurement II). The two instruments showed similar magnitude and variability in Antarctic PSC column occurrence frequency, suggesting that there has been no long-term trend. For the Arctic, the two instruments showed similar results for February, but CALIOP column occurrence frequencies were substantially higher than SAM II for December and January. This finding is likely a reflection of the high degree of interannual variability in Arctic PSCs rather than an indicator of a long-term trend.

8. Data availability

CALIPSO/CALIOP L1B: Winker, D. (2016), CALIPSO LID L1 Standard HDF File - Version 4.10, NASA Langley Research Center Atmospheric Science Data Center DAAC, Last access December 2017, https://doi.org/10.5067/caliop/calipso/lid_l1-standard-v4-10.

CALIPSO/CALIOP L2 PSC Mask: CALIPSO Science Team (2015), CALIPSO/CALIOP Level 2, Polar Stratospheric Cloud Data, version 1.00, Hampton, VA, USA: NASA Atmospheric Science Data Center (ASDC), Last access October 2017, https://doi.org/10.5067/CALIOP/CALIPSO/CAL_LID_L2_PSCMask-Prov-V1-00_L2-001.00.

Aura MLS HNO₃ data: EOS MLS Science Team (2017), MLS/Aura Near-Real-Time L2 Nitric Acid (HNO₃) Mixing Ratio V004, Greenbelt, MD, USA, Goddard Earth Sciences Data and Information Services Center (GES DISC), Last access October 2017, https://disc.gsfc.nasa.gov/datacollection/ML2HNO3_NRT_004.html.

Aura MLS H₂O data: EOS MLS Science Team (2017);, MLS/Aura Near-Real-Time L2 Water Vapor (H₂O) Mixing Ratio V004, Greenbelt, MD, USA, Goddard Earth Sciences Data and Information Services Center (GES DISC), Last access October 2017, https://disc.gsfc.nasa.gov/datacollection/ML2H2O_NRT_004.html.

Aura MLS Derived Meteorological Products: Manney et al. (2007); Manney et al. (2011a), Last access December 2017 at <https://mls.jpl.nasa.gov/dmp/>.

SAM II Aerosol Extinction data: SAM II Science Team (1999), SAM II Level 2 Data, Hampton, VA, USA: NASA Atmospheric Science Data Center (ASDC), Last access October 2017 at doi: [10.5067/NIMBUS7/SAMII/SOLAR_ASCII_L2-AV](https://doi.org/10.5067/NIMBUS7/SAMII/SOLAR_ASCII_L2-AV)

Appendix A

A.1 Crosstalk Correction

The CALIOP backscatter signal is separated into parallel (\parallel) and perpendicular (\perp) components by a polarization beam splitter in the receiver subsystem (Hunt et al., 2009). With an ideal beam splitter, the measured molecular depolarization ratio ($\delta_{\text{mol, meas}}$) would equal the theoretical value of 0.00366 at the ~40-pm bandwidth of the etalon in the CALIOP receiver (Cairo et al. 1999; Hostetler et al., 2006). The difference between the measured and theoretical molecular depolarization ratios indicates the level of crosstalk (CT) between the two polarization channels. We assume for simplicity that a fraction CT of the received parallel signal is reflected into the perpendicular channel and that the remainder ($1-CT$) of the received

Deleted: Finally, to investigate potential long-term (multi-decade) trends in PSC occurrence we compared the CALIOP Antarctic PSC data record with the historic SAM II solar occultation data record (1979-1989) that was the basis for the first satellite-based PSC climatology. To facilitate the comparison, the CALIOP data record was subsetted to mimic the sampling pattern and coarser resolution of SAM II, which made 15 observations per day at a latitude that varied slowly with season. We found that time series of SAM II occultation-like CALIOP column integrated Antarctic PSC sighting frequencies were quite similar, suggesting no obvious long-term trend in PSC occurrence.¶

parallel signal is transmitted into the parallel detector. With this assumption and some algebraic manipulation, it can be shown that

$$CT = (\delta_{\text{mol, meas}} - 0.00366) / (1 + \delta_{\text{mol, meas}}) \quad (\text{A.1})$$

The crosstalk-corrected attenuated backscatter signals can then be derived from the measured signals as follows:

$$\beta'_{\parallel} = \beta'_{\parallel, \text{meas}} / (1 - CT) \quad (\text{A.2})$$

$$\beta'_{\perp} = \beta'_{\perp, \text{meas}} - \beta'_{\parallel}(CT) \quad (\text{A.3})$$

Figure A1 shows a time series of CT calculated from daily values of $\delta_{\text{mol, meas}}$ over the course of the CALIPSO mission, as well as the PSC season averages used for simplicity in our algorithm. The abrupt jumps in CT are all associated with events in which the etalon temperature was changed, suggesting that they are real changes due to hysteresis associated with temperature cycling of the etalon and its mount. CT has been less than 0.5% over the entire mission except for the 2008 Antarctic and 2008-09 Arctic winters, when it was 0.6% – 0.65%. δ_{mol} has not been measured regularly since March 2015, so a constant value of CT has been assumed after that point.

A.2 Random Measurement Uncertainties

Random uncertainties in β'_{\parallel} [$u(\beta'_{\parallel})$] and β'_{\perp} [$u(\beta'_{\perp})$] due to shot noise are computed using the noise scale factor (NSF) approach introduced by Liu et al. (2006) and described in detail for the CALIOP system by Hostetler et al. (2006). The uncertainties are scaled by the inverse square root of the product of: the number of 15-m vertical bins being averaged, which is 12 in the case of our fixed 180-m vertical resolution, and the number of 1/3-km horizontal resolution laser shots being averaged, which ranges from 15 to 405 in our successive horizontal averaging scheme. Relative random uncertainty in attenuated scattering ratio R'_{532} [$u(R'_{532})/R'_{532}$] is calculated as the square root of the sum of squares of the relative random uncertainties in β'_{\parallel} [$u(\beta'_{\parallel})/\beta'_{\parallel}$] and β'_{\perp} [$u(\beta'_{\perp})/\beta'_{\perp}$] plus an assumed 3% relative uncertainty in β_{mol} (Hostetler et al., 2006). The basic random uncertainties are propagated through the calculation of other optical quantities to estimate their uncertainties as well.

Competing Interests

The authors declare that they have no conflict of interest.

Acknowledgements

The authors would like to thank David Considine, Program Scientist for the CALIPSO/CloudSat Missions for continued support of this research. The authors also acknowledge the Stratosphere-troposphere Processes And their Role in Climate

(SPARC) project and the International Space Science Institute (ISSI) for its support of the SPARC Polar Stratospheric Cloud Initiative (PSCi). Support for L. Poole is provided under NASA contract NNL16AA05C. MCP and LRP would like to pay special tribute to our late colleague William H. (Bill) Hunt, a senior lidar engineer who made many significant contributions to the success of atmospheric lidar programs at NASA Langley over his 40-year career. A testament to his thoroughness and dedication is the fact that CALIOP has exceeded its expected lifetime many times over.

References

- Achtert, P., Andersson, M. K., Khosrawi, F., and Gumbel, J., On the linkage between tropospheric and Polar Stratospheric clouds in the Arctic as observed by space-borne lidar, *Atmos. Chem. Phys.*, **12**, 3791-3798, doi:10.5194/acp-12-3791-2012, 2012.
- 10 Achtert, P., and Tesche, M., Assessing lidar-based classification schemes for polar stratospheric clouds based on 16 years of measurements at Esrange, Sweden, *J. Geophys. Res.*, **119**, 1386-1405, doi:10.1002/2013JD020355, 2014.
- Alexander, S. P., Klekociuk, A. R., Pitts, M. C., McDonald, A. J., and Arevalo-Torres, A. The effect of orographic gravity waves on Antarctic polar stratospheric cloud occurrence and composition, *J. Geophys. Res. Atmos.*, **116**, D06109, doi:10.1029/2010JD015184, 2011.
- 15 Alexander, S. P., Klekociuk, A. R., McDonald, A. J., and Pitts, M. C., Quantifying the role of orographic gravity waves on polar stratospheric cloud occurrence in the Antarctic and the Arctic, *J. Geophys. Res. Atmos.*, **118**, 11,493–11,507, doi:10.1002/2013JD020122, 2013.
- Bosilovich, M. G., R. Lucchesi, and M. Suarez, MERRA-2: File Specification. GMAO Office Note No. 9 (Version 1.1), 73 pp, available from http://gmao.gsfc.nasa.gov/pubs/office_notes, 2016.
- 20 Butchart, N. and Remsberg, E., The area of the stratospheric polar vortex as a diagnostic for tracer transport on an isentropic surface, *J. Atmos. Sci.*, **43**, 1319-1339, [https://doi.org/10.1175/1520-0469\(1986\)043<1319:TAOTSP>2.0.CO;2](https://doi.org/10.1175/1520-0469(1986)043<1319:TAOTSP>2.0.CO;2), 1986.
- Cairo, F., Di Donfrancesco, G., Adriani, A., Pulvirenti, L., and Fierli, F., Comparison of various linear depolarization parameters measured by lidar, *Appl. Opt.*, **38**, 4425 – 4432, doi:10.1364/AO.38.004425, 1999.
- Campbell, P., and Deshler, T., Condensation nuclei measurements in the midlatitude (1982–2012) and Antarctic (1986–2010) stratosphere between 20 and 35 km, *J. Geophys. Res. Atmos.*, **119**, 137–152, doi:10.1002/2013JD019710, 2014.
- 25 Cariolle, D., Muller, S., Cayla, F., and McCormick, M. P., Mountain waves, polar stratospheric clouds, and the ozone depletion over Antarctica, *J. Geophys. Res.*, **94**, 11233-11240, doi:10.1029/JD094iD09p11233, 1989.
- Carlsaw, K. S., Luo, B. P., and Peter, T.: An analytic expression for the composition of aqueous HNO₃-H₂SO₄ stratospheric aerosols including gas phase removal of HNO₃, *Geophys. Res. Lett.*, **22**, 1877–1880, doi:10.1029/95GL01668, 1995.
- 30 Carlsaw, K. S., Wirth, M., Tsias, A., Luo, B. P., Dörnbrack, A., Leutbecher, M., Volkert, H., Renger, W., Bacmeister, J. T., and Peter, T., Particle microphysics and chemistry in remotely observed mountain polar stratospheric clouds, *J. Geophys. Res.*, **103**(D5), 5785–5796, 1998.

- Charlton, A. J., Polvani, L. M., A new look at stratospheric sudden warmings. Part I: Climatology and modeling benchmarks, *J. Clim.*, 20, 449-469, <https://doi.org/10.1175/JCLI3996.1>, 2007.
- [Chu, W. P., and McCormick, M. P., Inversion of stratospheric aerosol and gaseous constituents from spacecraft solar extinction data in the 0.38-1.0 \$\mu\text{m}\$ range, *Appl. Opt.*, 18, 1404-1413, 1979.](#)
- 5 Crutzen, P. J., Müller, R., Brühl, C., and Peter, T.: On the potential importance of the gas phase reaction $\text{CH}_3\text{O}_2 + \text{ClO} \rightarrow \text{ClOO} + \text{CH}_3\text{O}$ and the heterogeneous reaction $\text{HOCl} + \text{HCl} \rightarrow \text{H}_2\text{O} + \text{Cl}_2$ in “ozone hole” chemistry, *Geophys. Res. Lett.*, 19, 1113–1116, doi:10.1029/92GL01172, 1992.
- [Deshler, T., Larsen, N., Weissner, C., Schreiner, J., Mauersberger, K., Cairo, F., Adriani A., Di Donfrancesco, G., Ovarlez, J., Ovarlez, H., Blum, U., Fricke, F., and Dörnbrack, A., Large nitric acid particles at the top of an Arctic stratospheric cloud, *J. Geophys. Res.*, 108\(D16\), 4517, doi:10.1029/2003JD003479, 2003.](#)
- 10 [Di Liberto, L., Cairo, F., Fierli, F., Di Donfrancesco, G., Viterbini, M., Deshler, T., and Snels, M., Observation of polar stratospheric clouds over McMurdo \(77.85°S, 166.67°E\) \(2006–2010\), *J. Geophys. Res. Atmos.*, 119, 5528–5541, doi:10.1002/2013JD019892, 2014.](#)
- Drdla, K. and Müller, R.: Temperature thresholds for chlorine activation and ozone loss in the polar stratosphere, *Ann. Geophys.*, 30, 1055–1073, doi:10.5194/angeo-30-1055-2012, 2012.
- 15 Engel, I., Luo, B. P., Pitts, M. C., Poole, L. R., Hoyle, C. R., Groß, J.-U., Dörnbrack, A., and Peter, T., Heterogeneous formation of polar stratospheric clouds – Part 2: Nucleation of ice on synoptic scales, *Atmos. Chem. Phys.*, 13, 10769–10785, <https://doi.org/10.5194/acp-13-10769-2013>, 2013.
- [Fahey, D. W., Gao, R. S., Carslaw, K. S., Kettleborough, J., Popp, P. J., Northway, M. J., Holecek, J. C., Ciciora, S. C., McLaughlin, R. J., Baumgardner, D. G., Gandrud, B., Wennberg, P. O., Dhaniyala, S., McKinney, K., Peter, T., Salawitch, R. J., Bui, T. P., Elkins, J. W., Webster, C. R., Atlas, E. L., Jost, H., Wilson, J. C., Herman, R. L., and Kleinbohl, A., The detection of large \$\text{HNO}_3\$ -containing particles in the winter Arctic stratosphere, *Science*, 291, 1026–1031, 2001.](#)
- 20 [Fromm, M., Alfred, J., and Pitts, M., A unified, long-term, high-latitude stratospheric aerosol and cloud database using SAM II, SAGE II, and POAM II/III data: Algorithm description, database definition, and climatology, *J. Geophys. Res.*, 108\(D12\), 4366, doi:10.1029/2002JD002772, 2003.](#)
- 25 [Garnier, A., Pelon, J., Vaughan, M. A., Winker, D. M., Trepte, C. R., and Dubuisson, P., Lidar multiple scattering factors inferred from CALIPSO lidar and IIR retrievals of semi-transparent cirrus cloud optical depths over oceans, *Atmos. Meas. Tech.*, 8, 2759–2774, doi:10.5194/amt-8-2759-2015, 2015.](#)
- 30 [Gelaro, R., McCarty, W., Suárez, M. J., Todling, R., Molod, A., Takacs, L., Zhao, B., The Modern-Era Retrospective Analysis for Research and Applications, version 2 \(MERRA-2\), *J. Clim.*, 30, 5419–5454, <https://doi.org/10.1175/JCLI-D-16-0758.1>, 2017.](#)
- [Gobbi, G. P., Lidar estimation of stratospheric aerosol properties: Surface, volume, and extinction to backscatter ratio, *J. Geophys. Res.*, 100, D6, 11,219-11,235, doi:10.1029/94JD03106, 1995.](#)

Deleted:

Deleted:

Deleted: J.

Deleted: M. A.

Deleted: D. M.

Deleted: C. R.

Deleted: P.

Deleted: ...,

Deleted: Gian Paolo

- Hanson, D. R. and Mauersberger, K.: Laboratory studies of the nitric acid trihydrate: Implications for the south polar stratosphere, *Geophys. Res. Lett.*, 15, 855–858, doi:10.1029/GL015i008p00855, 1988.
- Heintzenberg, J., Properties of the Log-Normal Particle Size Distribution, *Aerosol Science and Technology*, 21:1, 46-48, doi:10.1080/02786829408959695, 1994.
- 5 [Highwood, E. J., Hoskins, B. J., Berrisford, P., Properties of the arctic tropopause, *Q. J. Roy. Met. Soc.*, 126, 1515-1532, <https://doi.org/10.1002/qj.49712656515>, 2000.](#)
- [Hoffmann, L., Hertzog, A., Rößler, T., Stein, O., Wu, X., Intercomparison of meteorological analyses and trajectories in the Antarctic lower stratosphere with Concordiasi superpressure balloon observations, *Atmos. Chem. Phys.*, 17, 8045–8061, <https://doi.org/10.5194/acp-17-8045-2017>, 2017a.](#)
- 10 Hoffmann, L., R. Spang, A. Orr, M. J. Alexander, L. A. Holt, and O. Stein (2017), A decadal satellite record of gravity wave activity in the lower stratosphere to study polar stratospheric cloud formation, *Atmos. Chem. Phys.*, 17 (4), 2901-2920, doi:10.5194/acp-17-2901-2017b.
- Höpfner, M., Larsen, N., Spang, R., Luo, B. P., Ma, J., Svendsen, S. H., Eckermann, S. D., Knudsen, B., Massoli, P., Cairo, F., Stiller, G., v. Clarmann, T., and Fischer, H., MIPAS detects Antarctic stratospheric belt of NAT PSCs caused by mountain waves, *Atmos. Chem. Phys.*, 6, 1221– 1230, <https://doi.org/10.5194/acp-6-1221-2006>, 2006.
- 15 Höpfner, M., Pitts, M. C., Poole, L. R., Comparison between CALIPSO and MIPAS observations of polar stratospheric clouds, *J. Geophys. Res.*, 114, D00H05, doi:10.1029/2009JD012114, 2009.
- [Höpfner, M., Deshler, T., Pitts, M., Poole, L., Spang, R., Stiller, G., and von Clarmann, T., The MIPAS/Envisat climatology \(2002–2012\) of polar stratospheric cloud \(PSC\) volume density profiles, *Atmos. Meas. Tech. Disc.*, amt-2018-163, 2018.](#)
- 20 Hostetler, C. A., Liu, Z., Reagan, J., Vaughan, M., Winker, D., Osborn, M., Hunt, W. H., Powell, K. A., and Treppe, C., CALIOP Algorithm Theoretical Basis Document- Part 1: Calibration and Level 1 Data Products, PC-SCI-201, available at: http://www-calipso.larc.nasa.gov/resources/project_documentation.php, NASA Langley Research Center, Hampton, VA, 2006.
- Hunt, W. H., Winker, D. M., Vaughan, M. A., Powell, K. A., Lucker, P. L., and Weimer, C., CALIPSO Lidar Description and Performance Assessment, *J. Atmos. Oceanic Technol.*, 26, 1214–1228, doi:10.1175/2009JTECHA1223.1, 2009.
- 25 Kar, J., Vaughan, M. A., Lee, K.-P., Tackett, J. L., Avery, M. A., Garnier, A., Getzewich, B. J., Hunt, W. H., Josset, D., Liu, Z., Lucker, P. L., Magill, B., Omar, A. H., Pelon, J., Rogers, R. R., Toth, T. D., Treppe, C. R., Vernier, J.-P., Winker, D. M., and Young, S. A., CALIPSO Lidar Calibration at 532 nm: Version 4 Nighttime Algorithm, *Atmos. Meas. Tech. Discuss.*, <https://doi.org/10.5194/amt-2017-365>, 2017.
- 30 Kohma, M., and Sato, K., Simultaneous occurrence of polar stratospheric clouds and upper-tropospheric clouds caused by blocking anticyclones in the Southern Hemisphere, *Atmos. Chem. Phys.*, 13, 3849–3864, www.atmos-chem-phys.net/13/3849/2013/doi:10.5194/acp-13-3849-2013, 2013.
- Lambert, A., Read, W. G., Livesey, N. J., Santee, M. L., Manney, G. L., Froidevaux, L., Wu, D. L., Schwartz, M. J., Pumphrey, H. C., Jimenez, C., Nedoluha, G. E., Cofield, R. E., Cuddy, D. T., Daffer, W. H., Drouin, B. J., Fuller, R. A.,

Deleted: Jost

- Jarnot, R. F., Knosp, B. W., Pickett, H. M., Perun, V. S., Snyder, W. V., Stek, P. C., Thurstans, R. P., Wagner, P. A., Waters, J. W., Jucks, K. W., Toon, G. C., Stachnik, R. A., Bernath, P. F., Boone, C. D., Walker, K. A., Urban, J., Murtagh, D., Elkins, J. W., and Atlas, E., Validation of the Aura Microwave Limb Sounder middle atmosphere water vapor and nitrous oxide measurements, *J. Geophys. Res.*, 112, D24S36, doi:10.1029/2007JD008724, 2007.
- 5 Lambert, A., Santee, M. L., Wu, D. L., and Chae, J. H., A-train CALIOP and MLS observations of early winter Antarctic polar stratospheric clouds and nitric acid in 2008, *Atmos. Chem. Phys.*, 12, 2899–2931, <https://doi.org/10.5194/acp-12-2899-2012>, 2012.
- Lambert, A. , Santee, M. L., and Livesey, N. J., Interannual variations of early winter Antarctic polar stratospheric cloud formation and nitric acid observed by CALIOP and MLS, *Atmos. Chem. Phys.*, 16, 15219–15246, doi:10.5194/acp-16-15219-2016, 2016.
- 10 Lambert, A., and Santee, M., Accuracy and precision of polar lower stratospheric temperatures from reanalyses evaluated from A-Train CALIOP and MLS, COSMIC GPS RO, and the equilibrium thermodynamics of supercooled ternary solution and ice clouds, *Atmos. Chem. Phys.*, 18, 1945–1975, <https://doi.org/10.5194/acp-18-1945-2018>, 2018.
- Liu, Z., Hunt, W., Vaughan, M., Hostetler, C., McGill, M., Powell, K., Winker, D., and Hu, Y., Estimating random errors due to shot noise in backscatter lidar observations, *Appl. Opt.*, 45, 4437–4447, <https://doi.org/10.1364/AO.45.004437>, 2006.
- 15 Livesey, N. J., Snyder, W. V., Read, W. G., and Wagner, P. A., Retrieval algorithms for the EOS Microwave Limb Sounder (MLS), *IEEE 35 Trans. Geosci. Remote Sens.*, 44, 1144–1155, 2006.
- Livesey, N. J., Read, W. G., Wagner, P. A., Froidevaux, L., Lambert, A., Manney, G. L., Valle, L. F. M., Pumphrey, H. C., Santee, M. L., Schwartz, M. J., Wang, S., Fuller, R. A., Jarnot, R. F., Knosp, B. W., and Martinez, E., Version 4.2x Level 2 data quality and description document, Tech. Rep. JPL D-33509 Rev. C, Jet Propulsion Laboratory, available from <http://mls.jpl.nasa.gov>, 2017.
- 20 Lowe, D. and MacKenzie, A. R.: Polar stratospheric cloud microphysics and chemistry, *J. Atmos. Solar-Terr. Phys.*, 70, 13–40, doi:10.1016/j.jastp.2007.09.011, 2008.
- 25 Manney, G. L., Michelsen, H. A., Santee, M. L., Gunson, M. R., Irion, F. W., Roche, A. E., and Livesey, N. J., Polar vortex dynamics during spring and fall diagnosed using trace gas observations from the Atmospheric Trace Molecule Spectroscopy instrument, *J. Geophys. Res.*, 104, 18841–18866, doi:10.1029/1999JD900317, 1999.
- Manney, G. L., Daffer, W. H., Zawodny, J. M., Bernath, P. F., Hoppel, K. W., Walker, K. A., Knosp, B. W., Boone, C., Remsberg, E. E., Santee, M. L., Harvey, V. L., Pawson, S., Jackson, D. R., Deaver, L., McElroy, C. T., McLinden, C. A., Drummond, J. R., Pumphrey, H. C., Lambert, A., Schwartz, M. J., Froidevaux, L., McLeod, S., Takacs, L. L., Suarez, M. J., Trepte, C. R., Cuddy, D. C., Livesey, N. J., Harwood, R. S., and Waters, J. W., Solar occultation satellite data and derived meteorological products: Sampling issues and comparisons with Aura Microwave Limb Sounder, *J. Geophys. Res.*, 112, D24S50, doi:10.1029/2007JD008709, 2007.
- 30

- Manney, G. L., Hegglin, M. I., Daffer, W. H., Santee, M. L., Ray, E. A., Pawson, S., Schwartz, M. J., Boone, C. D., Froidevaux, L., Livesey, N. J., Read, W. G., and Walker, K. A., Jet characterization in the upper troposphere/lower stratosphere (UTLS): Applications to climatology and transport studies, *Atmos. Chem. Phys.*, 11, 6115–6137, <https://doi.org/10.5194/acp-11-6115-2011>, 2011a.
- 5 Manney, G. L., Santee, M. L., Rex, M., Livesey, N. J., Pitts, M. C., Veefkind, P., Nash, E. R., Wohltmann, I., Lehmann, R., Froidevaux, L., Poole, L. R., et al., Unprecedented Arctic ozone loss in 2011, *Nature*, 478, 469–475, doi:10.1038/nature10556, 2011b.
- [Massoli, P., Maturilli, M., and Neuber, R., Climatology of Arctic polar stratospheric clouds as measured by lidar in Ny-Ålesund, Spitsbergen \(79°N, 12°E\), *J. Geophys. Res.*, 111, D09206, doi:10.1029/2005JD005840, 2006.](#)
- 10 [McCormick, M. P., Hamill, P., Pepin, T. J., Chu, W. P., Swissler, T. J., and McMaster, L. R., Satellite studies of the stratospheric aerosol, *Bull. Amer. Meteor. Soc.*, 60, 1038–1046, 1979.](#)
- [McCormick, M. P., Steele, H. M., Hamill, P., Chu, W. P., and Swissler, T. J., Polar Stratospheric Cloud Sightings by SAM II, *J. Atmos. Sci.*, 39, 1387–1397, 1982.](#)
- Mishchenko, M. I., and Travis, L. D., Capabilities and limitations of a current FORTRAN implementation of the T-matrix method for randomly oriented, rotationally symmetric scatterers, *J. Quant. Spectrosc. Radiat. Transfer*, 60, 309–324, doi:10.1016/S0022-4073(98)00008-9, 1998.
- 15 Molleker, S., Borrmann, S., Schlager, H., Luo, B., Frey, W., Klingebiel, M., Weigel, R., Ebert, M., Mitev, V., Matthey, R., Woiwode, W., Oelhaf, H., Dörnbrack, A., Stratmann, G., Groö, J.-U., Günther, G., Vogel, B., Müller, R., Krämer, M., Meyer, J., and Cairo, F., Microphysical properties of synoptic-scale polar stratospheric clouds: in situ measurements of unexpectedly large HNO₃-containing particles in the Arctic vortex, *Atmos. Chem. Phys.*, 14(19), 10,785–10,801, doi:10.5194/acp-14-10785-2014, 2014.
- 20 Morgenstern, O., Hegglin, M. I., Rozanov, E., O'Connor, F. M., Abraham, N. L., Akiyoshi, H., Archibald, A. T., Bekki, S., Butchart, N., Chipperfield, M. P., Deushi, M., Dhomse, S. S., Garcia, R. R., Hardiman, S. C., Horowitz, L. W., Jöckel, P., Josse, B., Kinnison, D., Lin, M., Mancini, E., Manyin, M. E., Marchand, M., Marécal, V., Michou, M., Oman, L. D., Pitari, G., Plummer, D. A., Revell, L. E., Saint-Martin, D., Schofield, R., Stenke, A., Stone, K., Sudo, K., Tanaka, T. Y., Tilmes, S., Yamashita, Y., Yoshida, K., and Zeng, G.: Review of the global models used within phase 1 of the Chemistry–Climate Model Initiative (CCMI), *Geoscientific Model Development*, 15 10, 639–671, <https://doi.org/10.5194/gmd-10-639-2017>, <http://www.geosci-model-dev.net/10/639/2017/>, 2017.
- 25 Murphy, D. M. and Koop, T.: Review of the vapour pressures of ice and supercooled water for atmospheric applications, *Q. J. Roy. Meteor. Soc.*, 131, 1539–1565, doi:10.1256/qj.04.94, 2005.
- 30 [Northway, M. J., Gao, R. S., Popp, P. J., Holeccek, J. C., Fahey, D. W., Carslaw, K. S., Tolbert, M. A., Lait, L. R., Dhaniyala, S., Flagan, R. C., Wennberg, P. O., Mahoney, M. J., Herman, R. L., Toon, G. C., Bui, T. P., An analysis of large HNO₃-containing particles sampled in the Arctic stratosphere during the winter of 1999 /2000, *J. Geophys. Res.*, 107\(D20\), 8289, doi:10.1029/2001JD001079, 2002.](#)

Deleted: Nash, Eric R., Paul A. Newman, Joan E. Rosenfield, and Mark R. Schoeberl, An objective determination of the polar vortex using Ertel's potential vorticity, *J. Geophys. Res.*, 101(D 9471–9478, doi:10.1029/96JD00066, 1996.¶

Orr, A., Hosking, J. S., Homann, L., Keeble, J., Dean, S. M., Roscoe, H. K., Abraham, N. L., Vosper, S., and Braesicke, P., Inclusion of mountainwave-induced cooling for the formation of PSCs over the Antarctic Peninsula in a chemistry-climate model, *Atmos. Chem. Phys.*, 15 (2), 1071-1086, doi:10.5194/acp15-1071-2015, 2015.

Ott, L. E., Duncan, B. N., Thompson, A. M., Diskin, G., Fasnacht, Z., Langford, A. O., Lin, M., Molod, A. M., Nielsen, J. E., Pusede, S. E., Wargan, K., Weinheimer, A. J., Yoshida, Y., Frequency and impact of summertime stratospheric intrusions over Maryland during DISCOVER-AQ (2011): New evidence from NASA's GEOS-5 simulations, *J. Geophys. Res., Atmos.*, 121, 3687-3706, doi:10.1002/2015JD024052, 2016.

Peter, T. and Groö, J.-U.: Chapter 4: Polar stratospheric clouds and sulfate aerosol particles: Microphysics, denitrification and heterogeneous chemistry, in: *Stratospheric Ozone Depletion and Climate*, edited by Müller, R., pp. 108–144, RSC Publishing, 2012.

Pitts, M. C., Thomason, L. W., Poole, L. R., and Winker, D. M., Characterization of polar stratospheric clouds with spaceborne lidar: CALIPSO and the 2006 Antarctic season, *Atmos. Chem. Phys.*, 7, 5207-5228, <https://doi.org/10.5194/acp-7-5207-2007>, 2007.

Pitts, M. C., Poole, L. R., and Thomason, L. W., CALIPSO polar stratospheric cloud observations: second-generation detection algorithm and composition discrimination, *Atmos. Chem. Phys.*, 9, 7577-7589, <https://doi.org/10.5194/acp-9-7577-2009>, 2009.

Pitts, M. C., Poole, L. R., Dörnbrack, A., and Thomason, L. W., The 2009-2010 Arctic polar stratospheric cloud season: A CALIPSO perspective, *Atmos. Chem. Phys.*, 11, 2161-2177, <https://doi.org/10.5194/acp-11-2161-2011>, 2011.

Pitts, M. C., Poole, L. R., Lambert, A., Thomason, L. W., An assessment of CALIOP polar stratospheric cloud composition classification, *Atmos. Chem. Phys.*, 13, 2975-2988, doi:10.5194/acp-13-2975-2013, 2013.

Platt, C. M. R., Vaughan, M. A., and Austin, R. T., Characteristics of CALIPSO and CloudSat Backscatter at the Top Center Layers of Mesoscale Convective Systems and Relation to Cloud Microphysics, *J. Appl. Meteor. Climatol.*, 50, 368-378, doi:10.1175/2010JAMC2537.1, 2011.

Poole, L. R., and Pitts, M. C., Polar stratospheric cloud climatology based on SAM II observations from 1978-1989, *J. Geophys. Res.*, 99, 13083, doi:10.1029/94JD00411, 1994.

Prata, A. T., Young, S., Siems, S., and Manton, M., Lidar ratios of stratospheric volcanic ash and sulfate aerosols retrieved from CALIOP measurements, *Atmos. Chem. Phys.*, 17, 8599–8618, <https://doi.org/10.5194/acp-17-8599-2017>, 2017.

Read, W. G., Lambert, A., Bacmeister, J., Cofield, R. E., Christensen, L. E., Cuddy, D. T., Daffer, W. H., Drouin, B. J., Fetzer, E., Froidevaux, L., Fuller, R., Herman, R., Jarnot, R. F., Jiang, J. H., Jiang, Y. B., Kelly, K., Knosp, B. W., Kovalenko, L. J., Livesey, N. J., Liu, H. C., Manney, G. L., Pickett, H. M., Pumphrey, H. C., Rosenlof, K. H., Sabouchi, X., Santee, M. L., Schwartz, M. J., Snyder, W. V., Stek, P. C., Su, H., Takacs, L. L., Thurstans, R. P., Vomel, H., Wagner, P. A., Waters, J. W., Webster, C. R., Weinstock, E. M., and Wu, D. L., Aura Microwave Limb Sounder upper tropospheric and lower stratospheric H₂O and relative humidity with respect to ice validation, *J. Geophys. Res.*, 112, D24S35, doi:10.1029/2007JD008752, 2007.

Reichardt, J., Dörnbrack, A., Reichardt, S., Yang, P., and McGee, T. J., Mountain wave PSC dynamics and microphysics from ground-based lidar measurements and meteorological modeling, *Atmos. Chem. Phys.*, **4**, 1149–1165, 2004.

Santee, M. L., Lambert, A., Read, W. G., Livesey, N. J., Cofield, R. E., Cuddy, D. T., Daffer, W. H., Drouin, B. J., Froidevaux, L., Fuller, R. A., Jarnot, R. F., Knosp, B. W., Manney, G. L., Perun, V. S., Snyder, W. V., Stek, P. C.,
5 Thurstans, R. P., Wagner, P. A., Waters, J. W., Muscari, G., de Zafra, R. L., Dibb, J. E., Fahey, D. W., Popp, P. J., Marcy, T. P., Jucks, K. W., Toon, G. C., Stachnik, R. A., Bernath, P. F., Boone, C. D., Walker, K. A., Urban, J., and Murtagh, D., Validation of the Aura Microwave Limb Sounder HNO₃ measurements, *J. Geophys. Res.*, **112**, D24S40, doi:10.1029/2007JD008721, 2007.

Sarchilli, C., Adriani, A., Cairo, F., Di Donfrancesco, G., Buontempo, C., Snels, M., Moriconi, M. L., Deshler, T., Larsen,
10 N., Luo, B., Mauersberger, K., Ovarlez, J., Rosen, J., and Schreiner, J., Determination of polar stratospheric cloud particle refractive indices by use of in situ optical measurements and T-matrix calculations, *Appl. Opt.*, **44**, 3302–3311, <https://doi.org/10.1364/AO.44.003302>, 2005.

Schreiner, J., Voigt, C., Weisser, R., Kohlmann, A., Mauersberger, K., Deshler, T., Kröger, C., Rosen, J., Kjome, N., Larsen,
15 N., Adriani, A., Cairo, F., Di Donfrancesco, G., Ovarlez, J., Ovarlez, H., and Dörnbrack, A., Chemical, microphysical, and optical properties of polar stratospheric clouds, *J. Geophys. Res.*, **107**, 8313, doi:10.1029/2001JD000825, 2002.

Shindell, D. T.: Climate and ozone response to increased stratospheric water vapor, *Geophys. Res. Lett.*, **28**, 1551–1554, doi:10.1029/1999GL011197, 2001.

Solomon, S., Garcia, R. R., Rowland, F. S., and Wuebbles, D. J.: On the depletion of Antarctic ozone, *Nature*, **321**, 755–758, 1986.

20 Solomon, S.: Stratospheric ozone depletion: A review of concepts and history, *Rev. Geophys.*, **37**, 275–316, doi:10.1029/1999RG900008, 1999.

Spang, R., Hoffmann, L., Höpfner, M., Griessbach, S., Müller, R., Pitts, M. C., Orr, A. M. W., and Riese, M.: A multi-wavelength classification method for polar stratospheric cloud types using infrared limb spectra, *Atmos. Meas. Tech.*, **9**, 3619–3639, <https://doi.org/10.5194/amt-9-3619-2016>, 2016.

25 Spang, R., Hoffmann, L., Müller, R., Groöb, J.-U., Tritscher, I., Höpfner, M., Pitts, M., Orr, A., and Riese, M.: A climatology of polar stratospheric cloud composition between 2002 and 2012 based on MIPAS/Envisat observations, *Atmos. Chem. Phys.*, **18**, 5089–5113, <https://doi.org/10.5194/acp-18-5089-2018>, 2018.

Stephens, G. L., Vane, D. G., Boain, R. J., Mace, G. G., Sassen, K., Wang, Z., Illingworth, A. J., O'Connor, E. J., Rossow, W. B., Durden, S. L., Miller, S. D., Austin, R. T., Benedetti, A., Mitrescu, C., and the CloudSat Science Team, The
30 CloudSat mission and the A-Train: A new dimension of space-based observations of clouds and precipitation, *Bull. Am. Meteorol. Soc.*, **83**, 1771–1790, <https://doi.org/10.1175/BAMS-83-12-1771>, 2002.

Teitelbaum, H., and Sadourny, R.: The role of planetary waves in the formation of polar stratospheric clouds, *Tellus, Ser. A*, **50**, 302–312, <https://doi.org/10.3402/tellusa.v50i3.14528>, 1998.

Deleted: Atmos. Chem. Phys. Discuss.,
<https://doi.org/10.5194/acp-2017-898>, 2017

Teitelbaum, H., Moustauoui, M., and Fromm, M., Exploring polar stratospheric cloud and ozone minihole formation: The primary importance of synoptic-scale flow perturbation, *J. Geophys. Res.*, 106 (D22), 28173 – 28188, doi:10.1029/2000JD000065, 2001.

5 Tsias, A., Wirth, M., Carslaw, K. S., Biele, J., Mehrtens, H., Reichardt, J., Wedekind, C., Weiß, V., Renger, W., Neuber, R., von Zahn, U., Stein, B., Santacesaria, V., Stefanutti, L., Fierli, F., Bacmeister, J., and Peter, T., Aircraft lidar observations of an enhanced type Ia polar stratospheric clouds during APE-POLECAT, *J. Geophys. Res.*, 104, D19, 23961-23969, doi:10.1029/1998JD100055, 1999.

10 Voigt, C., Larsen, N., Deshler, T., Kröger, C., Schreiner, J., Mauersberger, K., Luo, B., Adriani, A., Cairo, F., Di Donfrancesco, G., Ovarlez, J., Ovarlez, H., Dörnbrack, A., Knudsen, B., and Rosen, J., In situ mountain-wave polar stratospheric cloud measurements: Implications for nitric acid trihydrate formation, *J. Geophys. Res.*, 108(D5), 8331, doi:10.1029/2001JD001185, 2003.

Waters, J. W., Froidevaux, L., Harwood, R. S., Jarnot, R. F., Pickett, H. M., Read, W. G., Siegel, P. H., Cofield, R. E., Filipiak, M. J., Flower, D. A., Holden, J. R., Lau, G. K. K., Livesey, N. J., Manney, G. L., Pumphrey, H. C., Santee, M. L., Wu, D. L., Cuddy, D. T., Lay, R. R., Loo, M. S., Perun, V. S., Schwartz, M. J., Stek, P. C., Thurstans, R. P., Boyles, 15 M. A., Chandra, K. M., Chavez, M. C., Chen, G. S., Chudasama, B. V., Dodge, R., Fuller, R. A., Girard, M. A., Jiang, J. H., Jiang, Y. B., Knosp, B. W., LaBelle, R. C., Lam, J. C., Lee, K. A., Miller, D., Oswald, J. E., Patel, N. C., Pukala, D. M., Quintero, O., Scaff, D., Van Snyder, W., Tope, M. C., Wagner, P. A., and Walch, M. J., The Earth Observing System Microwave Limb Sounder (EOS MLS) on the Aura satellite, *IEEE Trans. Geosci. Remote Sens.*, 44, 1075–1092, 2006.

20 Waugh, D. W., and Randel, W. J., Climatology of Arctic and Antarctic polar vortices using elliptical diagnostics, *J. Atmos. Sci.*, 56, 1594-1613, [https://doi.org/10.1175/1520-0469\(1999\)056<1594:COAAAP>2.0.CO;2](https://doi.org/10.1175/1520-0469(1999)056<1594:COAAAP>2.0.CO;2), 1999.

Waugh, D. W., Sobel, A. H., and Polvani, L. M., What is the polar vortex and how does it influence weather, *Bull. Amer. Meteor. Soc.*, 98, 37-44., <https://doi.org/10.1175/BAMS-D-15-00212.1>, 2017.

25 Wegner, T., Pitts, M. C., Poole, L. R., Tritscher, I., Grooß, J.-U., and Nakajima, H., Vortex-wide chlorine activation by a mesoscale PSC event in the Arctic winter of 2009/10, *Atmos. Chem. Phys.*, 16, 4569-4577, doi:10.5194/acp-16-4569-2016, <https://doi.org/10.5194/acp-16-4569-2016>, 2016.

Weigel, R., Volk, C. M., Kandler, K., Hösen, E., Günther, G., Vogel, B., Grooß, J.-U., Khaykin, S., Belyaev, G. V., and S. Borrmann, Enhancements of the refractory submicron aerosol fraction in the Arctic polar vortex: feature or exception?, *Atmos. Chem. Phys.*, 14, 12319–12342, doi:10.5194/acp-14-12319-2014, 2014.

30 Wespes, C., Hurtmans, D., Clerbaux, C., Santee, M. L., Martin, R. V., and Coheur, P. F., Global distributions of nitric acid from IASI/MetOP measurements, *Atmos. Chem. Phys.*, 9, 7949-7962, <https://doi.org/10.5194/acp-9-7949-2009>, 2009.

Wilson, J. C., Stolzenburg, M. R., Clark, W. E., Loewenstein, M., Ferry, G. V., and Chan, K. R., Measurements of Condensation Nuclei in the Airborne Arctic Stratospheric Expedition: Observations of Particle Production in the Polar Vortex, *Geophys. Res. Lett.*, 17, 4, 361-364, 1990.

Winker, D. M., McGill, M., and Hunt, W. H.: Initial performance assessment of CALIOP, *Geophys. Res. Lett.*, 34, L19803, doi:10.1029/2007GL030135, 2007.

Winker, D. M., M. A. Vaughan, A. H. Omar, Y. Hu, K. A. Powell, Z. Liu, W. H. Hunt, and S. A. Young, Overview of the CALIPSO Mission and CALIOP Data Processing Algorithms, *J. Atmos. Oceanic Technol.*, 26, 2310–2323, doi:10.1175/2009JTECHA1281.1, 2009.

WMO (World Meteorological Organization), Antarctic Ozone Bulletin, No. 8/2006, Geneva, Switzerland, July 2007.

WMO (World Meteorological Organization), Scientific Assessment of Ozone Depletion: 2014, Global Ozone Research and Monitoring Project-Report No. 55, Geneva, Switzerland, 2015.

Young, S. A., and Vaughan, M. A., The Retrieval of Profiles of Particulate Extinction from Cloud-Aerosol Lidar Infrared Pathfinder Satellite Observations (CALIPSO) Data: Algorithm Description, *J. Atmos. Oceanic Technol.*, 26, 1105–1119, doi:10.1175/2008JTECHA1221.1, 2009.

Zhang, J., Tian, W., Chipperfield, M., Xie, F., and Huang, J., Persistent shift of the Arctic polar vortex towards the Eurasian continent in recent decades, *Nat. Climate Change*, 6, 1094–1099, doi:10.1038/nclimate3136, 2016.

Zhu, Y., Toon, O. B., Pitts, M. C., Lambert, A., Bardeen, C., and Kinnison, D. E., Comparing simulated PSC optical properties with CALIPSO observations during the 2010 Antarctic Winter, *J. Geophys. Res. Atmos.*, 122, 1175–1202, doi:10.1002/2016JD025191, 2017.

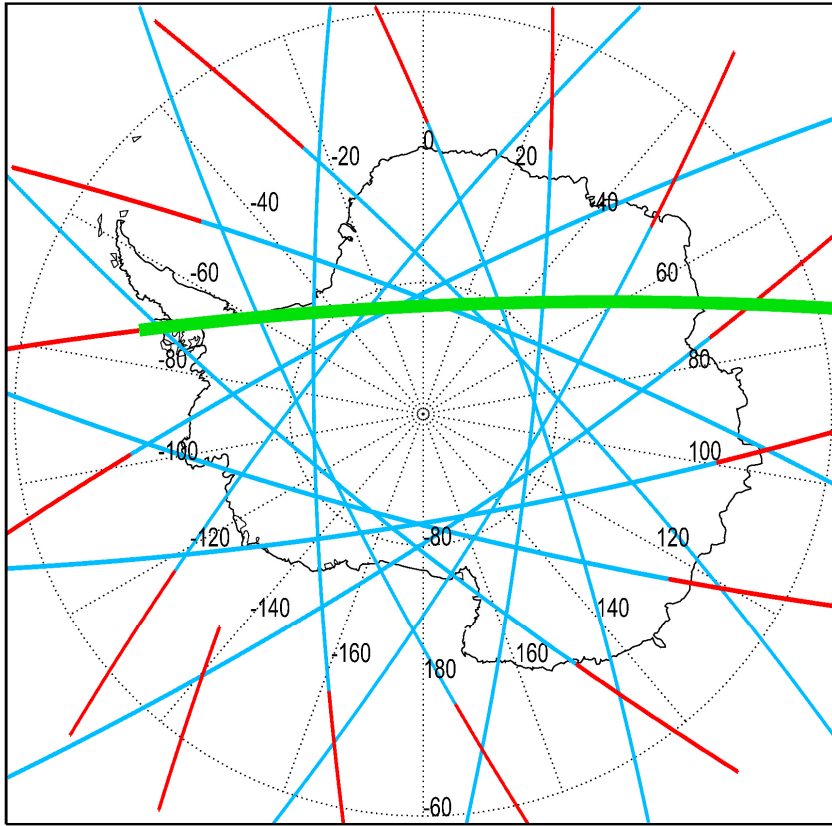


Figure 1: CALIPSO orbital coverage over the polar region of the Southern Hemisphere on 17 July 2008. Blue (red) lines depict nighttime (daytime) orbit segments. The CALIOP curtain along the orbit highlighted in green is shown in Fig. 2.

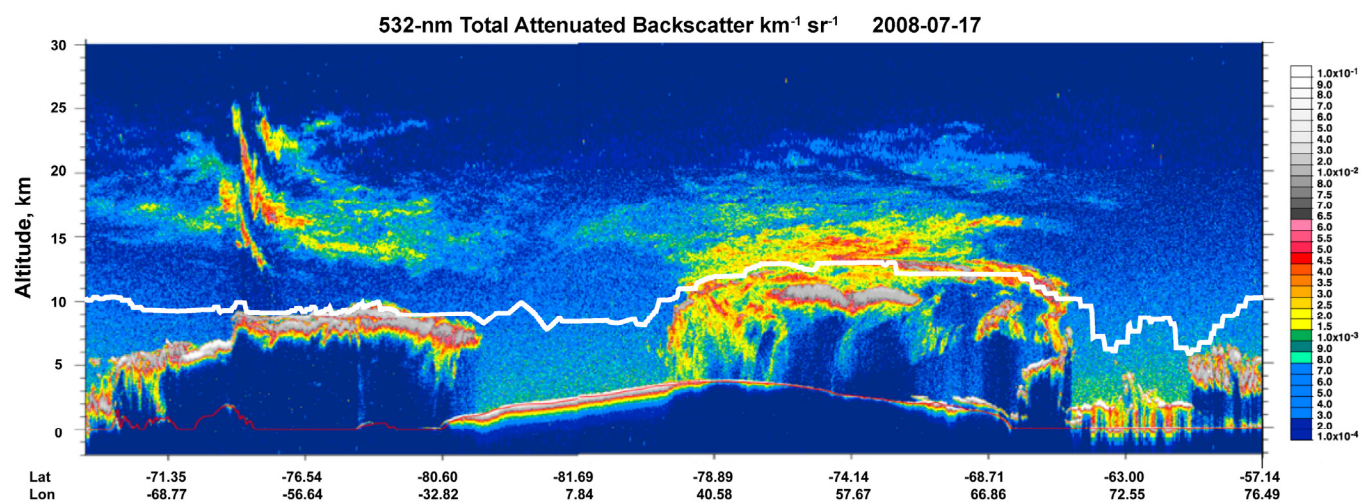


Figure 2: Orbital curtain of CALIOP 532-nm total attenuated backscatter coefficient ($\text{km}^{-1}\text{sr}^{-1}$) along the single orbit highlighted in green in Fig. 1. The MERRA-2 tropopause height is indicated by the solid white line.

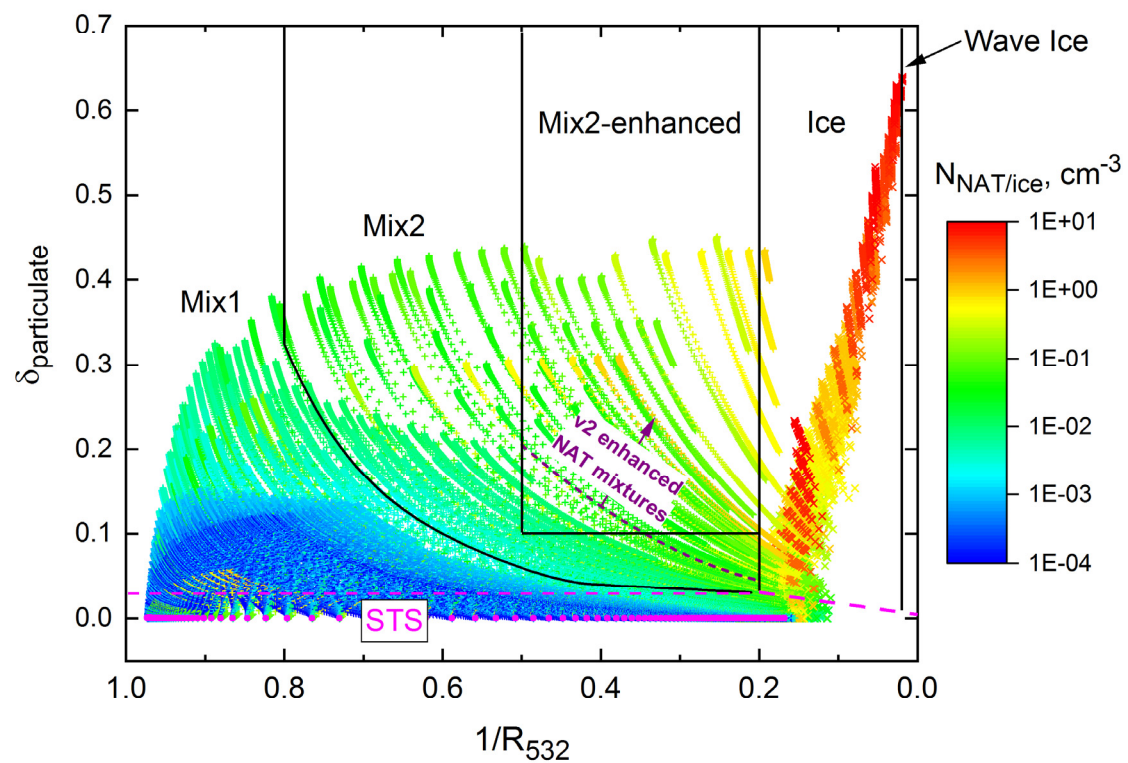


Figure 3: Theoretical optical calculations for non-equilibrium liquid-NAT and liquid-ice mixtures, illustrating the CALIOP v1 PSC composition classification scheme. The dashed purple curve represents the lower boundary of the v2 enhanced NAT mixtures composition class, as discussed in the text and in Fig. 4.

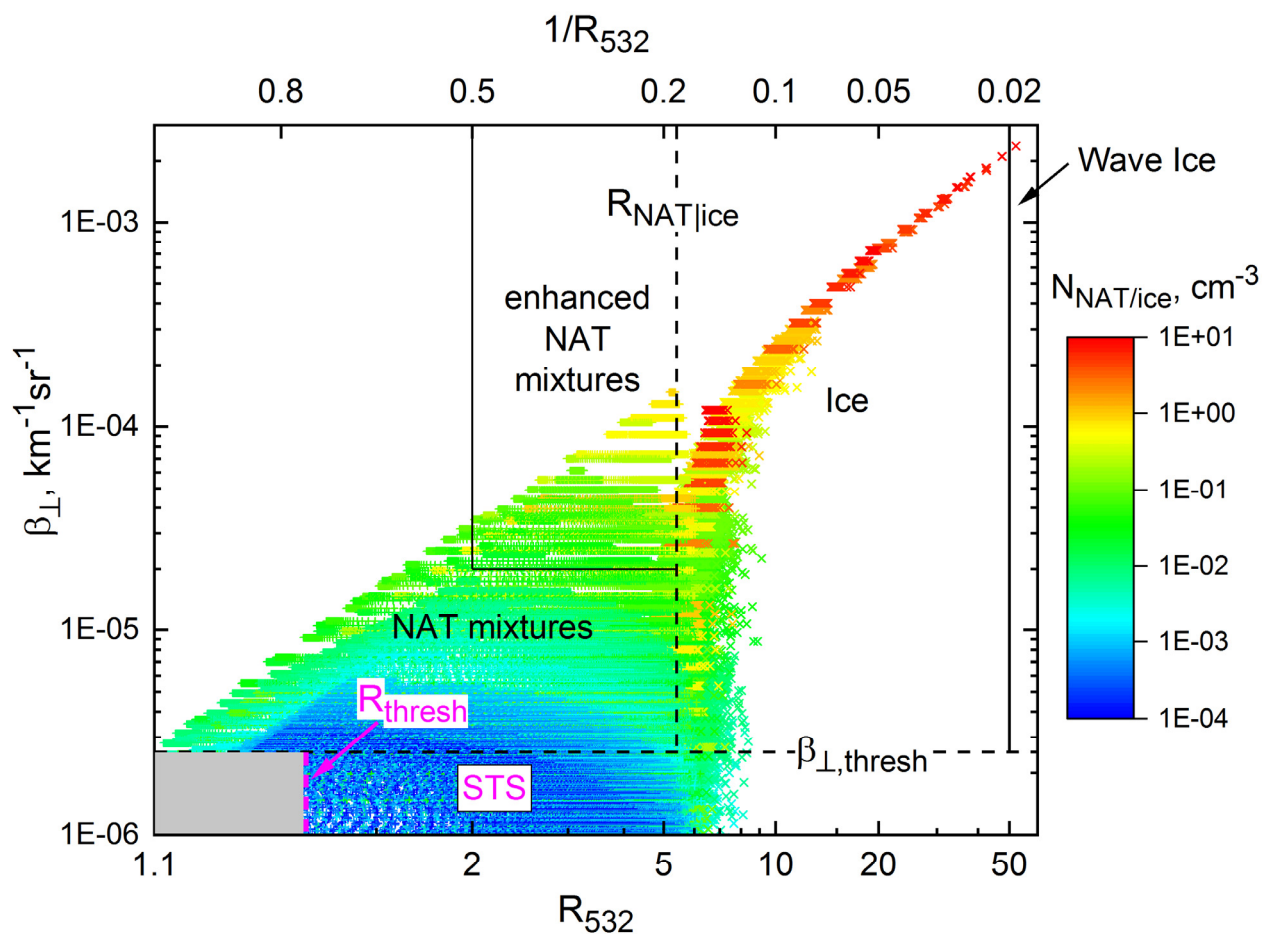


Figure 4: Theoretical optical calculations for non-equilibrium liquid-NAT and liquid-ice mixtures, illustrating the v2 PSC composition classification scheme. The grey box at the lower left represents points that fall below both CALIOP v2 PSC detection thresholds and are classified as non-features.

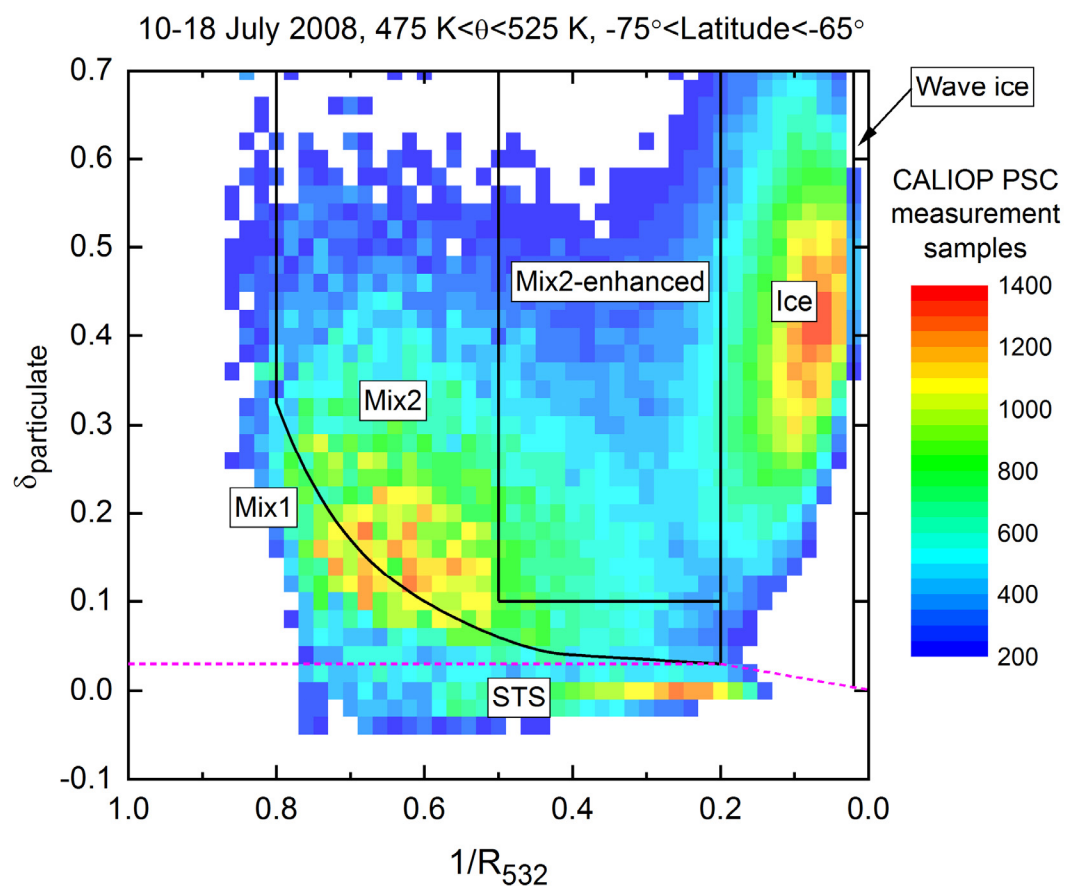


Figure 5: 2-D histogram of CALIOP PSC data for the period 10-18 July 2008, latitudes 65°S-75°S, and potential temperatures (θ) = 475 K-525 K plotted in the CALIOP v1 composition classification coordinate system.

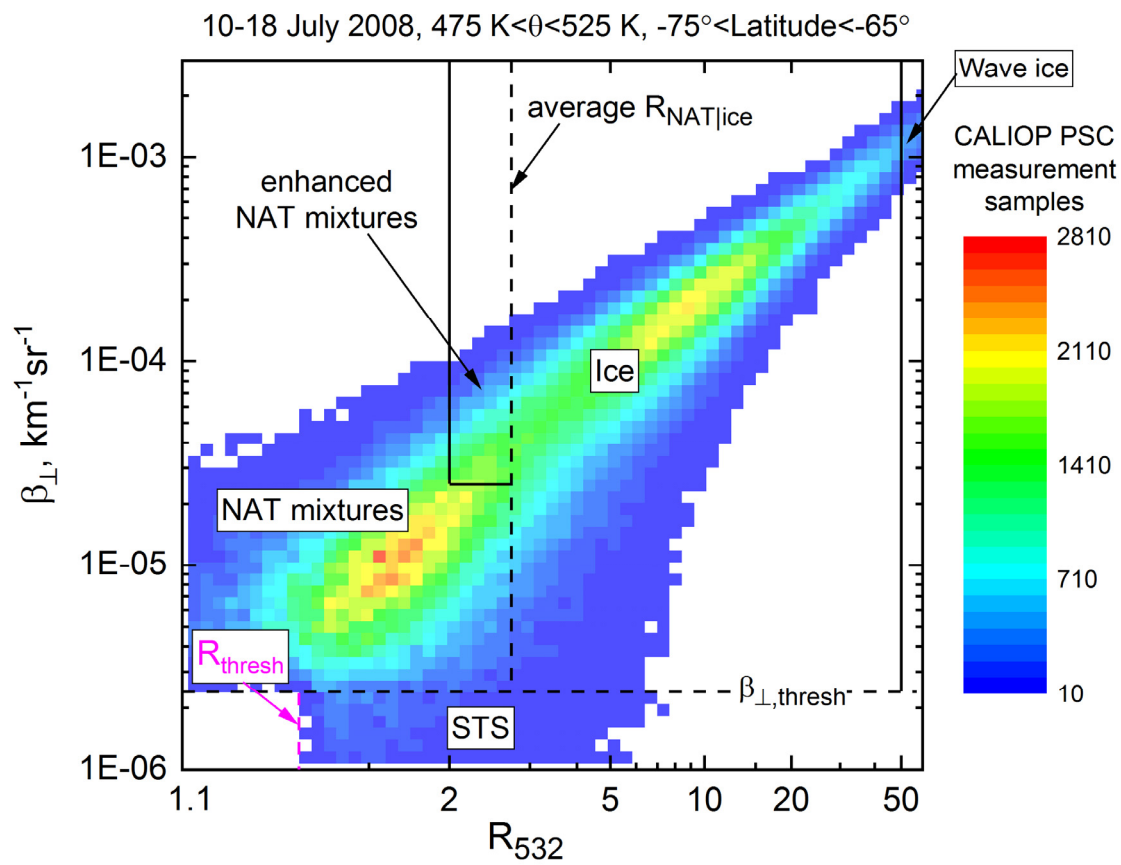


Figure 6: As in Fig. 5, but plotted in the CALIOP v2 composition classification coordinate system.

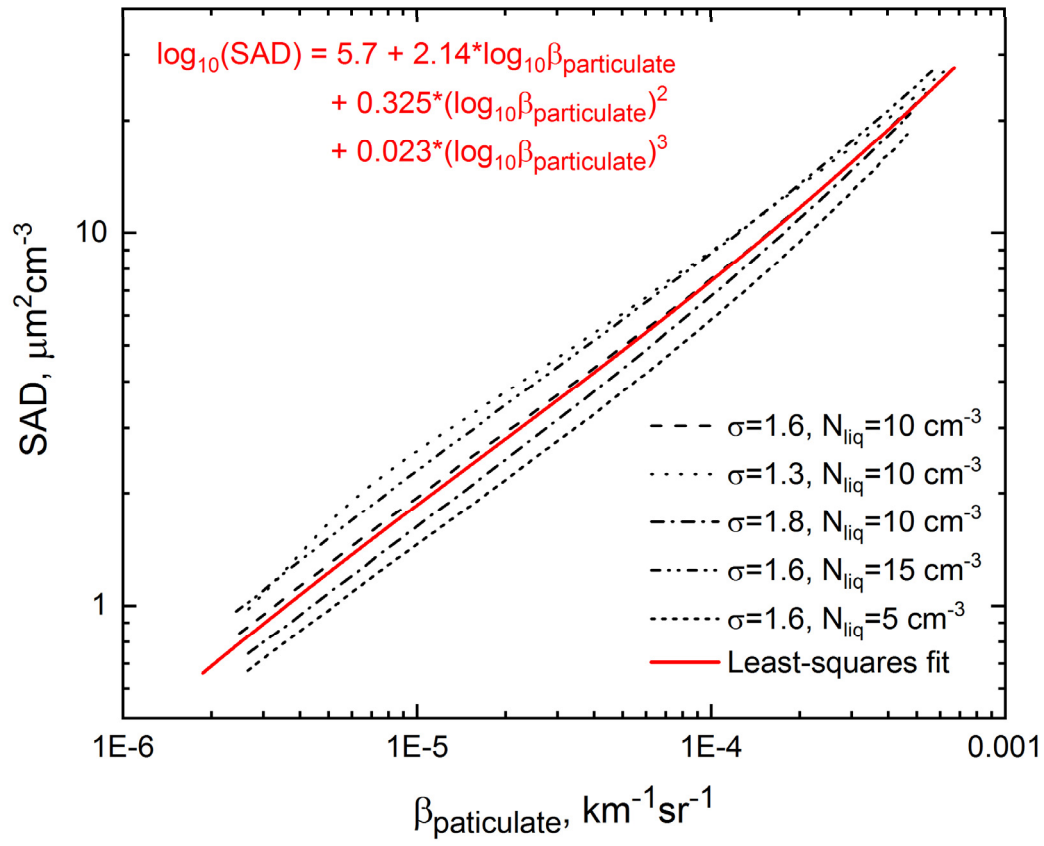


Figure 7: Theoretical particulate surface area density (SAD) vs. $\beta_{\text{particulate}}$ for various combinations of liquid particle number density N_{liq} and lognormal geometric standard deviation σ , along with the 3rd order polynomial least-squares fit.

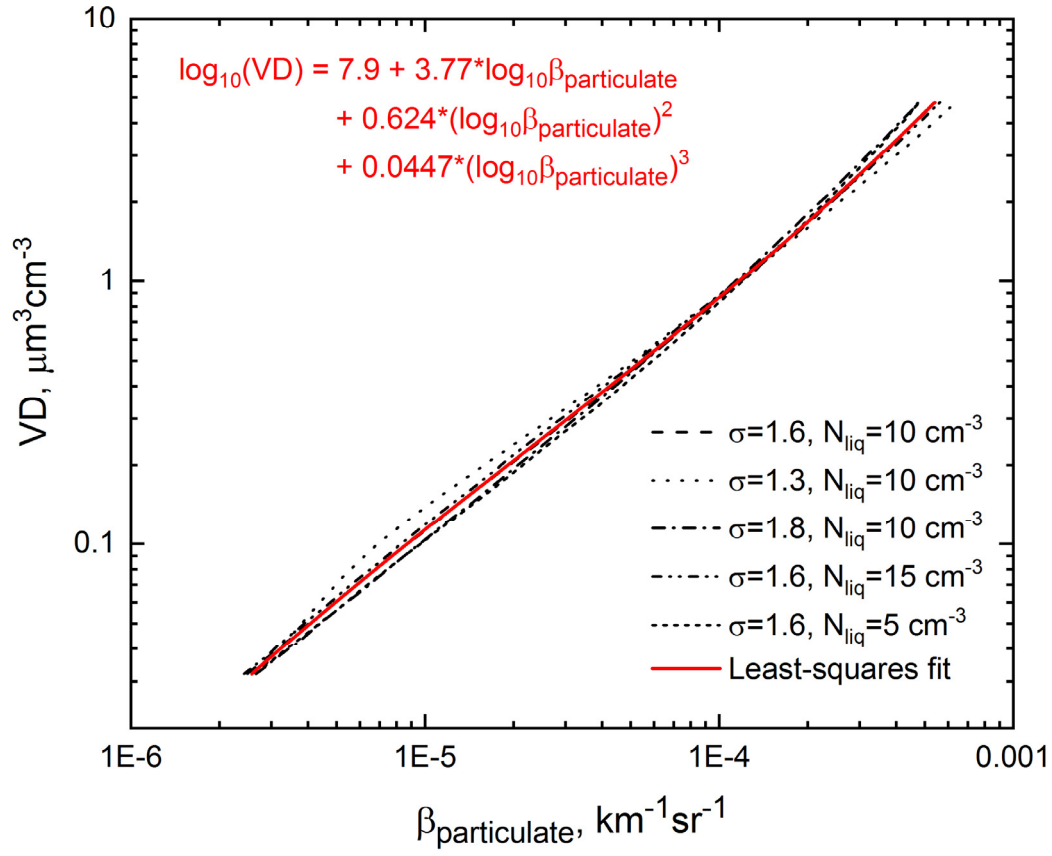


Figure 8: Theoretical particulate volume density (VD) vs. $\beta_{\text{particulate}}$ for various combinations of liquid particle number density N_{liq} and lognormal geometric standard deviation σ , along with the 3rd order polynomial least-squares fit.

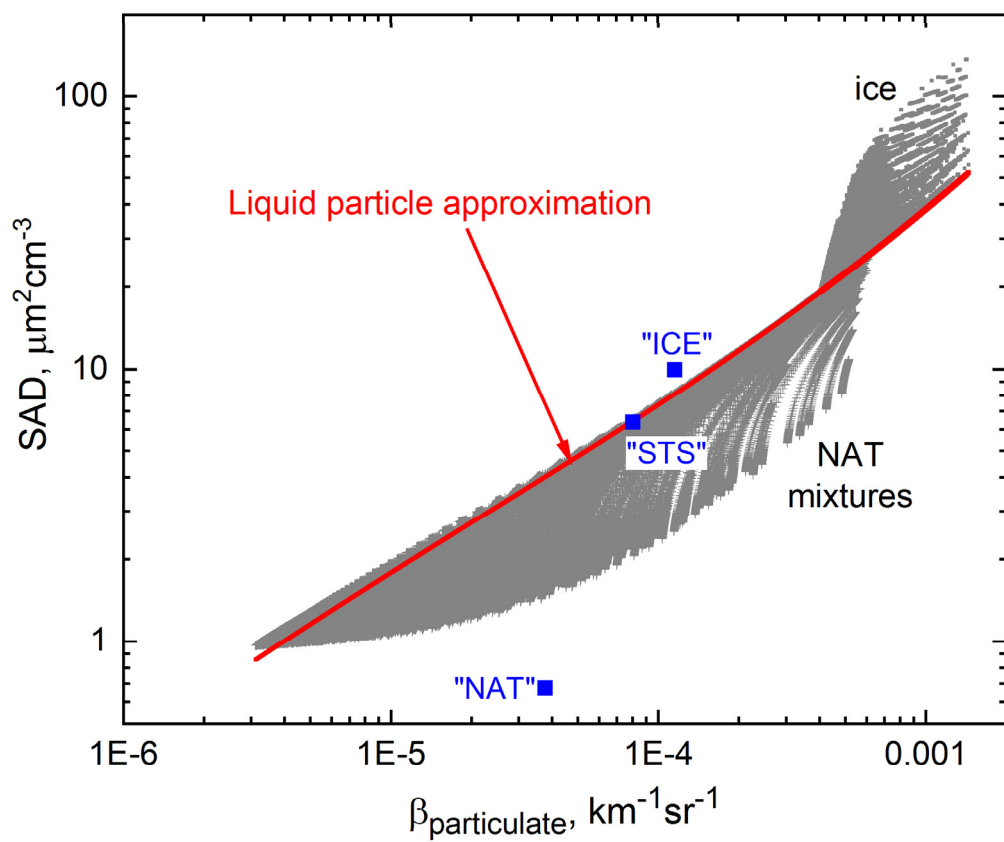


Figure 9: Theoretical particulate surface area density (SAD) vs. $\beta_{\text{particulate}}$ from the full suite of results for NAT mixtures and ice, compared with the liquid particle approximation. Blue symbols are computed values based on bimodal lognormal size distribution fits to in situ optical particle counter measurements within STS, NAT, and ice PSC layers (Deshler et al., 2003).

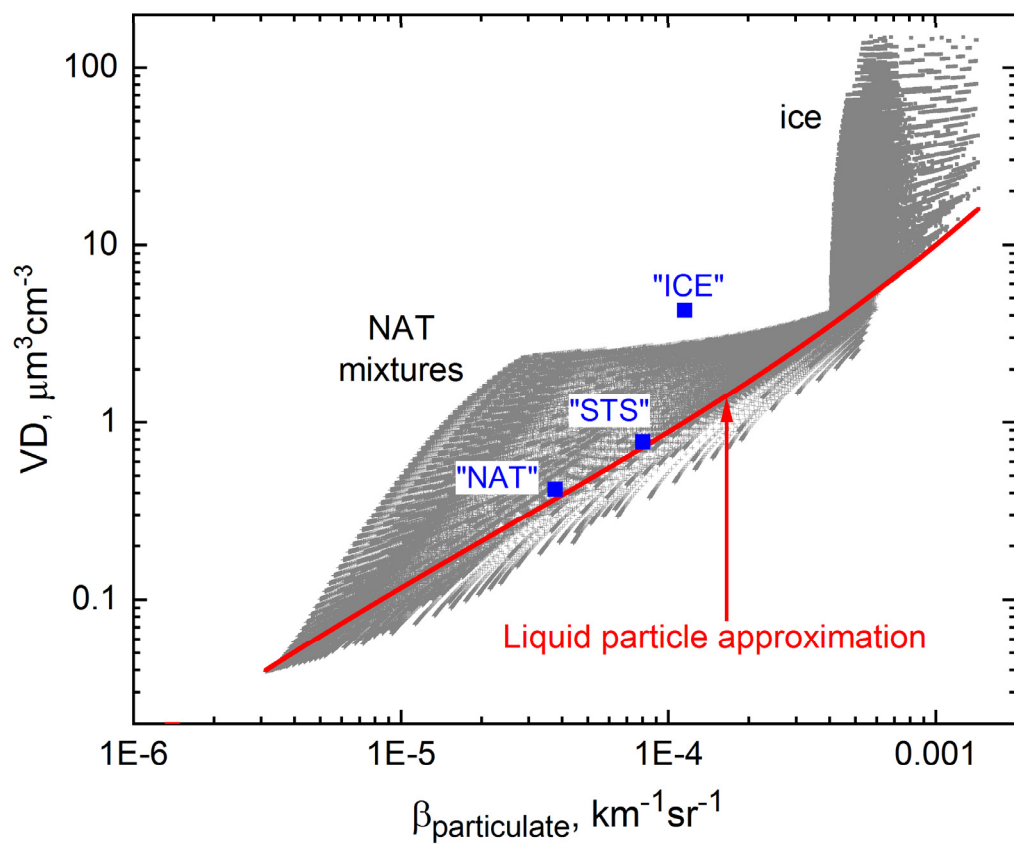


Figure 10: Theoretical particulate volume density (VD) vs. $\beta_{\text{particulate}}$ from the full suite of results for NAT mixtures and ice, compared with the liquid particle approximation. Blue symbols are computed values based on bimodal lognormal size distribution fits to in situ optical particle counter measurements within STS, NAT, and ice PSC layers (Deshler et al., 2003).

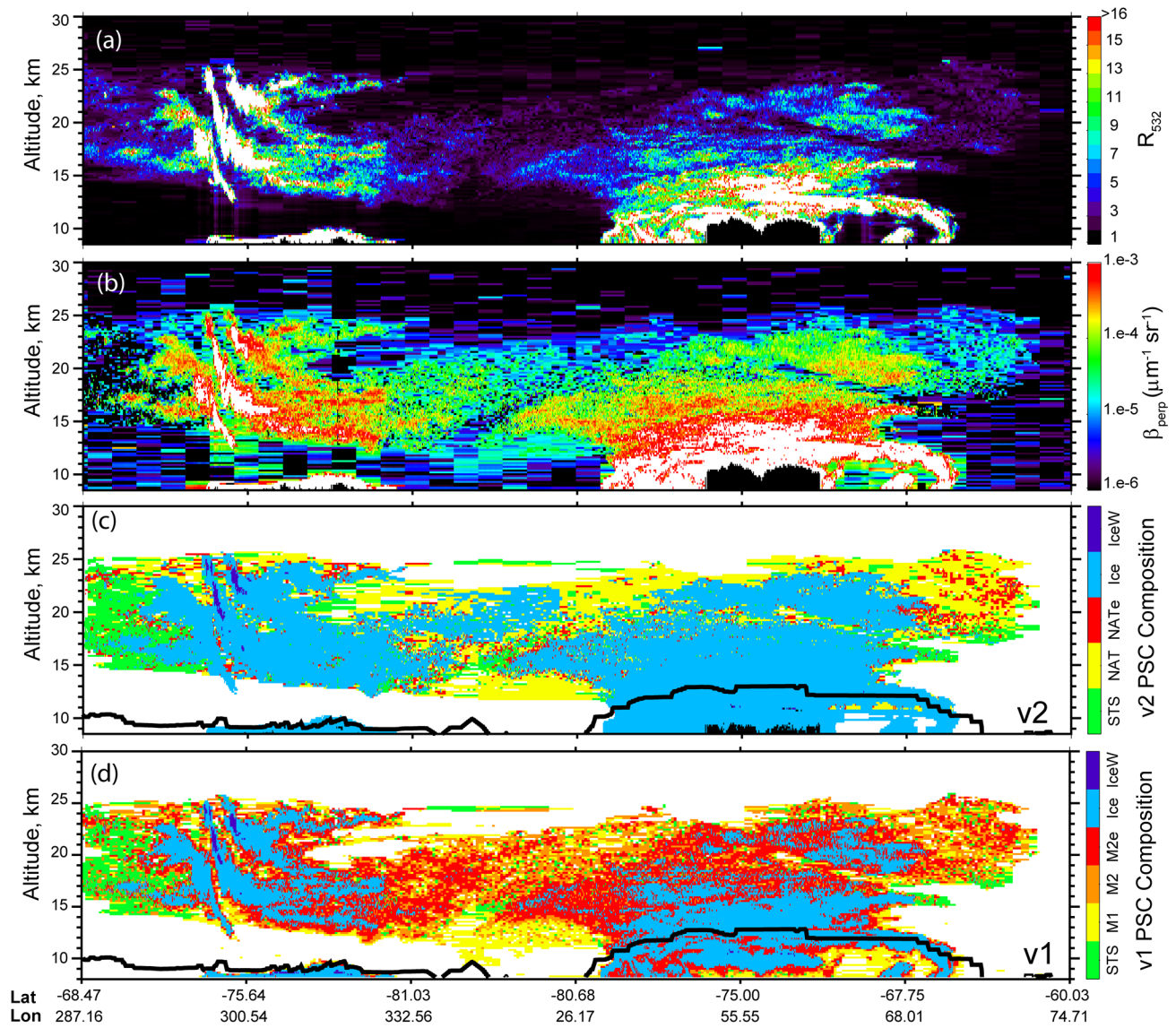
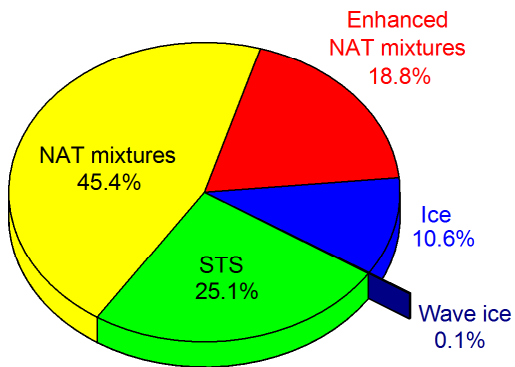


Figure 11: Curtains of CALIOP (a) R_{532} , (b) β_L , (c) v2 PSC composition mask, and (d) v1 PSC composition mask along the orbit track on 17 July 2008 highlighted in green in Fig.1. The location of the MERRA-2 “blended” tropopause is shown in panels (c) and (d) by the solid black line.

CALIOP Antarctic PSCs: 2009 v1
3.26E7 measurement samples



CALIOP Antarctic PSCs: 2009 v2
3.89E7 measurement samples

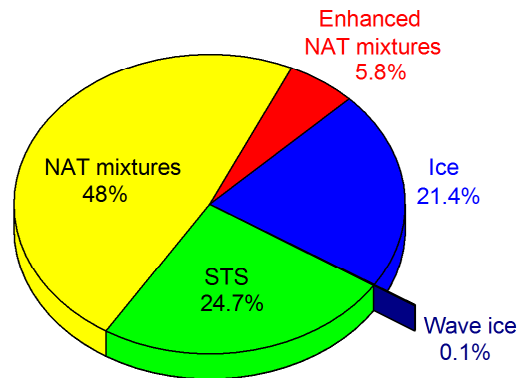


Figure 12: Comparison between v1 and v2 CALIOP PSC measurements during the 2009 Antarctic winter and their breakdown by composition classification. Data are restricted to altitudes 4 km or more above the tropopause to avoid distortion of statistics by ubiquitous underlying cirrus.

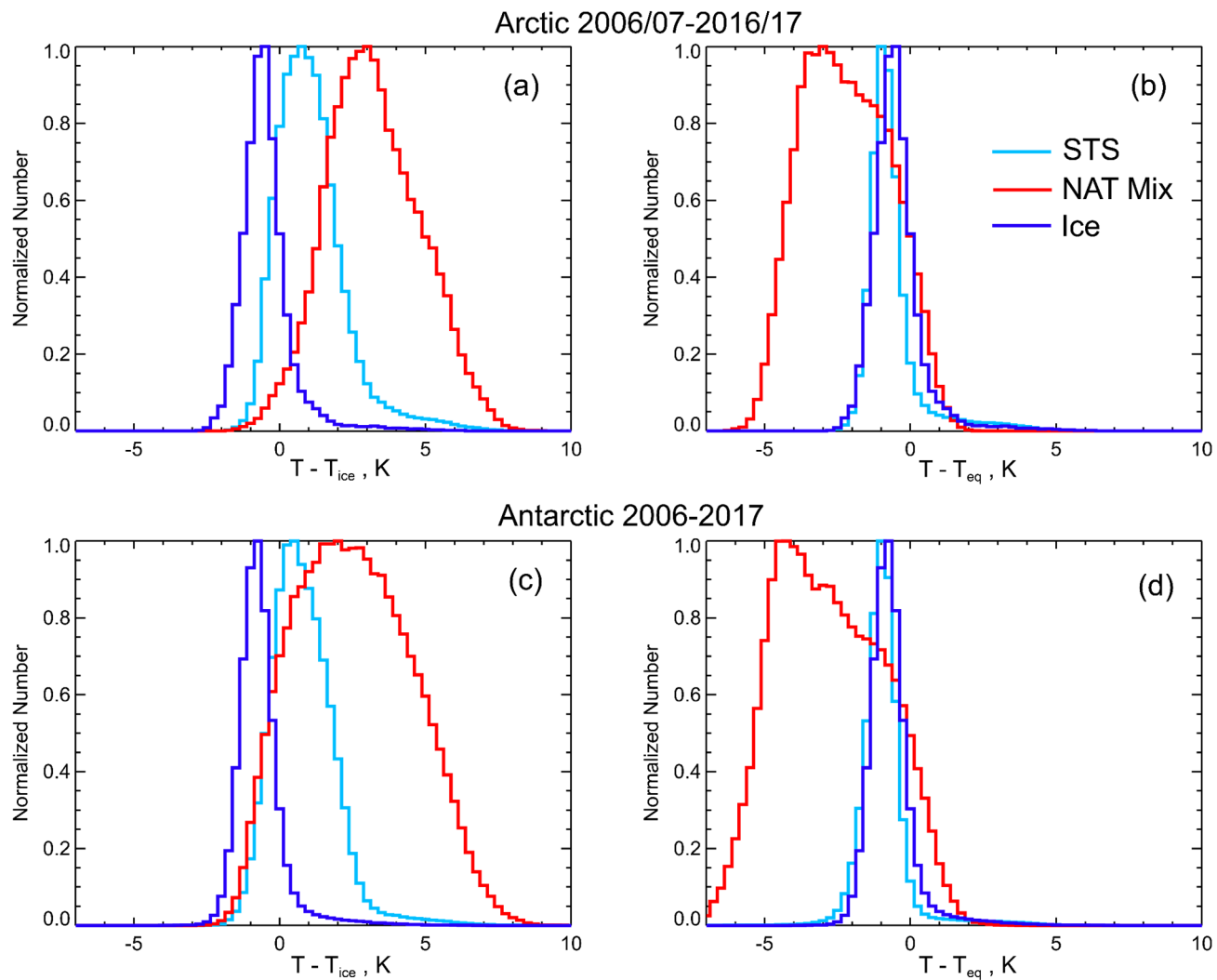


Figure 13: Histograms of CALIOP v2 PSC measurements at 21 km from 11 Arctic and 12 Antarctic winters as a function of (a, c) $T - T_{ice}$ and (b, d) $T - T_{eq}$ by composition: STS (light blue); NAT mixtures, including enhanced NAT mixtures (red); and ice, including wave ice (dark blue).

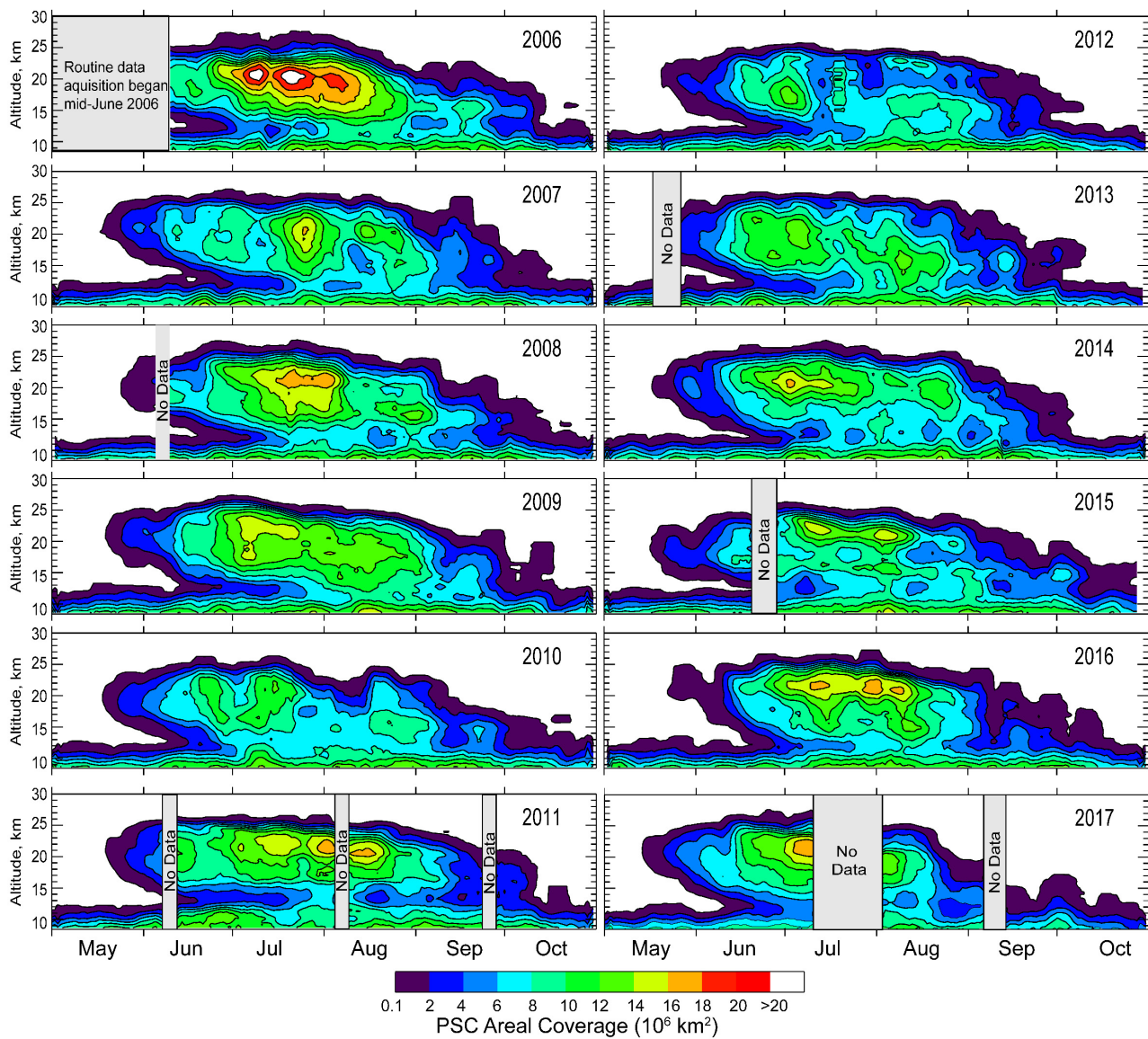


Figure 14: Time series of total PSC areal coverage over the Antarctic region as a function of altitude for each of the 12 Antarctic winters in the CALIOP v2 data record.

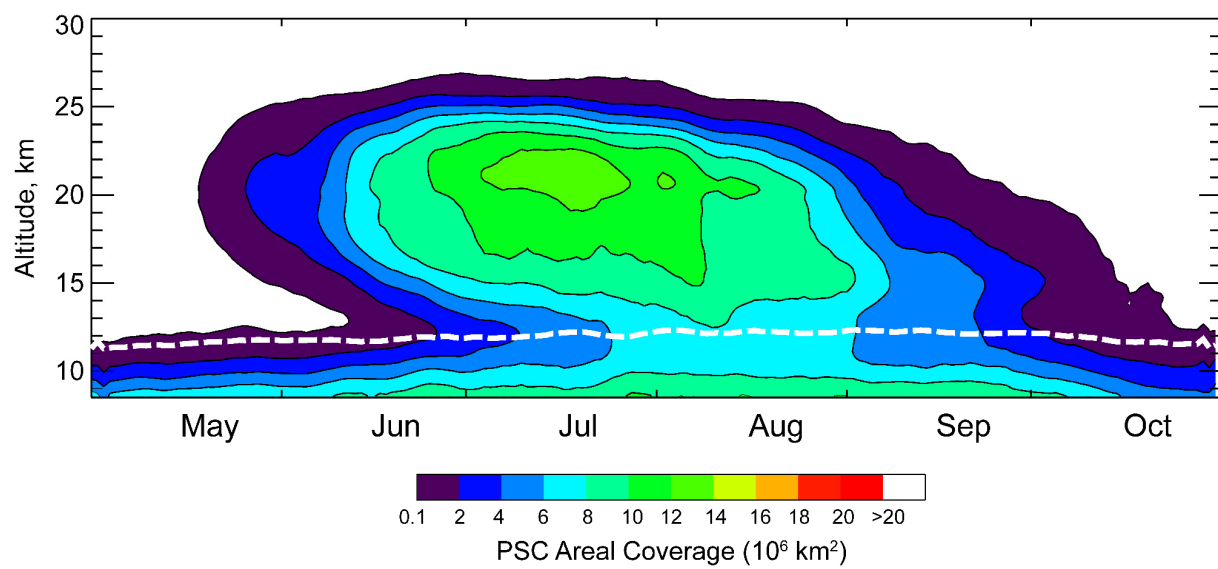


Figure 15: Twelve-year mean daily PSC areal coverage over the Antarctic. The climatological daily maximum MERRA-2 tropopause height is indicated by the dashed white line.

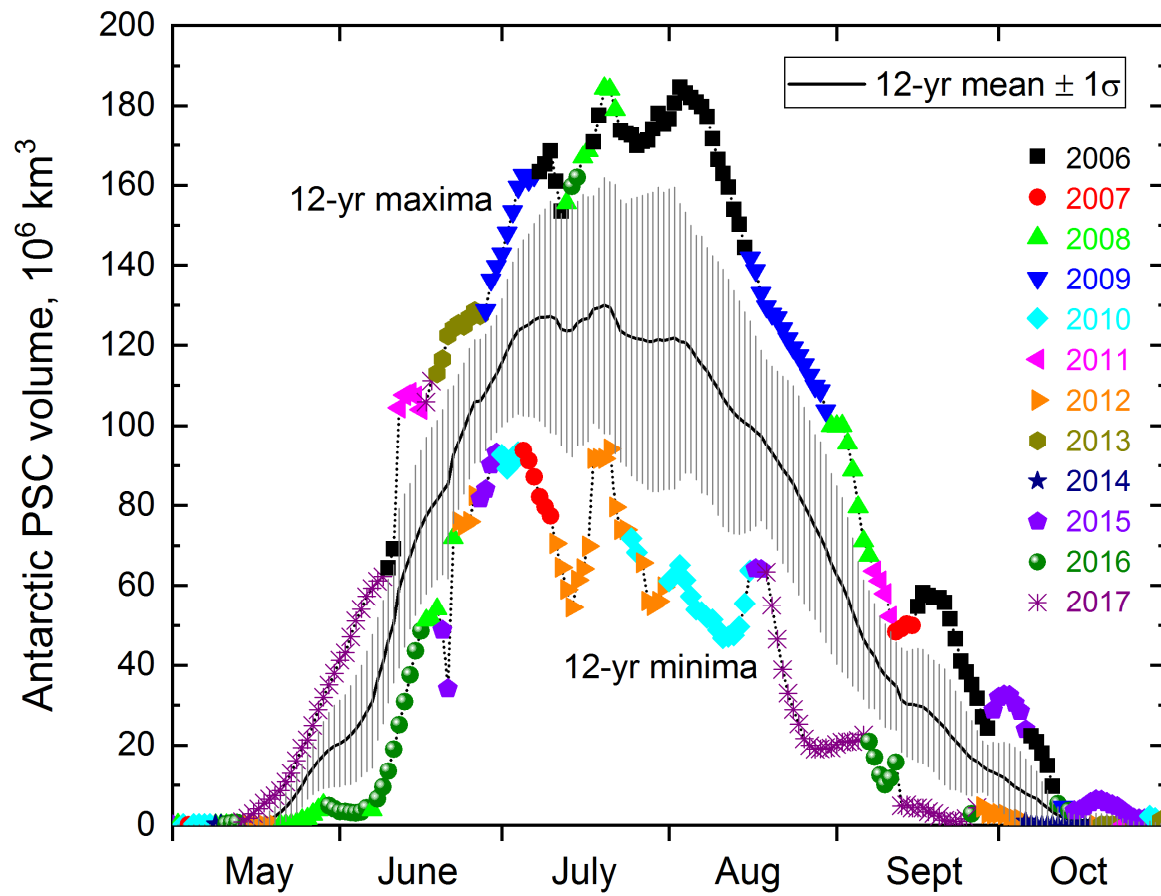


Figure 16: Time series of the 12-year mean, standard deviation, and range of daily values of Antarctic PSC spatial volume (daily areal coverage integrated over altitude). The daily maximum and minimum values are color-coded according to the year in which they occurred.

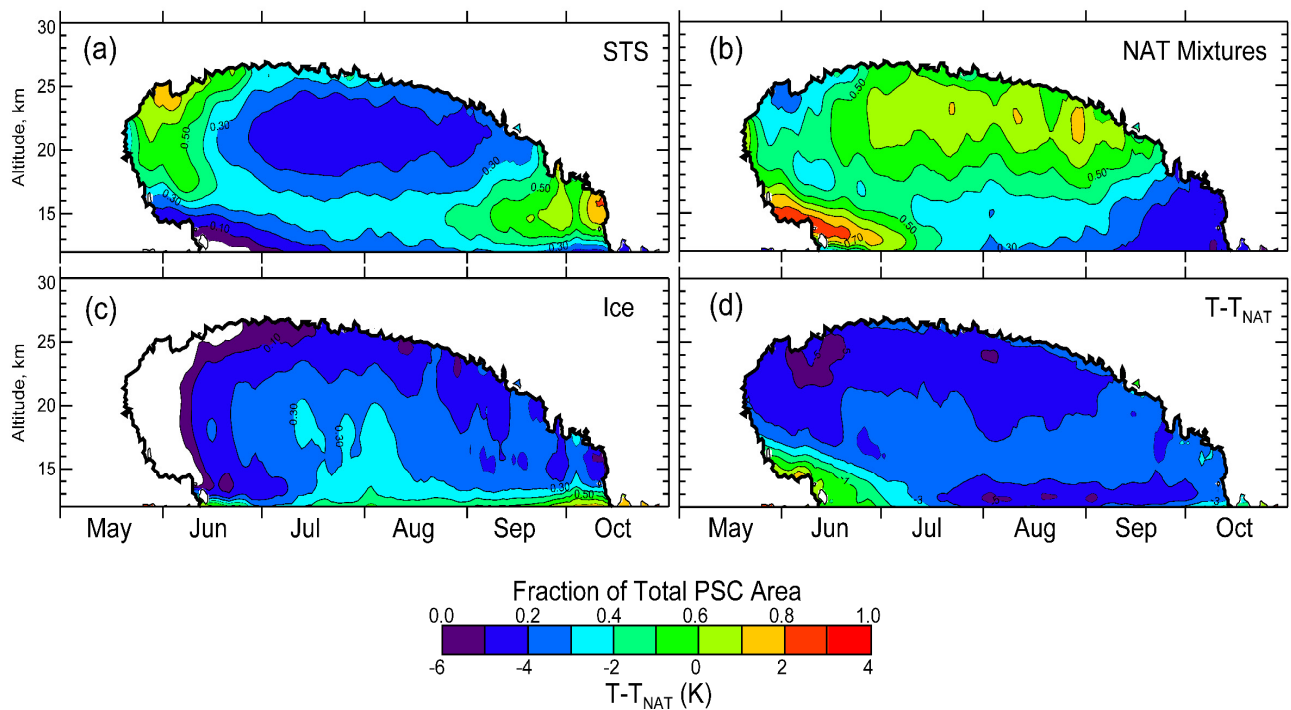


Figure 17: Twelve-year mean relative spatial coverage (composition-specific area normalized by total PSC area) for (a) STS; (b) NAT mixtures, including enhanced NAT mixtures; and (c) ice, including wave ice. For additional perspective, (d) shows 12-year mean distribution of $T-T_{\text{NAT}}$. The thick black contour line on each of the color panels corresponds to the range of days and altitudes where PSCs (of any composition) were observed in at least six of the twelve Antarctic seasons.

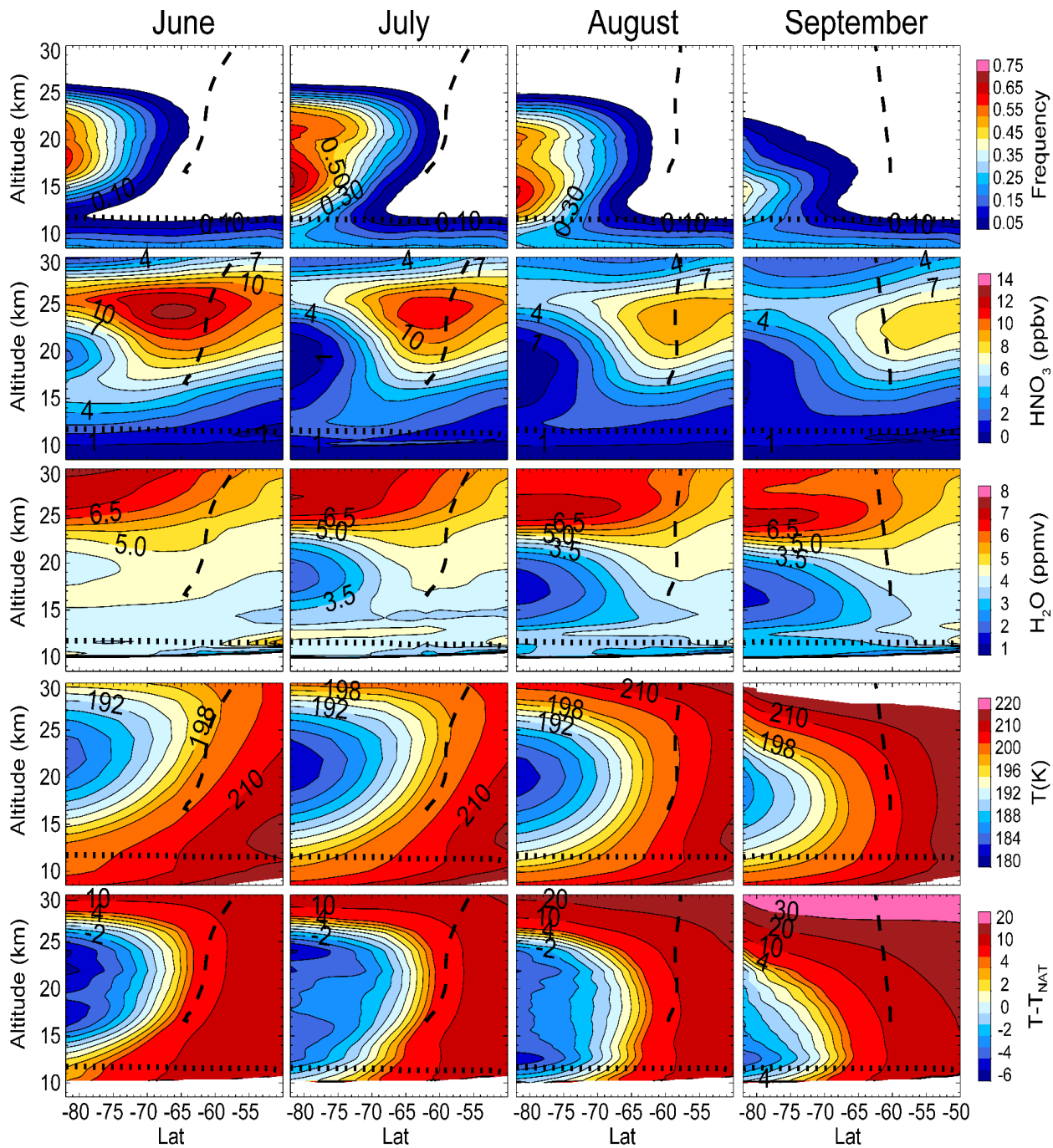


Figure 18: Latitude/altitude cross sections of 12-year average, monthly zonal mean (top row) Antarctic PSC occurrence frequency, (second row) cloud-free MLS HNO_3 , (third row) cloud-free MLS H_2O , (fourth row) MERRA-2 temperature, and (fifth row) $T - T_{\text{NAT}}$. For reference, the mean location of the vortex edge (heavy dashed line) and MERRA-2 tropopause height (dotted line) are indicated in the panels.

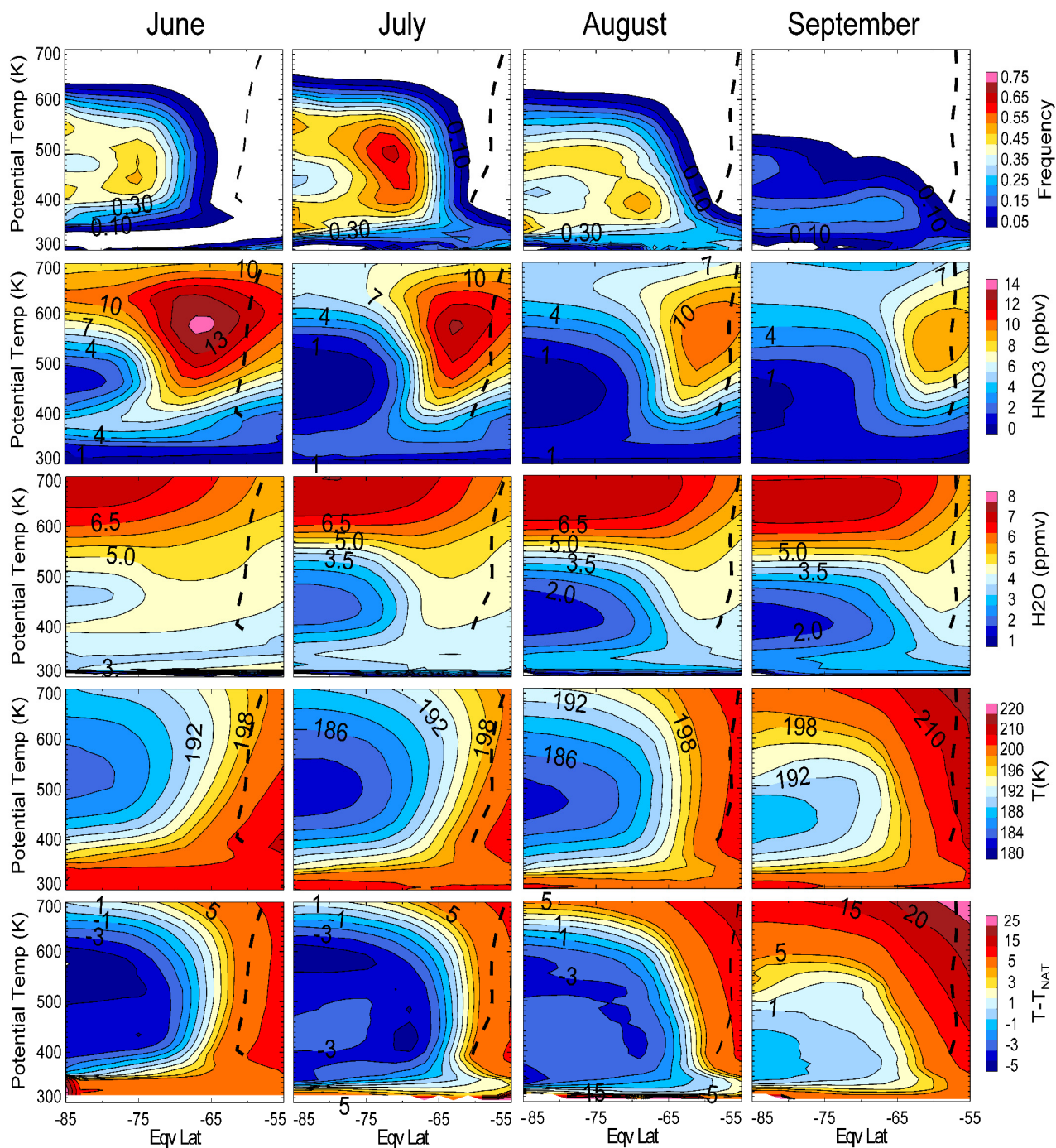


Figure 19: Equivalent latitude/potential temperature cross sections of 12-year average, monthly zonal mean (top row) Antarctic PSC occurrence frequency, (second row) cloud-free MLS HNO₃, (third row) cloud-free MLS H₂O, (fourth row) MERRA-2 temperature, and (fifth row) $T - T_{\text{NAT}}$. For reference, the mean location of the vortex edge (heavy dashed line) is indicated in the panels.

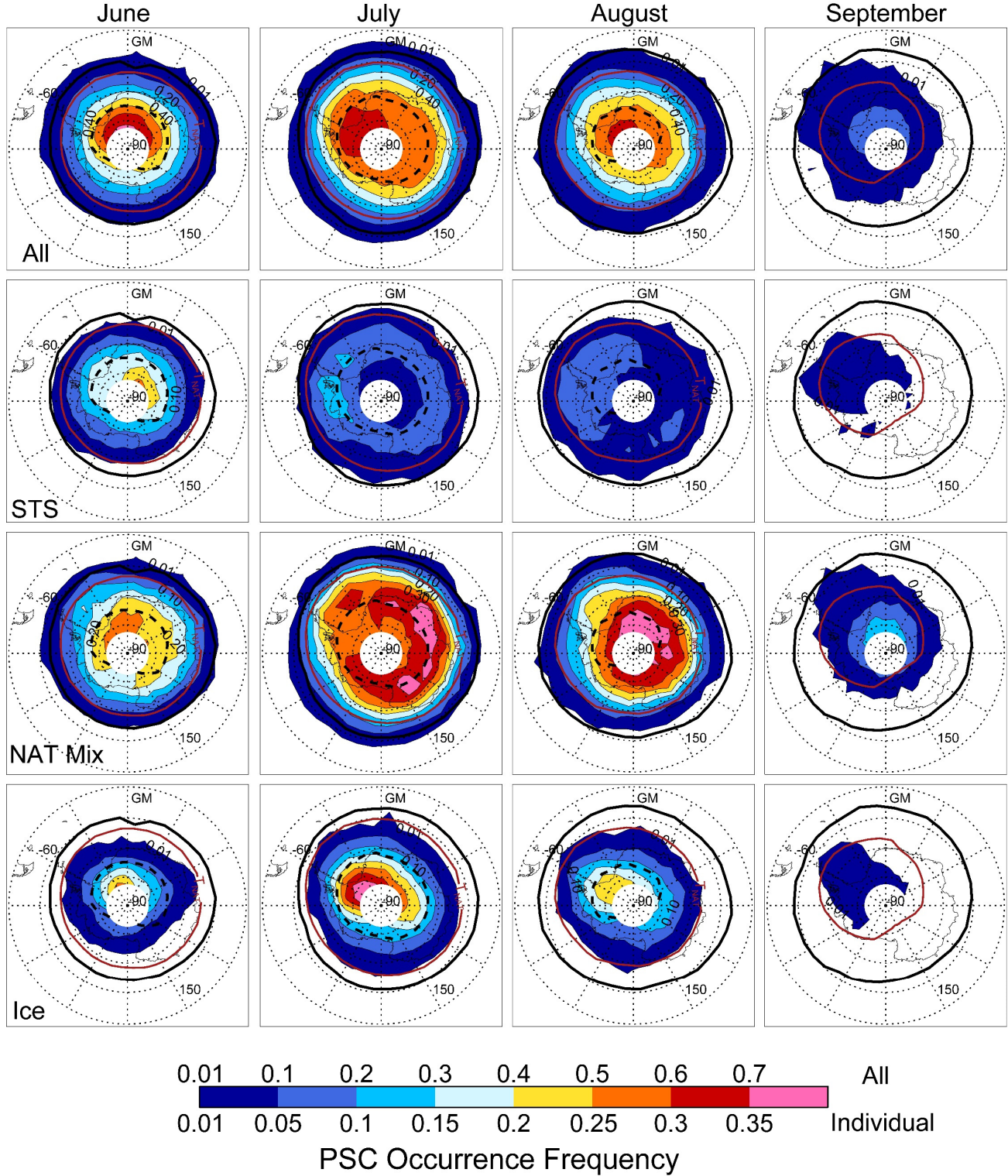


Figure 20: Twelve-year average, monthly mean polar maps of Antarctic PSC occurrence frequency at $\theta=500$ K (~ 20 km). The top row shows the occurrence frequency for all PSCs, while the subsequent rows display the occurrence frequencies of STS, NAT mixtures (including enhanced NAT), and ice (including wave ice), respectively. Overlaid in the panels are the mean location of the edge of the vortex (black line) and the boundaries of the regions where the mean temperature is below T_{NAT} (solid red line) and below T_{ice} (dashed black line). Light gray regions indicate latitudes not sampled by CALIOP. Note the different color scales for “all” PSCs and “individual” compositions.

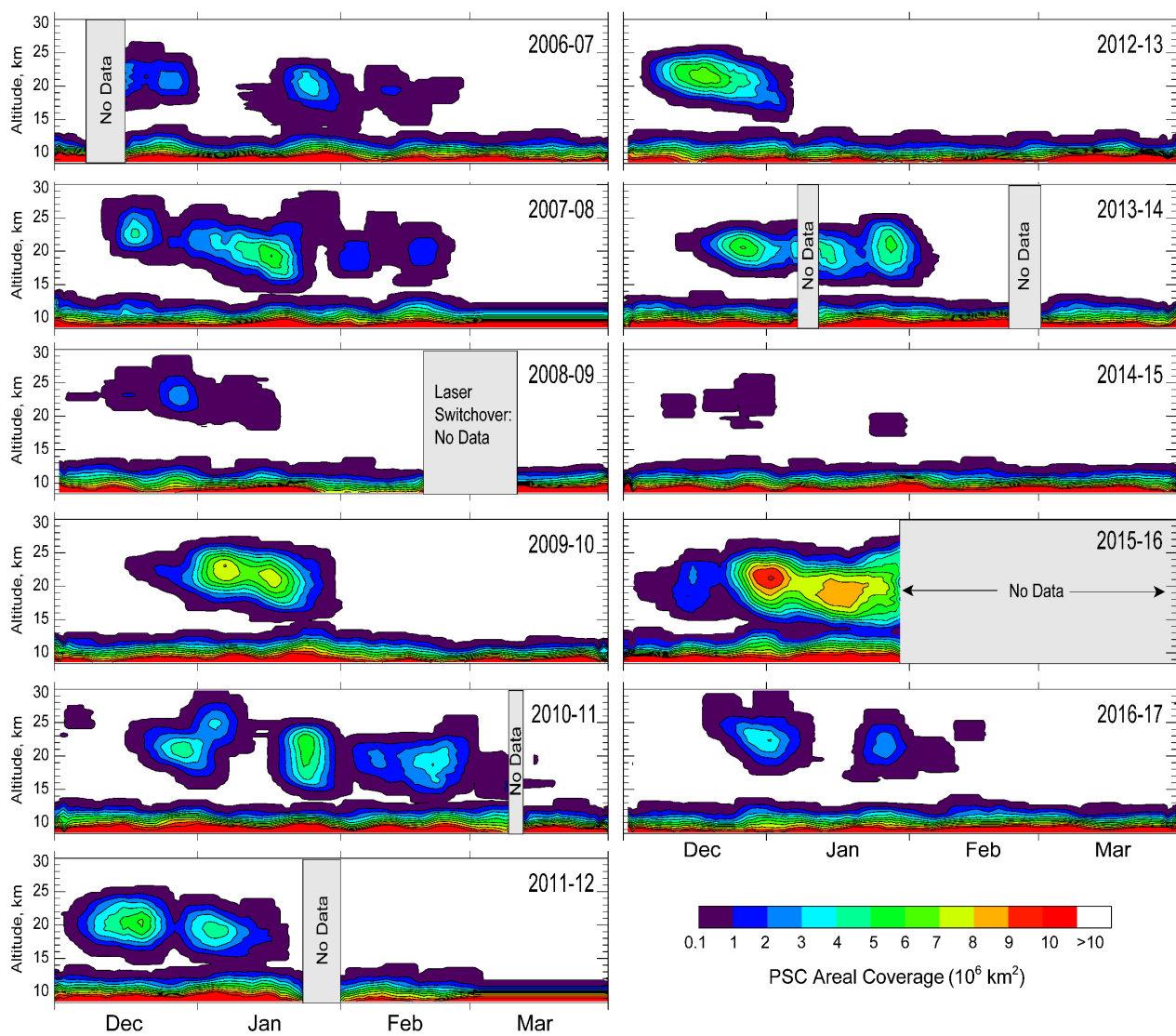


Figure 21: Daily PSC areal coverage as a function of altitude for each of the 11 Arctic winters in the CALIOP v2 data record. Note the change in color scale compared with Fig. 14.

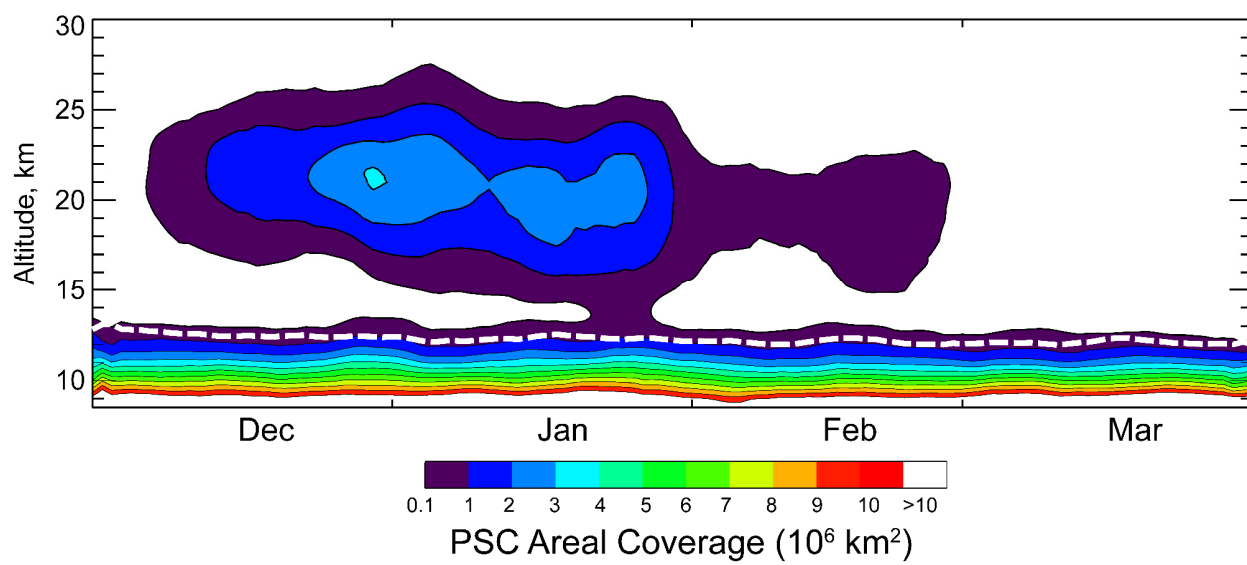


Figure 22: Eleven-year mean daily PSC areal coverage over the Arctic. The climatological daily maximum MERRA-2 tropopause height is indicated by the dashed white line.

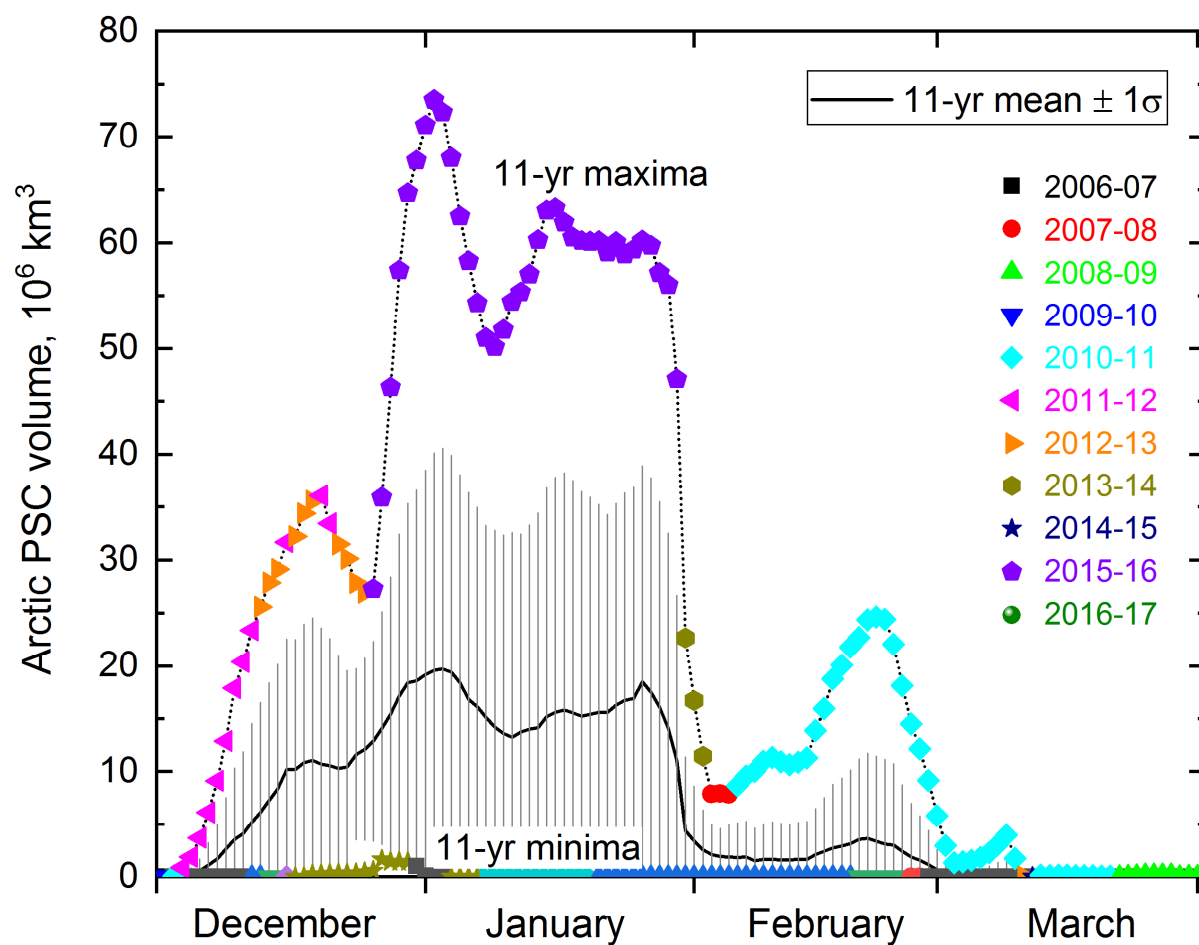


Figure 23: Time series of the 11-year mean, standard deviation, and range of daily values of Arctic PSC spatial volume (daily areal coverage integrated over altitude). The daily maximum and minimum values are color-coded according to the year in which they occurred.

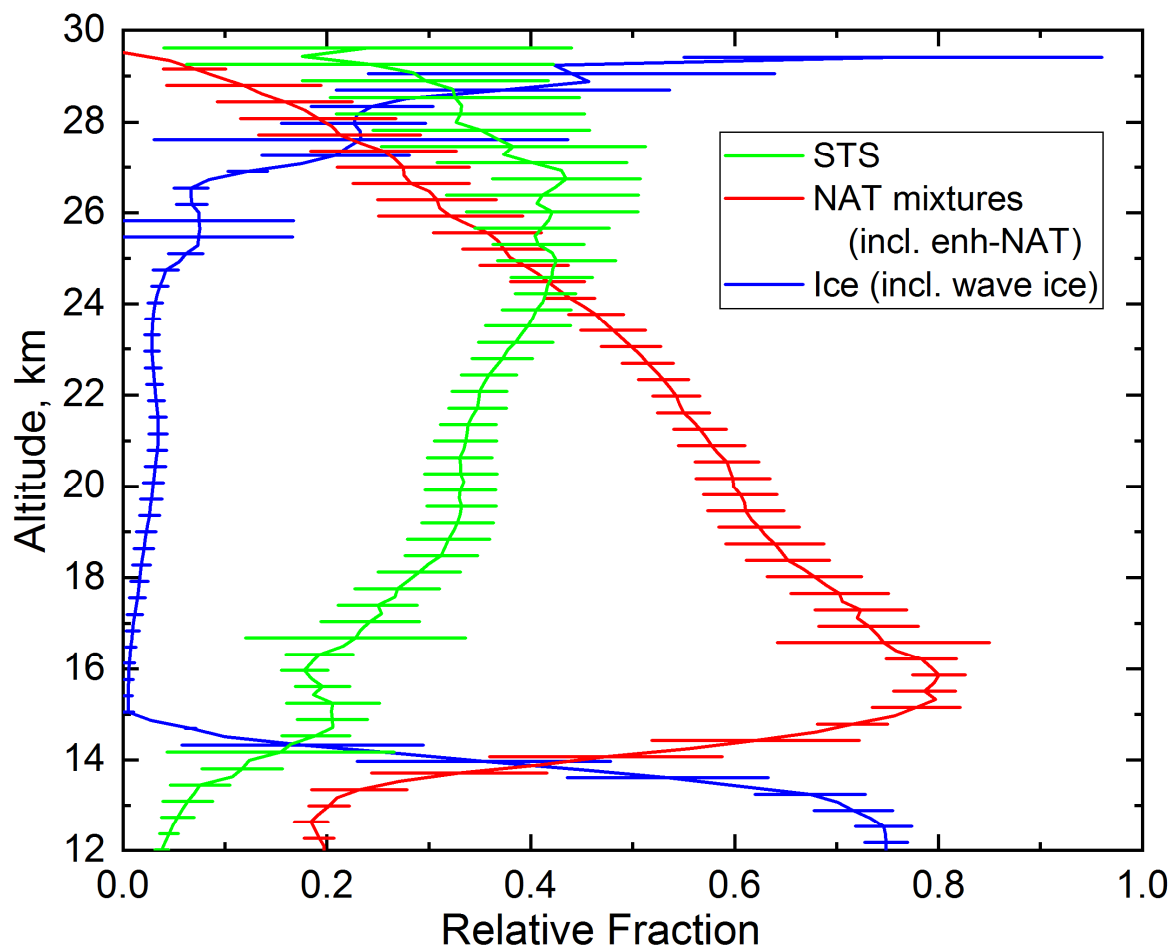


Figure 24: Vertical profile of 11-year mean season-long relative spatial coverage (composition-specific area normalized by total PSC area) of Arctic PSCs by composition. Horizontal bars show the standard error in the mean values and are offset by 0.1 km to avoid overlap.

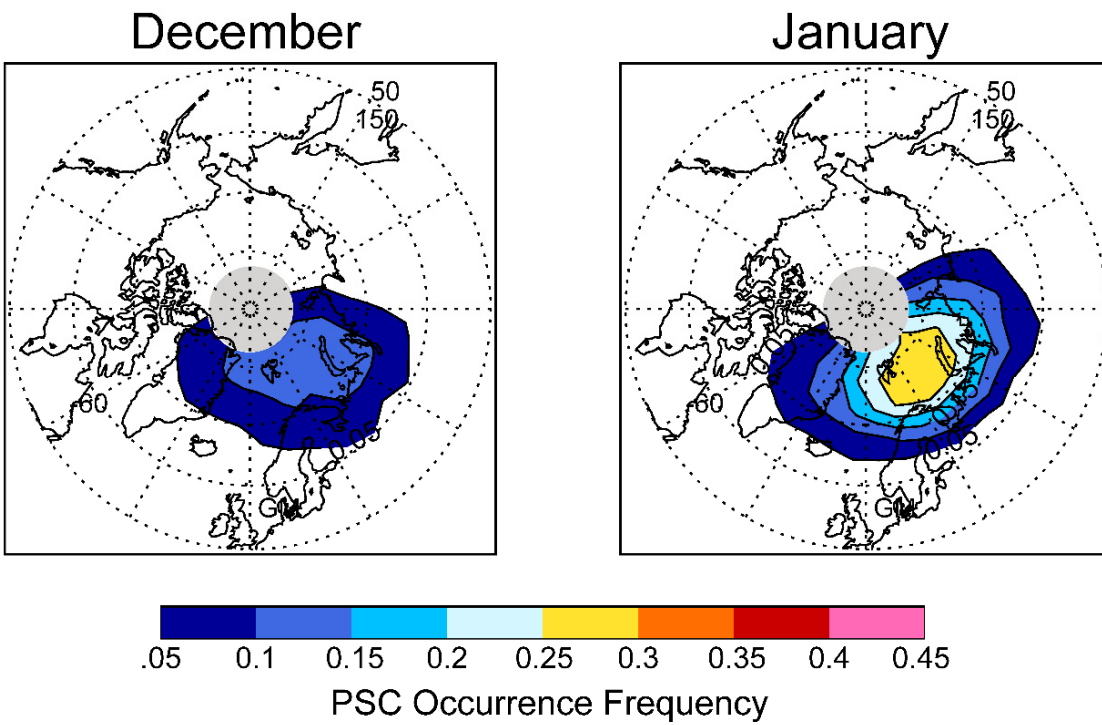
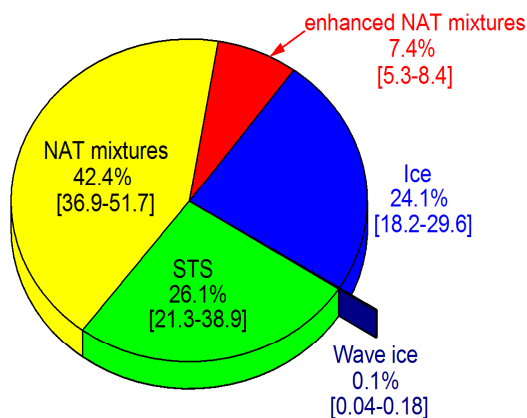


Figure 25: Eleven-year average, monthly mean polar maps of Arctic PSC occurrence frequency at $\theta=500$ K (~20 km). Light gray regions indicate latitudes not sampled by CALIOP.

CALIOP Antarctic PSCs: 2006-2017
3.40E8 total measurement samples



CALIOP Arctic PSCs: 2006-07 to 2016-17
2.27E7 total measurement samples

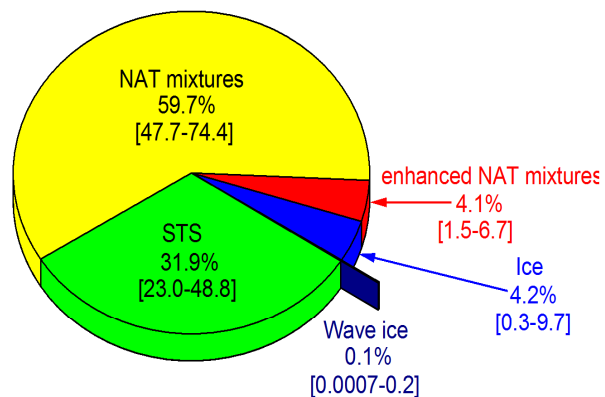


Figure 26: Composition breakdown of CALIOP PSC measurements in the Antarctic and Arctic during 2006–2017. The percentages are averages over the 12 Antarctic and 11 Arctic seasons in the data record, and the minimum and maximum percentages in any one season are indicated by the numbers in brackets. Data are restricted to altitudes 4 km or more above the tropopause to avoid distortion of the statistics by ubiquitous underlying cirrus.

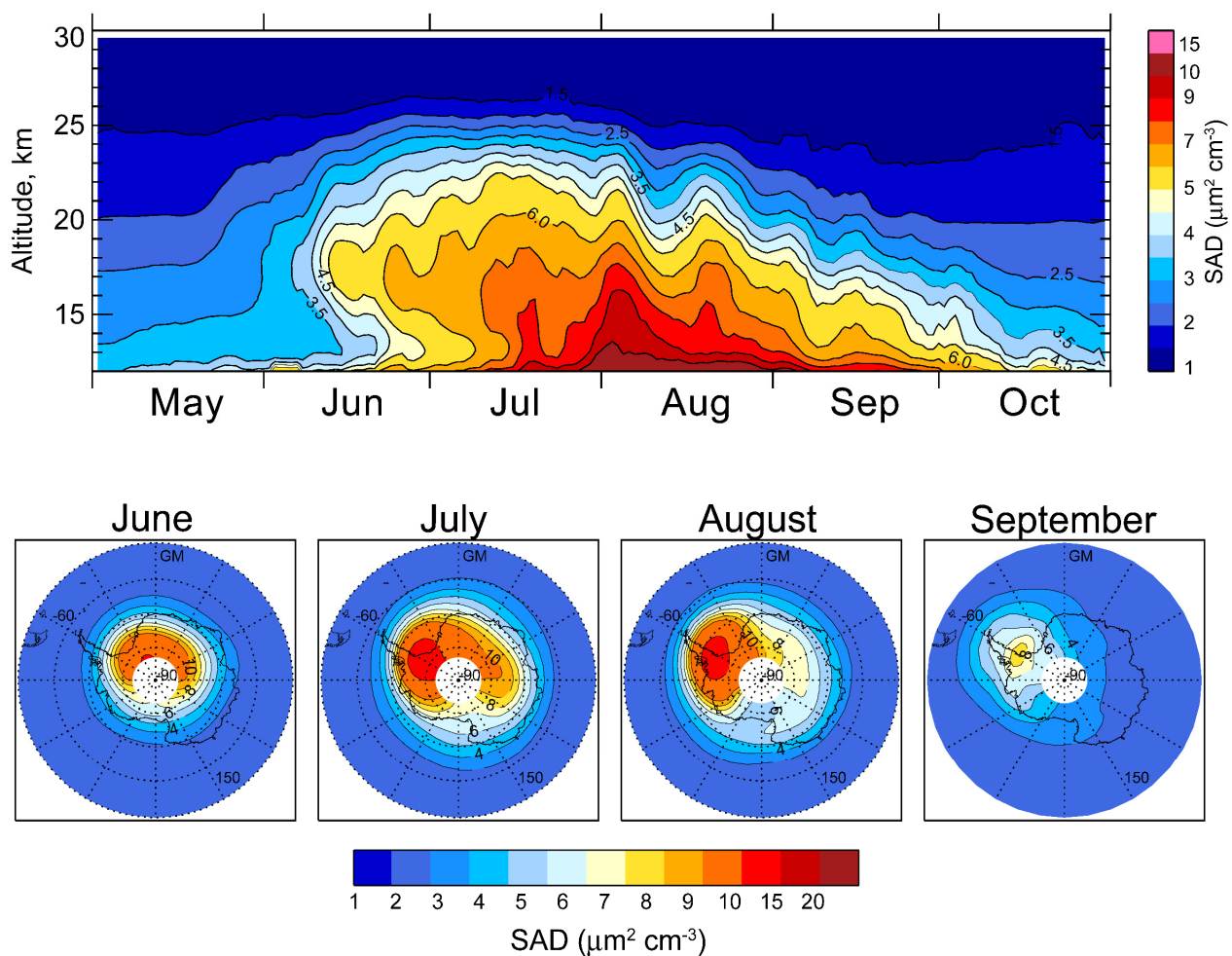


Figure 27: (Top): Twelve-year mean seasonal evolution of Antarctic vortex-averaged SAD. (Bottom): Twelve-year average, monthly mean polar maps of SAD over the Antarctic at 18 km for June-September.

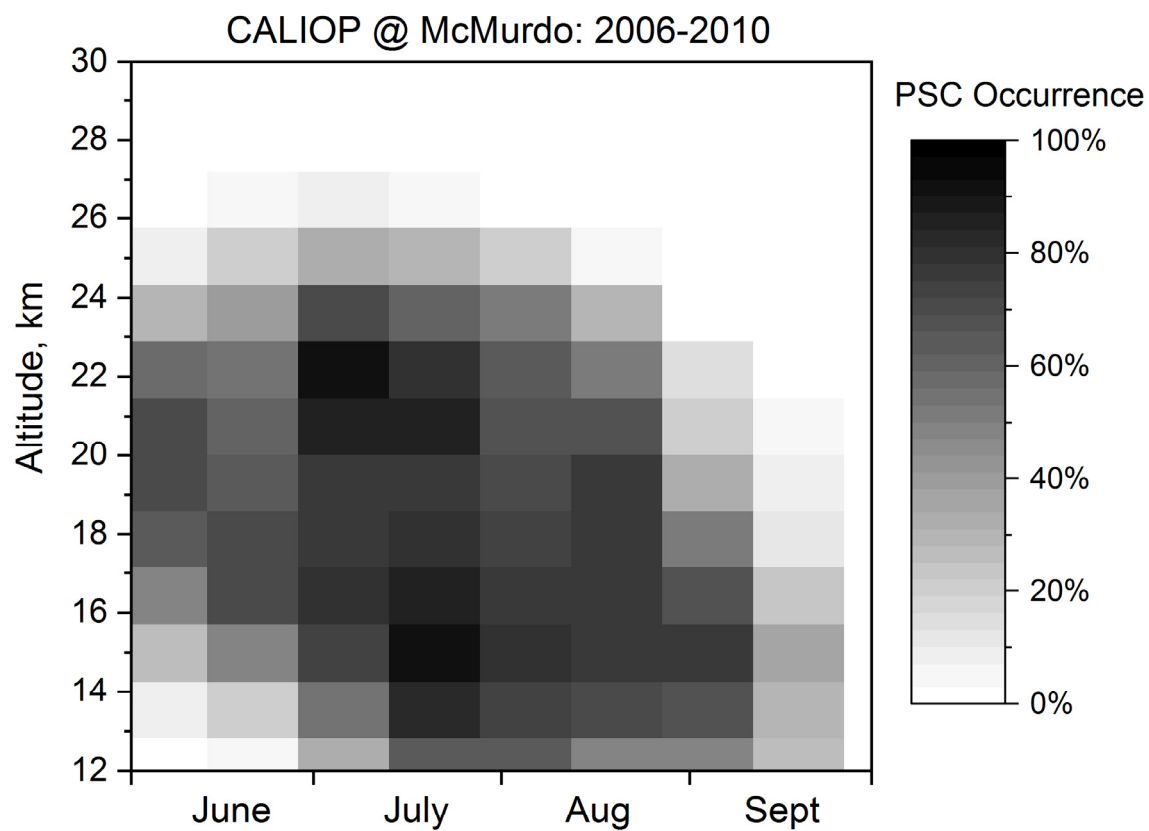


Figure 28: CALIOP v2 PSC occurrence frequencies near McMurdo Station, Antarctica, for June-September, 2006-2010 (in 15-d \times 1.5-km bins) for comparison with ground-based lidar data for the same period shown in Di Liberto et al. (2014).

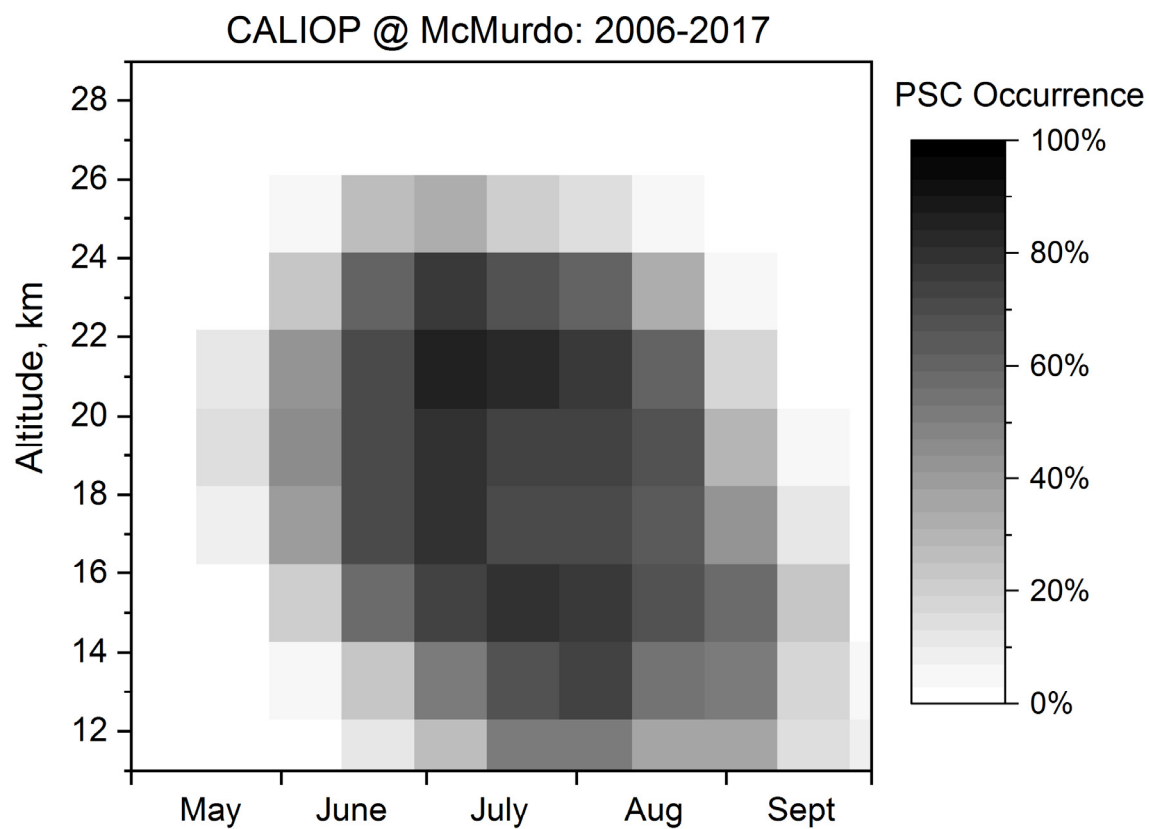


Figure 29: CALIOP v2 PSC occurrence frequencies near McMurdo Station, Antarctica, for May-September, 2006-2017 (in 15-dx2-km bins) for comparison with ground-based lidar data from 1995-2001 shown in Massoli et al. (2006).

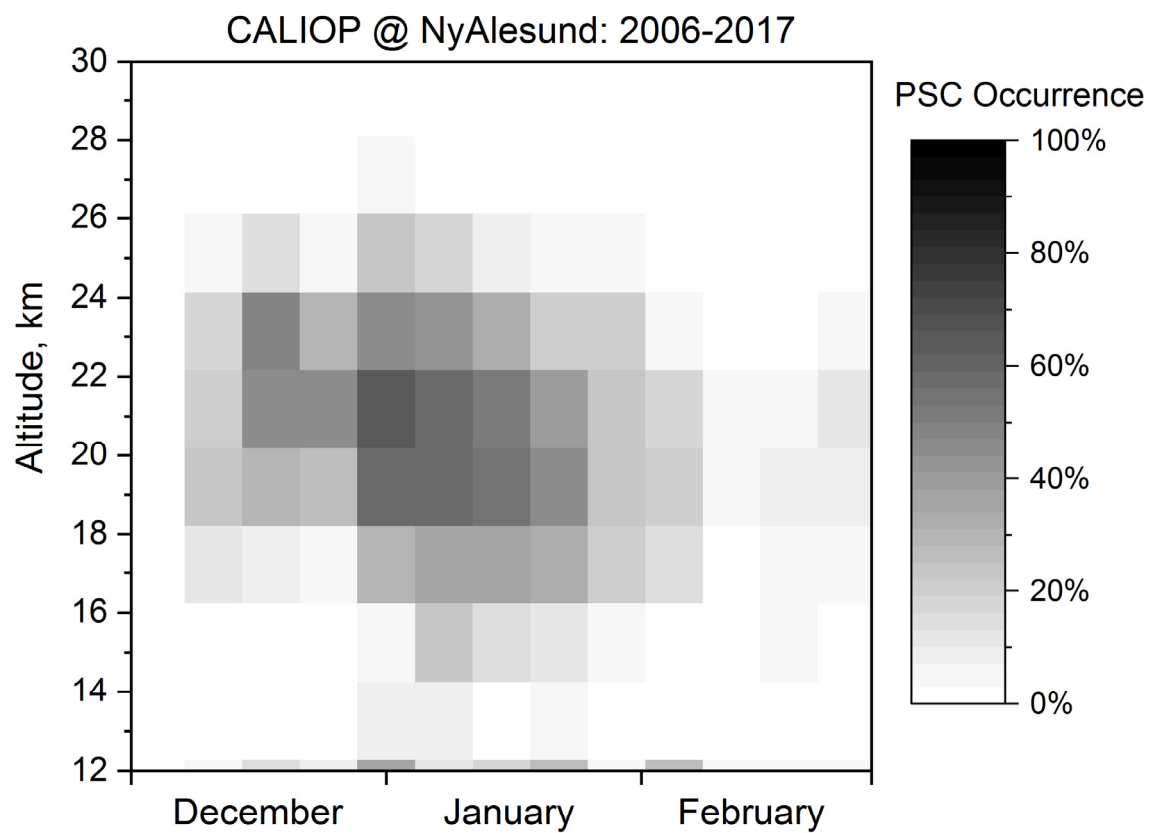


Figure 30: CALIOP v2 PSC occurrence frequencies near Ny-Ålesund, Spitsbergen, for December-February, 2006-2017 (in 7-dx2-km bins) for comparison with ground-based lidar data from 1995-2003 shown in Massoli et al. (2006).

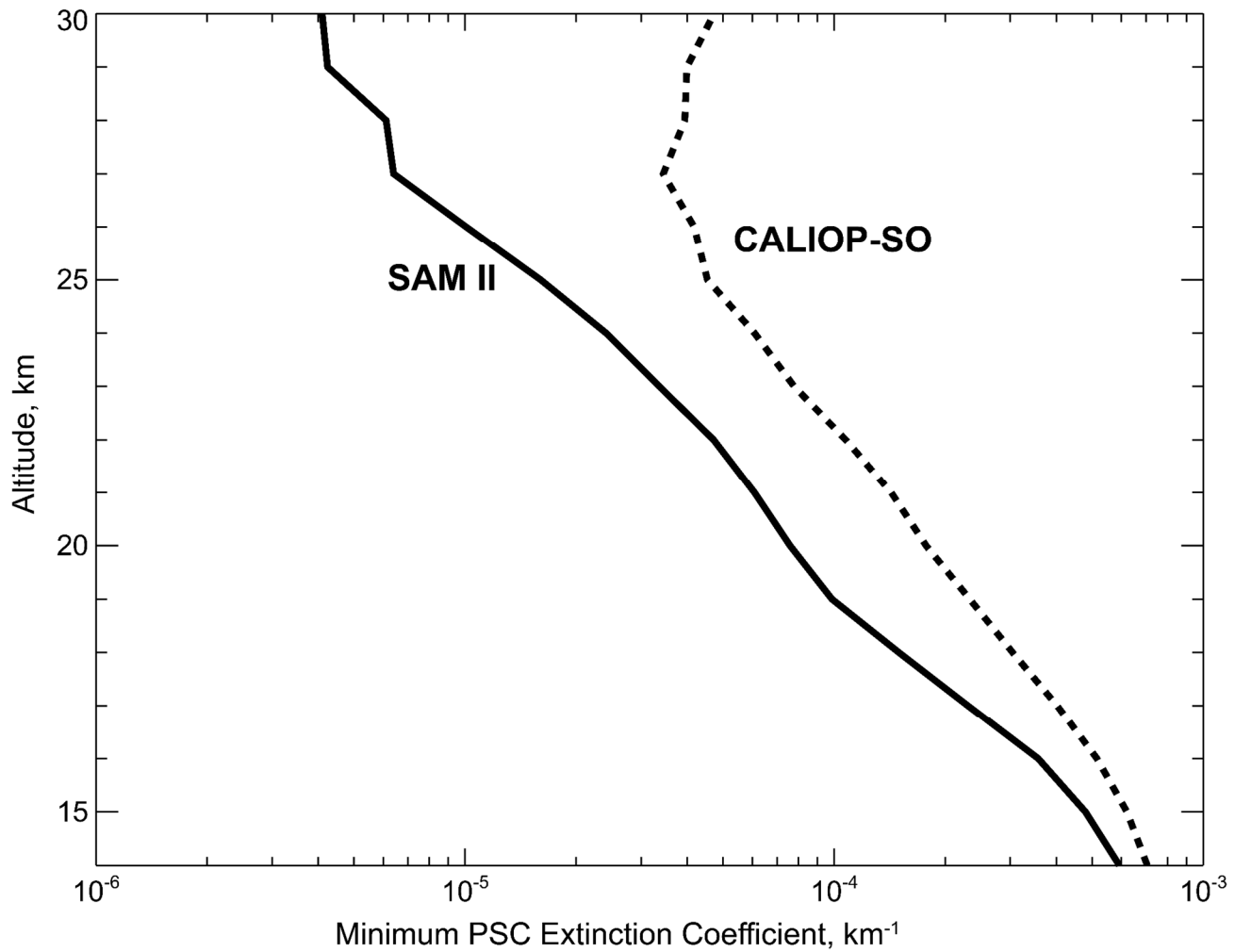


Figure 31: Vertical profile of season-long minimum (1st percentile) values of adjusted ($\times 1.3$) $1\text{-}\mu\text{m}$ $\alpha_{\text{particulate}}$ for SAM II Antarctic PSCs (solid curve) and calculated $1\text{-}\mu\text{m}$ $\alpha_{\text{particulate}}$ for CALIOP-SO Antarctic PSCs (dotted curve).

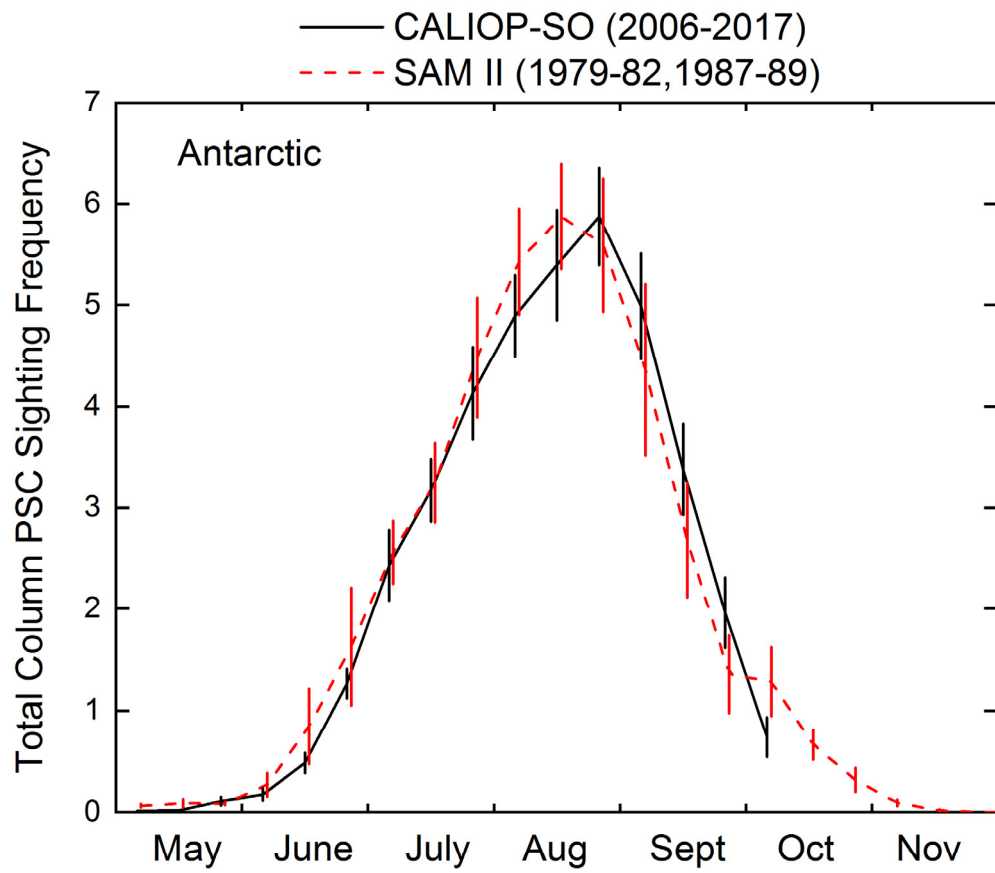


Figure 32: Multi-year mean Antarctic PSC column occurrence frequency from May-November for CALIOP-SO (black solid) and SAM II (red dashed), along with standard errors in the means.

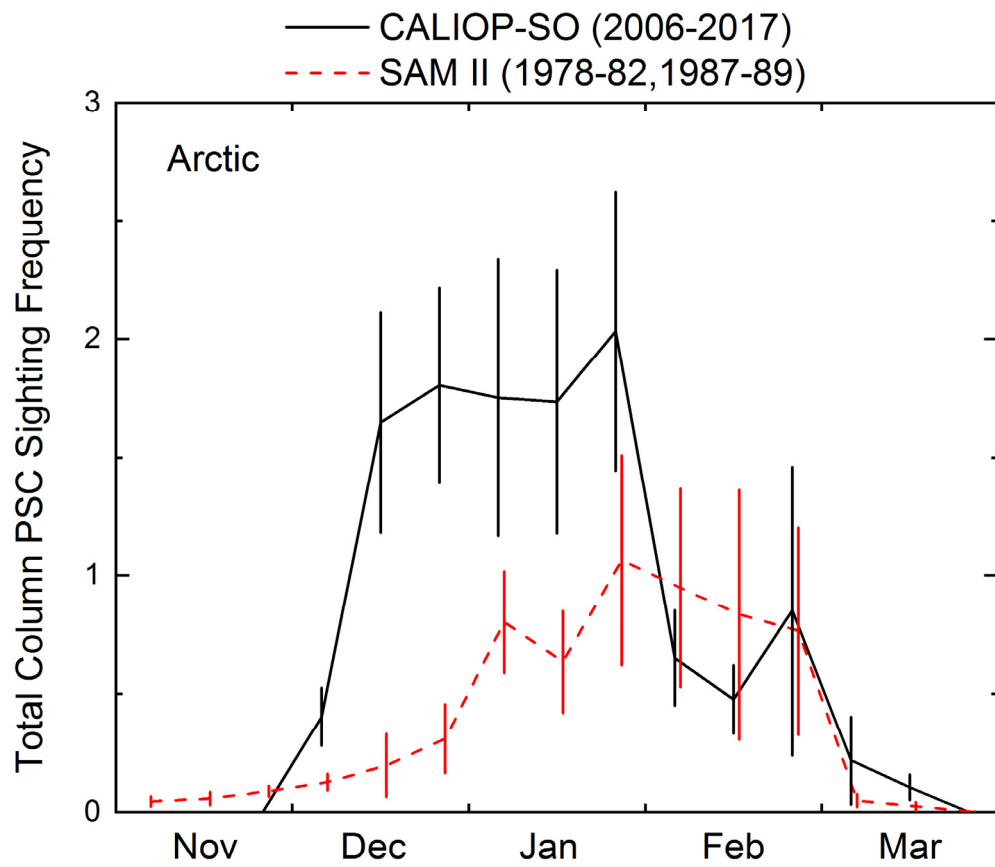


Figure 33: Multi-year mean Arctic PSC column occurrence frequency from November-March for CALIOP-SO (black solid) and SAM II (red dashed), along with standard errors in the means.

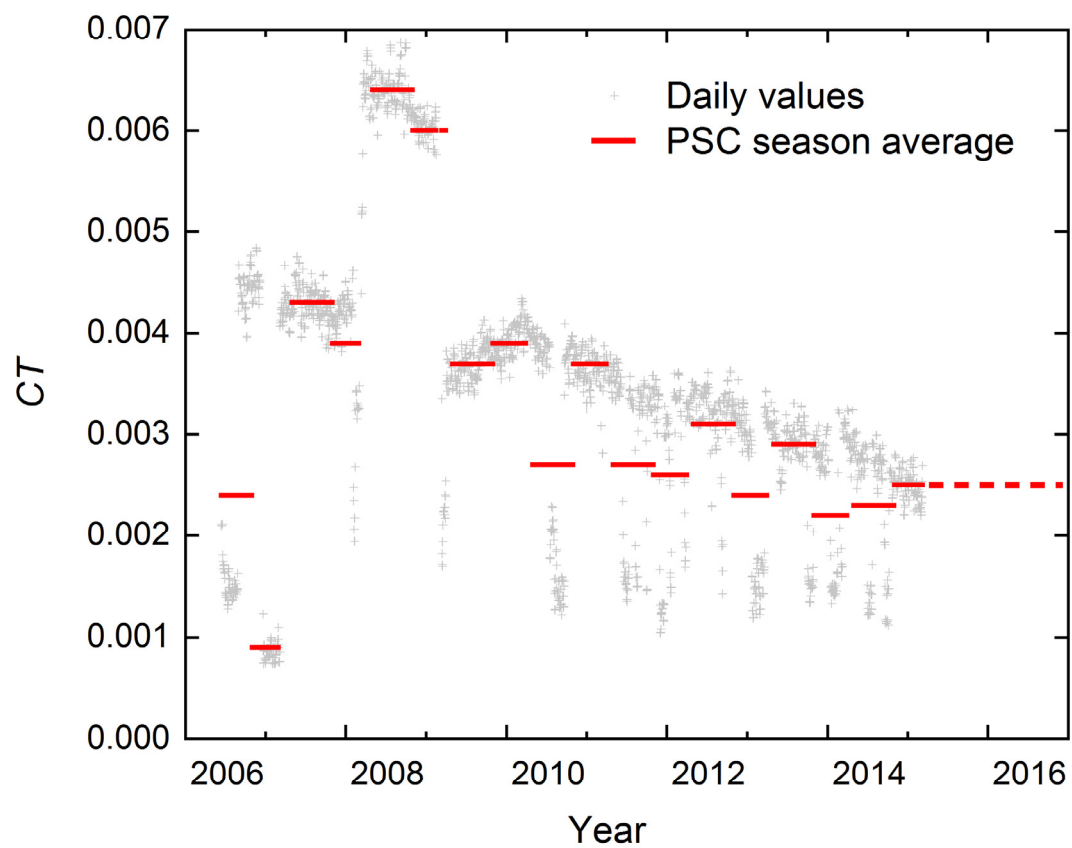


Figure A1: Time series of CT calculated from daily values of $\delta_{\text{mol, meas}}$ over the course of the CALIPSO mission, as well as the averages over PSC seasons.